EXTENDING THE SCIENTIFIC REACH OF ADVANCED LIGO BY COMPENSATING FOR TEMPORAL VARIATIONS IN THE CALIBRATION OF THE DETECTORS

by

DARKHAN TUYENBAYEV, M.S.

DISSERTATION
Presented to the Graduate Faculty of
The University of Texas at San Antonio
In Partial Fulfillment
Of the Requirements
For the Degree of

DOCTOR OF PHILOSOPHY IN PHYSICS

COMMITTEE MEMBERS:
Volker Quetschke, Ph.D., Co-Chair
Richard Savage, Ph.D., Co-Chair
Mario Diaz, Ph.D.
Soma Mukherjee, Ph.D.
Kelly Nash, Ph.D.

THE UNIVERSITY OF TEXAS AT SAN ANTONIO
College of Sciences
Department of Physics and Astronomy
December 2017

DEDICATION

I dedicate this thesis to my parents Ozat Tuyenbayev and Kalima Tuyenbayeva.

ACKNOWLEDGEMENTS

First of all, I would like to thank my supervisors, Prof. R. Savage and Prof. V. Quetschke, for advising me during my studies in the Ph.D. in Physics program. They dedicated an enormous amount of time and effort to ensure that I make the needed progress towards the degree and gave me much valuable professional and life advice. I also thank my first graduate adviser, Prof. M. Rakhmanov, for giving me the opportunity to study physics at the University of Texas at Brownsville and for advising me to take an internship at the LIGO Hanford Observatory. Also, I want to thank my former adviser, Prof. B. Matkarimov, who encouraged me to apply to a graduate program in Physics.

I would like to thank faculty and staff members at the University of Texas at San Antonio and the University of Texas Rio Grande Valley, notably Prof. S. Mukherjee and Prof. K. Nash for serving on my dissertation committee; Professors M. Benacquista, L. Brancaleon, T. Creighton, A. Hanke, X. Lopez-Lózano, K. Martirosyan, S. Mohanty, R. Price and E. Schlegel for teaching courses and giving advice; also C. Balderas, B. Garcia, L. Gomez, C. Robledo, A. Salazar, B. Tucker and A. Wallace.

I am grateful to the director of the Center for Gravitational Wave Astronomy, Prof. M. Diaz, for continued financial support during my Ph.D. study and for serving on my dissertation committee. For their financial support, I would like to thank past and present deans of the College of Sciences at the University of Texas Rio Grande Valley, Prof. M. M. Bouniaev and Prof. P. Grewal. Similarly, for granting me fellowship support, I would like to thank the director of LIGO, Prof. D. Reitze. Their support enabled me to uninterruptedly pursue my Ph.D. degree, conduct research while resident at the LIGO Hanford Observatory, attend meetings in Livingston, LA and Syracuse, NY, and LIGO-Virgo Collaboration meetings in Pasadena, CA and Glasgow, Scotland, from which I gained valuable experiences.

I would like to thank the members of the LIGO Calibration Committee, especially J. Betzwieser, C. Cahillane, E. Goetz, E. Hall, K. Izumi, S. Kandhasami, S. Karki, J. Kissel, G. Mendell, R. Savage, A. Urban, A. Viets, M. Wade and A. Weinstein, with whom I worked long and engaging hours on the calibration of the Advanced LIGO detectors.

I am sincerely indebted to all of the LIGO Hanford Observatory for their camaraderie and support during my three-year residency there.

I would like to thank V. Adiya for her help with editing my dissertation and especially for her encouraging words that helped me to succeed at a critically important time. Also, for their encouragements and valuable advice during the writing of my dissertation, I would like to give my thanks to P. King and M. Landry.

On a personal note, I would like to thank my friends with whom I shared countless enjoyable moments, M. Beroiz, C. Dannangoda, L. R. Diaz, M. Hobosyan, J. Hu, D. Jin, G. Moreno, Z. Ramazanova, A. Timofeeva, G. Valdez, W. Wang and many others in Texas, C. Compton, T. Edo, T. Hardwick, N. Kijbunchoo, E. King, D. McManus, K. Savage, D. Sigg, T. Vo, H. Yu and others whom I met in Washington, M. Cabero, E. Goetz, R. Kennedy, B. Pearlstone and J. Wright who turned my trip to Scotland into an unforgettable experience.

Most importantly, I am grateful to my parents, Ozat and Kalima, and my sister Zhanna for their encouragements and support.

This Masters Thesis/Recital Document or Doctoral Dissertation was produced in accordance with guidelines which permit the inclusion as part of the Masters Thesis/Recital Document or Doctoral Dissertation the text of an original paper, or papers, submitted for publication. The Masters Thesis/Recital Document or Doctoral Dissertation must still conform to all other requirements explained in the Guide for the Preparation of a Masters Thesis/Recital Document or Doctoral Dissertation at The University of Texas at San Antonio. It must include a comprehensive abstract, a full introduction and literature review, and a final overall conclusion. Additional material (procedural and design data as well as descriptions of equipment) must be provided in sufficient detail to allow a clear and precise judgment to be made of the importance and originality of the research reported.

It is acceptable for this Masters Thesis/Recital Document or Doctoral Dissertation to include as chapters authentic copies of papers already published, provided these meet type size, margin, and legibility requirements. In such cases, connecting texts, which provide logical bridges between different manuscripts, are mandatory. Where the student is not the sole author of a manuscript, the student is required to make an explicit statement in the introductory material to that manuscript describing the students contribution to the work and acknowledging the contribution of the other author(s). The signatures of the Supervising Committee which precede all other material in the Masters Thesis/Recital Document or Doctoral Dissertation attest to the accuracy of this statement.

December 2017

EXTENDING THE SCIENTIFIC REACH OF ADVANCED LIGO BY COMPENSATING FOR TEMPORAL VARIATIONS IN THE CALIBRATION OF THE DETECTORS

Darkhan Tuyenbayev, Ph.D.
The University of Texas at San Antonio, 2017

Supervising Professors: Volker Quetschke, Ph.D. and Richard Savage, Ph.D.

Temporal variations in the responses of gravitational wave detectors affect the calibration accuracy of the instruments and therefore can limit the ability to extract parameters of astrophysical sources. We developed and implemented a method for monitoring and correcting for changes in the response functions of Advanced LIGO detectors that significantly reduces calibration uncertainties. The method relies on fiducial periodic test mass displacements induced by radiation pressure actuators at frequencies that enable independent identification of changes in both the sensing and actuation functions. Continuous monitoring of the injected displacements together with a reference-time parametrized model of the detector response function are used to compute improved estimates of the time series that represent differential arm length changes induced by external sources, the gravitational wave data channel. Implementation of this method during Advanced LIGO's first observing period reduced systematic calibration errors by as much as a factor of six, consequently extending LIGO's scientific reach.

TABLE OF CONTENTS

LIST OF TABLES

LIST OF FIGURES

ACRONYMS

AEI	Albert Einstein Institute
aLIGO	Advanced LIGO
AOM	Acousto-Optic Modulator
BH	Black Hole
Caltech	California Institute of Technology
CC	Coupled Cavity
CDS	Control and Data System
DARM	Differential Arm
eLISA	Evolved LISA
EPICS	Experimental Physics and Industrial Control System
ER7	Seventh Engineering Run
ESD	Electrostatic Driver
ET	Einstein Telescope
ETM	End Test Mass
GR	General Relativity
GS	Gold Standard
GW	Gravitational Wave
ITM	Input Test Mass
KAGRA	Kamioka Gravitational Wave Detector
LHO	LIGO Hanford Observatory
LIGO	Laser Interferometer Gravitational Wave Observatory
LISA	Laser Interferometer Space Antenna
LLO	LIGO Livingston Observatory
MCMC	Markov Chain Monte Carlo
MIT	Massachusetts Institute of Technology
NIST	National Institute for Standards and Technology

NS	Neutron Star
O1	First Observing Run
O2	Second Observing Run
Pcal	Photon Calibrator
Rx	Receiver Module
RxPD	Receiver Module Photodetector
SMBH	Supermassive Black Hole
SNR	Signal-to-Noise Ratio
TF	Transfer Function
Tx	Transmitter Module
TxPD	Transmitter Module Photodetector
WS	Working Standard

Chapter 1: OVERVIEW OF GRAVITATIONAL WAVES

Over the course of the last 300 years scientists and philosophers interpreted gravitation in various ways. Prior to publication of the general theory of relativity, Newton's theory of gravity [1] was the mainstream theory, and it is still very useful for describing interactions of masses in the sub-relativistic regime. In his theory of general relativity (GR) published in 1915, Albert Einstein posited that gravitation can be explained with a curvature of spacetime. This interpretation gave a more accurate description of the motions of celestial bodies compared with previous models. One of the implications of the theory is the existence of *gravitational waves* (GWs).

This chapter provides a brief overview of gravitational waves and the GW detectors that are currently in operation, as well as the ones scheduled to come online in the near future. It also gives a summary of the recent first direct detection of gravitational waves by the Advanced LIGO detectors, the GW150914 event.

Discussions in the chapter are intended to give background information that is sufficient for the main subject of the dissertation. A reader interested in more detailed interpretations of these topics can refer to [2–6].

1.1 Gravitational waves

In the theory of general relativity gravity is described as curvature in the geometry of spacetime. According to the theory, changes in the gravitational field caused by masses in accelerated motion produce perturbations of the spacetime metric that propagate through space with a finite speed [7, 8]. Such perturbations are called *gravitational waves*.

In GR, the geometry of spacetime is expressed with a metric tensor, $g_{\alpha\beta}$, where indices α and β correspond to spacetime coordinates, t, x, y and z. Far from sources, GWs can be interpreted as plane waves. Furthermore, a coordinate system can be chosen in which GWs are expressed as

small perturbations of a flat metric,

$$g_{\alpha\beta} = \eta_{\alpha\beta} + h_{\alpha\beta}, \quad \text{for} \quad |h_{\alpha\beta}| \ll 1, \tag{1.1}$$

where $\eta_{\alpha\beta}$ are components of the flat spacetime metric and $h_{\alpha\beta}$ are small perturbations.

For a GW traveling parallel to the z axis, plane-wave solutions of the field equations have the following form

$$h_{\mu\nu}^{\mathrm{TT}} = \begin{pmatrix} 0 & 0 & 0 & 0 \\ 0 & h_+ & h_\times & 0 \\ 0 & h_\times & -h_+ & 0 \\ 0 & 0 & 0 & 0 \end{pmatrix} \cos\left[\omega(t-z)\right], \tag{1.2}$$

In GR the proper distance between two particles is given by

$$L' \equiv \int |ds^2|^{1/2} \tag{1.3}$$

where ds^2 is the line element, $ds^2 = g_{\alpha\beta}dx^\alpha dx^\beta$. Consider the effect of a gravitational wave on two free particles in a vacuum with initial separation L located at $(0,0,0)$ and $(L,0,0)$. To first order the proper distance between these two particles is

$$L' = \int_0^L dx \sqrt{1 + h_+ \cos(\omega t)} \approx L\left(1 + \frac{1}{2} h_+ \cos(\omega t)\right). \tag{1.4}$$

More generally, in the xy-plane the ΔL^x and ΔL^y displacements of a particle with initial (unperturbed) coordinates (L^x, L^y, z) are given by

$$\begin{pmatrix} \Delta L^x \\ \Delta L^y \end{pmatrix} = \frac{1}{2} \begin{pmatrix} h_+ & h_\times \\ h_\times & -h_+ \end{pmatrix} \begin{pmatrix} L^x \\ L^y \end{pmatrix} \cos\left[\omega(t-z)\right]. \tag{1.5}$$

The displacements of a set of particles arranged in a circular pattern, caused by plus- and cross-polarized GWs are shown in Figure 1.1. The figure illustrates the quadrupolar nature of GWs, a

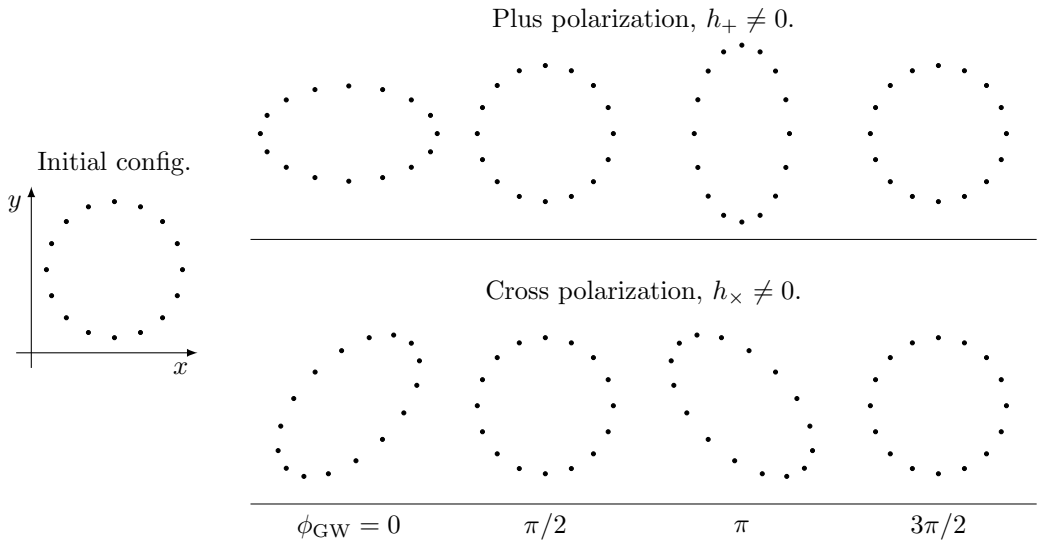

Figure 1.1: Gravitational-wave (GW) polarizations. The left panel shows the spatial arrangement of a set of free particles in the absence of GWs, i.e. their initial configuration. The upper-right and lower-right panels show distortions of these particles from a plus- and cross-polarized GW propagating along the z-axis, $\phi_{\rm GW} = \omega(t - z)$ is the phase of the GW.

45° rotation of the coordinates around the z-axis transforms the h_+ and $h_\times$ polarizations into each other.

1.2 Gravitational wave sources

According to GR gravitational waves are generated by any asymmetrically accelerating masses. However, for the effect to be strong enough for existing scientific instruments to detect, GWs must be generated by cataclysmic astrophysical events such as the inspiral and coalescence of compact binary systems or supernovae explosions. While this section outlines some of the possible GW sources, including compact binary systems that are of highest interest for ground-based GW detectors, an in-depth discussion of astrophysical events that could produce GWs can be found in [5].

1.2.1 Supernova explosions

At the end of their lives heavy stars go through a supernova explosion. When the core of a heavy star gravitationally collapses inward forming a neutron star (NS) or a black hole (BH), a massive explosion ejects part of the star's matter into space. Matter in a supernova process reaches velocities close to $1/10$ of the speed of light. Various observations indicate that supernovae (and hypernovae) explosions are not symmetric. Thus it is expected that they can generate detectable gravitation wave burst signals.

Limited understanding of the details of gravitational collapse in heavy stars and limitations of numerical modeling make it challenging to confidently predict GW waveforms from supernovae. Some numerical simulations suggest that GWs generated by a typical supernovae explosion would produce signals in the frequency range between approximately 200 and 1000 Hz.

1.2.2 Inspiral and coalescence of compact binary systems

Another type of GW sources is compact binary systems composed of black holes, white dwarfs or neutron stars. The radius of the orbit of any binary star system shrinks due to the emission of gravitational radiation. This leads to a decrease in the orbital period followed by the merger of the two stars.

During the inspiral stage the frequency of the GWs generated by the system increases over time. A GW signal with this characteristic form is called a *chirp* signal. The fundamental parameter of the system, consisting of two stars with masses m_1 and m_2, which determines the frequency evolution of the signal, the so-called *chirp mass*, is defined as

$$\mathcal{M} \equiv \frac{(m_1 m_2)^{3/5}}{(m_1 + m_2)^{1/5}}. \tag{1.6}$$

The relation between the frequency of the GW and the chirp mass is

$$\mathcal{M} \simeq \frac{c^3}{G}\left[\frac{5}{96}\pi^{-8/3} f^{-11/3}\dot{f}\right]^{3/5}, \tag{1.7}$$

where f is the signal frequency and $\dot{f}$ is its time derivative [9]. The frequency increase continues throughout the inspiral stage which, as a result of decay in the binary's orbit, is followed by the merger. The observed frequency of the signal is also scaled by a factor of $(1 + z)$, where z is the cosmological redshift. The observed masses are therefore redshifted by this factor.

Based on several detections between September 2015 and January 2017 (GW150914, GW151226 and GW170104), rate estimates for events in this category, binary black hole systems with total mass $\leq 100\ M_{\odot}$, have improved significantly. The most recent merger rate estimate based on two astrophysical population models (described in [10–12]) is $12 - 213\ \mathrm{Gpc}^{-3}\mathrm{yr}^{-1}$ [13]. The given rate is likely biased toward higher numbers due to it being calculated shortly after the most recent event and the estimate being based on a small sample size. Detection of more compact binary coalescence events will likely reduce the bias and distribution uncertainty.

GW signals from binary black hole mergers found in the first and second observational periods of Advanced LIGO are discussed in more detail in Section 1.4.

1.2.3 Supermassive BH binaries and extreme mass-ratio inspirals

Observations indicate that near the center of every galaxy there exists a $10^6 - 10^9\ M_{\odot}$ black hole. BHs in this mass range are called supermassive black holes (SMBH). It is hypothesized that during irregular galactic collisions SMBHs in their cores can inspiral into each other and merge into a single BH.

Gravitational waves generated by the inspiral of SMBH binaries are expected to be in the frequency range from several millihertz to several tens of millihertz [5]. In this frequency band, terrestrial GW detector sensitivities are limited by ground vibrations and gravity gradient noise. The design sensitivity of the future space-based detector eLISA should allow it to detect these events anywhere in the observable universe [14].

Another kind of GW event that involves SMBHs is intermediate and extreme mass-ratio inspirals. These events are produced when a supermassive BH ($M > 10^6 M_{\odot}$) captures a compact object whose mass is in range $1 - 100 M_{\odot}$. The anticipation of these sources is based on evidence

for a large number of compact objects in the vicinities of SMBHs. These are white dwarfs, neutron stars and stellar-mass black holes. GWs produced by inspiral and collision of these objects into SMBHs are among the events that eLISA project is expected to detect [14].

1.3 Global GW detector network

This section gives a brief history of past experiments designed to detect gravitational waves from astrophysical sources, currently operating detectors, and the state of the next generation instrumentation.

Early experiments for detection of GWs were carried out by J. Weber *et.al.* in the 1960's [15]. These first experiments relied on aluminum resonant bar detectors. Later studies showed that the fundamental sensitivity limits of the resonant bar detectors were insufficient for detection of GWs from common astrophysical sources [2, 16].

A possibility of using interferometers for measuring gravitational waves was also discussed in the scientific community in the 1960's. The measurement principle of such instrument is based on observation of variations in the light travel times in the two arms of a Michelson interferometer caused by a passing GW. Initially, a concept of a Michelson interferometer-based GW detector was proposed by M.E. Gertsenshtein and V.I. Pustovoit [17]. R.L. Forward *et. al.* built and conducted research on the first prototype of an interferometric detector at Hughes Aircraft Research Laboratories [18, 19]. In 1970's and 1980's, experimental studies on prototype interferometers were carried out at MIT [20], at the University of Glasgow in Scotland, UK [21], and at the Max Planck Institute for Astrophysics in Garching, Germany [22, 23].

Prototype interferometric detectors revealed a set of technological challenges that needed to be addressed to improve their sensitivities. These experimental results were used as a basis for designing and constructing first-generation long-baseline interferometers: the Laser Interferometer Gravitational-Wave Observatory (LIGO) [24], Virgo [25], GEO 600 [26] and TAMA 300 [27].

First generation gravitational wave detectors held observational periods from 2002 through 2011. These observations helped in setting goals for the second generation detectors (also called

the *advanced* detectors). A future global network of advanced detectors will be comprised of Advanced Virgo in Italy, KAGRA in Japan, GEO-HF in Germany, two Advanced LIGO detectors in the United States and a third Advanced LIGO detector being constructed in India.

1.3.1 Ground-based interferometric gravitational wave detectors

As of 2017, the two LIGO detectors, the LIGO Hanford in Washington and LIGO Livingston in Louisiana, are the most sensitive GW detectors in operation. These were first generation GW detectors with a unified design built under the Initial LIGO (iLIGO) project. An iLIGO detector was a power-recycled Fabry-Perot Michelson interferometer with either $2\,\mathrm{km}$-long or $4\,\mathrm{km}$-long arms [24]. These detectors started operations in 2002 and until 2010 had six observational data collection periods, i.e. "science runs," identified as S1 – S6 runs[1] [29,30]. From 2010 through 2015 the detectors have been upgraded to Advanced LIGO (aLIGO) detectors with design sensitivity ten times better compared to the initial LIGO detectors. Most significant results, i.e. direct detections of GWs, from observational periods of Advanced LIGO between September 2015 and January 2017 are discussed in Section 1.4.

The Virgo detector in Cascina, Italy is a product of the collaborative work of research institutions in Italy and France. This power recycled Fabry-Perot Michelson interferometer with $3\,\mathrm{km}$-long arms was initially commissioned in 2007 and held coincident observations with LIGO during the S5 run. Recently it was upgraded under the Advanced Virgo project [31] and together with Advanced LIGO held joint observations between August 1 and 25, 2017 [32].

The KAGRA detector located in Kamioka, Japan, is an advanced detector with $3\,\mathrm{km}$-long arms [33].[2] A significant difference between KAGRA and other second-generation detectors is that it employs cryogenically cooled sapphire test masses. Commissioning efforts at KAGRA are mostly complete, and it is expected to start observations in as early as 2019 [34].

Another advanced GW detector mentioned above is the GEO HF detector located in Hannover,

[1] Between S5 and S6 the detectors underwent upgrades under the Enhanced LIGO (eLIGO) project [28], so technically while S1 – S5 are iLIGO science runs, the S6 is an eLIGO run.

[2] Initially, this detector was called the Large-scale Cryogenic Gravitational-Wave Telescope (LCGT).

Germany. While LIGO, Virgo and KAGRA instruments target increased sensitivities in the frequency band from $20\,\mathrm{Hz}$ to about $2\,\mathrm{kHz}$, the primary goal of GEO-HF upgrades of this $600\,\mathrm{m}$ interferometer is to improve its sensitivity at higher frequencies [35]. As of 2014, these upgrades have been implemented and further improvements of the detector are being discussed [36].

1.3.2 Future instruments for detecting gravitational waves

Sensitivities of ground-based GW detectors at frequencies below $1\,\mathrm{Hz}$ are compromised by seismic and gravity gradient noises. A detector placed in space would not be susceptible to these noises. A project of such a detector that is currently being developed is the Laser Interferometer Space Antenna (LISA). The current design is called the evolved LISA (eLISA) [14] and it is expected to launch in the 2030s [37]. The most recent milestone achieved by the LISA project is the successful completion of the LISA Pathfinder mission in 2016, whose purpose was the assessment of acceleration noises of LISA test masses with respect to their local inertial frame [38].

The eLISA is envisioned to consist of three spacecraft that form a triangular constellation placed in a heliocentric orbit. They will form a Michelson interferometer with arm lengths, i.e. separation between the satellites, of $2.5 \times 10^6\,\mathrm{km}$. The sensitivity of the LISA detector is expected to be sufficient to detect mergers of binary SMBHs at redshifts as large as $z \approx 11$ [14].

Einstein Telescope (ET) is a conceptual project of a third generation GW detector that is currently being discussed by the European Commission [39]. This underground observatory will have three $10\,\mathrm{km}$-long arms arranged in a triangular shape, and be capable of measuring GWs at frequencies below $10\,\mathrm{Hz}$ [40–42].

1.4 Experimental confirmations of GWs

Since the publication of GR almost a century ago, many predictions of the theory have been experimentally verified. This includes indirect confirmation of GWs by Hulse and Taylor and the more recent first direct observations of GWs from binary black hole mergers with LIGO detectors.

Indirect evidence supporting the prediction of gravitational waves was based on long-term

observations of the binary pulsar system PSR B1913+16 discovered by Hulse and Taylor in 1975 [43]. Consequent observations revealed that the decay in the orbital period of the system agrees with predicted energy losses due to the emission of gravitational waves [44].

The first observational period of Advanced LIGO, the O1 run, that was carried out from September 2015 until January 2016 lead to the historical first direct detection of gravitational waves, the GW150914 event [45], as well as detection of two other transient GW events LVT151012 and GW151226 [11, 46].

Furthermore, aLIGO's second observational period (the O2 run) rendered a detection of a GW event from a coalescence of two black holes at even greater luminosity distance compared to the events from the O1 run. This signal was recorded on January 4, 2017

1.4.1 First direct observation of gravitational waves

The GW150914 signal was recorded by LIGO Hanford and LIGO Livingston detectors on September 14, 2015 at 09:50:45 UTC [45]. Data from the two detectors are replicated to computer clusters at Caltech, MIT and AEI where they are analyzed by software pipelines running search algorithms. The coincident signal was initially found by low-latency searches [47, 48].

An interferometric GW detector has a broad antenna pattern. A transient signal recorded by a single GW detector is insufficient to determine the sky location of the source. This information can be inferred from differences in the signal arrival times at several instruments comprising a GW detector network. Amplitude and phase differences resulting from the respective orientation of detectors allows further restrict possible source locations. During the event, three large-scale GW detectors were in operation: the GEO HF and the two LIGO detectors. Since the sensitivity limitations of the former did not allow it to measure the signal, the sky location of the GW150914 was estimated based on measurements by the two LIGO detectors. The source location was determined to lie in a region with an area $150\ \mathrm{deg}^2$ with $50\ \%$ probability and $600\ \mathrm{deg}^2$ with $90\ \%$ probability.

In the post-Newtonian theory, the phase evolution of a GW signal such as GW150914 at low frequencies is governed by the so-called *chirp mass* [9]. For the GW150914 event the estimated

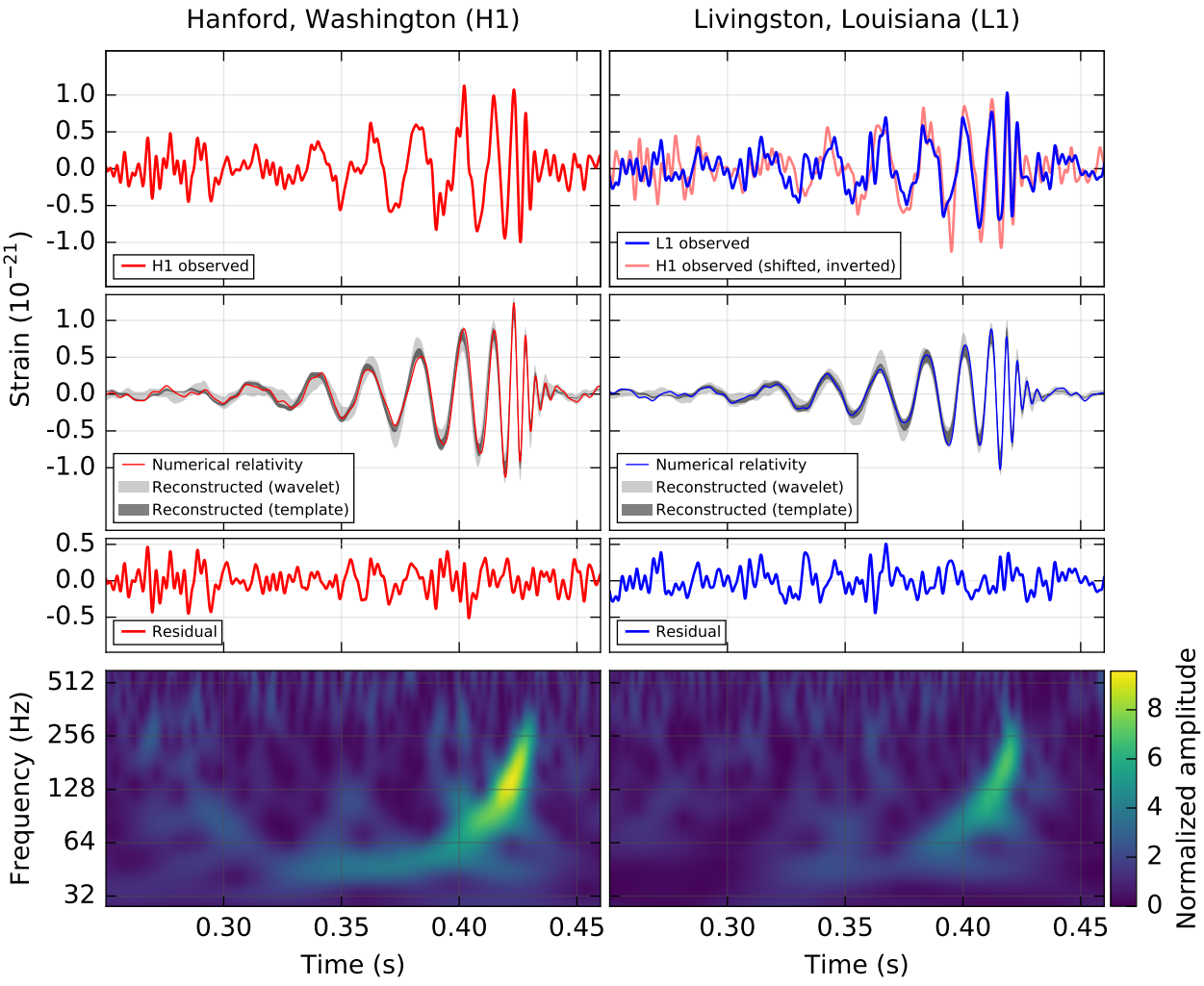

Figure 1.2: The gravitational wave signal from the GW150914 event. All time series shown here are filtered with a $35 - 350\,\mathrm{Hz}$ bandpass filter. The *top row* shows the H1 (LIGO Hanford) and L1 (LIGO Livingston) time series, the *top left panel* shows both time series overlapped with the H1 strain shifted by $6.9\,\mu\mathrm{s}$ to compensate for the delayed signal arrival at the H1 detector, and inverted to account for difference in the relative orientation of the detectors. On both of the panels of the *second row* traces show the numerical relativity (NR) waveform computed for the system with the GW150914 source parameters (*solid black lines*), $90\,\%$ credible region for signal reconstruction based on binary black hole template waveforms (*dark gray*) and 90% credible region of a strain signal calculated from combination of sine-Gaussian wavelets (*light gray*). The *third row* shows the background noise after the NR waveforms are subtracted from the time series. The time-frequency plots in the *bottom row* show how the frequency of the signal evolved during the inspiral. From [45].

chirp mass is $\mathcal{M} \approx 30 M_\odot$ and the total mass of the system in the detector frame is $M \approx 70 M_\odot$ [49]. The evolution of the signal from this intermediate stellar mass binary, reaching frequencies near 150 Hz, indicated high density of the stars forming the binary. It showed that the binary was formed from two black holes.

The estimated masses of the initial black holes are $36^{+5}_{-4}\ M_\odot$ and $29^{+4}_{-4}\ M_\odot$. The black hole formed as the result of the merger has mass $62^{+4}_{-4}\, M_\odot$ and spin $0.67^{+0.05}_{-0.07}$. During this event the total energy radiated by the system in the form of GWs is $3.0\, M_\odot c^2$. Properties of the GW150914 event are discussed in more detail in [49].

1.4.2 The first astrophysical event observed both in gravitational waves and in light

In August 2017, the Virgo detector in Italy, became the third instrument to complete commissioning tasks and come online to join the network of second generation GW detectors. On August 17, 2017, this network, that now is comprised of three instruments, detected the first GW transient signal from a binary neutron star merger, GW170817 [50]. Unlike the first event observed by the LIGO-Virgo network, a binary black hole merger GW170814 [51], this signal was not only observed in gravitational waves, it was also seen by electromagnetic telescopes. Because, all three GW detectors were in observation mode during this event, the sky location of the source was estimated to lie within an area of $\sim\ 30\,\mathrm{deg}^2$, which is about 20 times more precise localization compared to the GW150914 event. This gave better possibilities for traditional telescopes to find the source. Over the course of several days after the arrival of GW signal, seventy terrestrial and space-based observatories followed up on this event. As a result, the electromagnetic counterpart of the signal was captured in a wide band of the electromagnetic spectrum: gamma rays, X-rays, ultraviolet, visible, infrared and radio waves [52]. The data collected from this signal enabled astrophysicists to test several astrophysical and cosmological hypotheses [53, 54].

1.4.3 Other GW events in Advanced LIGO's first and second observational periods

The second signal detected during the O1 run, which had a high statistical significance, is the GW151226 event. This signal was measured on December 26, 2015 at 03:38:53 UTC. A longer duration of this signal allowed to estimate the chrip mass with a narrower confidence interval, $\mathcal{M} \approx 8.9^{+0.3}_{-0.3}\, M_\odot$. This GW transient event was also generated by the merger of two black holes of masses $14.2^{+8.3}_{-3.7}\, M_\odot$ and $7.5^{+2.3}_{-2.3}\, M_\odot$, forming the final black hole of mass $20.8^{+6.1}_{-1.7}\, M_\odot$ [46].

On January 4, 2017 at 10:11:58 UTC, the two Advanced LIGO detectors registered another GW transient signal, the GW170104 event. This GW signal was estimated to have a redshift $0.18^{+0.08}_{-0.07}$, the equivalent luminosity distance $880^{+450}_{-390}\,\mathrm{Mpc}$. The masses of the initial black holes were $31.2^{+8.4}_{-6.0}\, M_\odot$ and $19.4^{+5.3}_{-5.9}\, M_\odot$ [13].

Another coincident GW transient signal that was observed during the O1 run was the LVT151012 trigger. This event had a low statistical significance of $1.7\,\sigma$ with false alarm rate of $0.37\,\mathrm{yr}^{-1}$. The event was reported in [11].

After the two detections made in the O1 run, merger rate was estimated to lie between 9 and $240\ \mathrm{Gpc}^{-1}\mathrm{yr}^{-1}$. The new merger rate estimates calculated after the GW170104 signal was incorporated into the analysis are $12 - 213\ \mathrm{Gpc}^{-2}\mathrm{yr}^{-1}$, which is consistent with the earlier black hole rate estimates. The most recent merger rate estimates were based only on the events with high statistical significance and excluded the LVT151012 trigger from the analysis.

Chapter 2: ADVANCED LIGO DETECTORS AND THEIR CALIBRATION

Gravitational wave source parameters, e.g. the masses of the stars that generated the GWs and their spins, are inferred from the probability density functions of parameters extracted from the strain data. The probability density functions are obtained with the Bayesian approach, by multiplying the likelihood of the data for a simulated set of parameters and prior probabilities. Calibration errors are incorporated into the analysis by simulating random deviations of frequency-domain models from the perfect models that are based on sample source parameters. The range of these random deviations is determined by calibration uncertainties associated with the detector calibration. Thus, reduced calibration errors directly impact the parameter estimation process.

Advanced LIGO interferometers are second generation GW detectors (see Section 1.3). With the capability of measuring changes in the differential displacement of the two arms of the interferometer on the order of $10^{-19}\,\mathrm{m}$, as of writing this dissertation, they are the most sensitive instruments in operation [55, 56]. Even at these sensitivity levels the absolute test mass displacements are calibrated with uncertainties of less than $10\,\%$ in magnitude and 10° degrees in phase.

This chapter gives an overview of the Advanced LIGO detector calibration procedure used during the first and second observational periods. In order to understand how calibration of the Advanced LIGO detectors is made, one has to have some background knowledge of how the detectors operate, which is provided in Section 2.1. Section 2.2 gives an overview of the Advanced LIGO calibration. Section 2.3 describes calibration models of the sensing and actuation functions of the differential arm length feedback control loop. Section 2.4 explains how measurements of the frequency dependent response of the interferometer are made. Section 2.5 describes how model parameters of the response function are determined.

It is important to note that, although the material covered in this chapter includes descriptions of the measurements and techniques for estimating parameters of the response function model, two important topics have not been covered here. One of them is the topic of temporal variations of

the interferometer response. This is the central subject of this dissertation and it is discussed in Chapter 3. The other one, discussed in Chapter 4, is the aLIGO Photon Calibrator tool, the primary calibration tool for inducing fiducial displacements of test masses.

During nominal operation of the detector, desired resonance conditions in its cavities are maintained by control loops. Fluctuations in the differential arm length degree of freedom of the interferometer (DARM) are suppressed by the DARM control loop. Thus, characterization of the DARM response function is crucial for reconstruction of the GW strain signal. Discussions in this chapter cover measurements of the DARM sensing and actuation functions and methods used for obtaining the corresponding models.

2.1 Advanced LIGO detectors

Differential fluctuations in the interferometer arm lengths alter the interference condition at the beamsplitter that results in intensity fluctuations at its output port. A Michelson interferometer thus transduces gravitational waves by measuring differential fluctuations in the light travel times along the two arms of the interferometer. The signal that contains GW signal is generated by electronic outputs of photodetectors at the anti-symmetric port, also called the GW port. Fluctuations in the differential arm length of an aLIGO detector from external disturbances, $\Delta L_{\rm ext}$, are caused by either displacement noise or by a passing gravitational wave. In Advanced LIGO the GW strain signal is defined as fractional variations in the differential arm length of the interferometer, $h \equiv \Delta L_{\rm ext}/L$.

In in the last decades, interferometric gravitational wave detectors became a crucial part of the global gravitational wave detector network. First generation kilometer-scale ground-based gravitational wave detectors were capable of measuring strain with precision $10^{-19}\,/\sqrt{\rm Hz}$. Over the years, continued efforts allowed improving the sensitivities of such detectors by several orders of magnitude.

These instruments, which now belong to the second-generation interferometric gravitational wave detectors, reached GW strain sensitivities of $10^{-23}\,/\sqrt{\rm Hz}$ in the frequency band between 50

and $300\,\mathrm{Hz}$ [56].

2.1.1 Interpretation of length measurements made with a Michelson interferometer

Although sensitivity improvements of aLIGO detectors were achieved via implementing complex techniques, fundamentally the operation principle of these detectors can be explained by the response of a Michelson interferometer.

Propagation of gravitational waves causes the spacetime metric to fluctuate. As was explained in Section 1.1, changes in the metric can be expressed in terms of changes in the distances traversed by light along the interferometer arms. One of the ways for making high-precision measurements of fluctuations in the differential length along two paths is to use an interferometer. The Michelson interferometer, in particular, measures differential length fluctuations along two perpendicular beam paths, which makes it an efficient transducer of GWs.

Propagation of an electromagnetic field from a coherent laser source can be expressed in terms of plane waves. For instance, the electric field of a polarized laser beam with the maximum amplitude of E_0 and wavelength λ propagating along the x-axis can be written in the following form

$$E(t,x) = E_0 e^{i(kx-\omega t+\phi_0)}, \tag{2.1}$$

with the frequency of the beam, ω, and the wave number, k, given by

$$\omega = \frac{2\pi c}{\lambda} \tag{2.2}$$

$$k = \frac{2\pi}{\lambda} = \frac{\omega}{c} \tag{2.3}$$

where ϕ_0 is the phase shift.

Let the laser beam travel between two free-falling test masses placed at points A and B. Electric

fields at these points are given by

$$E_A(t) \equiv E(t, x_A) = E_0 e^{i(-\omega t + \phi_0)} e^{ikx_A} \tag{2.4}$$

$$E_B(t) \equiv E(t, x_B) = E_0 e^{i(-\omega t + \phi_0)} e^{ikx_B} \tag{2.5}$$

The phase of the electric field traveling between the test masses can be calculated by taking the ratio of the complex fields E_A and E_B:

$$\begin{aligned} \Delta\phi_{AB} &= \arg\left(\frac{E_B(t)}{E_A(t)}\right) = \arg\left(\frac{E_0 e^{i(-\omega t+\phi_0)} e^{ikx_B}}{E_0 e^{i(-\omega t+\phi_0)} e^{ikx_A}}\right) = \arg\left(e^{ik(x_B - x_A)}\right) \\ &= k(z_B - z_A) \end{aligned} \tag{2.6}$$

In other words, the phase rotation is linearly proportional to the distance between the two freely falling test masses.

Light traveling through a medium perturbed by a passing gravitational wave experiences these perturbations as variations in the spacetime interval it traverses. As shown in Section 1.1, this effect can be expressed as perturbations of the nominal distance between the test masses by a time-varying strain $h(t)$. Thus, the electric field of the light wave in the presence of GWs can be re-written as

$$E(t, x) = E_0 e^{i(-\omega t + \phi_0)} e^{i\phi(t,x)}, \tag{2.7}$$

where the phase is given by

$$\phi(t, x) = k \int_0^x \left(1 + \frac{1}{2} h(t)\right) dx'. \tag{2.8}$$

In the presence of GWs, for light traveling between two test masses placed at points $A = (x_A, 0, 0)$ and $B = (x_B, 0, 0)$, the total phase rotation of the electric field can be obtained by substituting

Equation (2.8) into Equation (2.6),

$$\Delta\phi_{AB}(t) = k\int_{x_A}^{x_B}\left(1+\frac{1}{2}h(t)\right)dx' = k(x_B - x_A) + \frac{1}{2}k\int_{x_A}^{x_B} h(t)dx'. \tag{2.9}$$

In a Michelson interferometer the laser beam enters the interferometer at the input port. Half of the beam power is transmitted through the beamsplitter and the other half is reflected. Each of the two beams travels along one arm of the interferometer and reflects from the mirror at the end of the arm back toward the beamsplitter. The power of the recombined beam measured at the *anti-symmetric port* depends on the interference condition.

The projection of time-varying changes in the strain produced by the two independent polarization of a gravitational wave, h_+ and $h_\times$ (see Section 1.1), in a Michelson interferometer can be written as

$$h(t) = F_+ h_+(t) + F_\times h_\times(t), \tag{2.10}$$

where $h(t)$ is the time-varying changes in the strain along the interferometer arms, F_+ and $F_\times$ are the antenna beam patterns that are functions of the GW source location in the sky and its polarization [19].

The total phase rotations of the electric fields of laser beams that make round trips along the two arms, commonly referred to as the x- and y-arms of an interferometer, can then be expressed as

$$\Delta\phi_x(t) = 2\left(kL + \frac{1}{2}kLh(t)\right) \tag{2.11}$$

$$\Delta\phi_y(t) = 2\left(kL - \frac{1}{2}kLh(t)\right) \tag{2.12}$$

The interference condition at the beamsplitter that determines the intensity of the beam at the output port is conditioned by the phase difference in the electric fields of the beams that traversed

along the two arms. This phase difference (from Equations (2.11) and (2.12)) is

$$\Delta\phi_{xy}(t) = 2kLh(t) = \frac{2\omega L}{c}h(t), \tag{2.13}$$

where ω is the frequency of the laser beam, c is the speed of light, $h(t)$ is the GW strain from Equation (2.10).

2.1.2 Optical layout of an Advanced LIGO detector

The two Advanced LIGO detectors, LIGO Hanford (LHO) in Washington and LIGO Livingston (LLO) in Louisiana, are Dual-Recycled Fabry-Pérot Michelson interferometers with 4-km-long arms. A schematic diagram of their optical configuration is shown in Figure 2.1. The input beam is generated by a pre-stabilized Nd:YAG laser operating at $1064\,\mathrm{nm}$ and capable of producing output beam power of up to $180\,\mathrm{W}$. The beam is split into two beams of equal power that are sent into the arms of the Michelson interferometer. Each arm of the detector has a partially transparent mirror at the end closest to the beamsplitter and a highly reflective mirror at the other end. The two mirrors, called the input test mass (ITM) and the end test mass (ETM) respectively, form a 4 km-long Fabry-Pérot cavity. A partially transparent mirror installed at the input port of the interferometer, called the power recycling mirror, increases the amount of laser power circulating in the detector, thus reducing a fundamental noise source, shot noise. Another partially transparent mirror placed at the output port, called the signal recycling mirror, forms the coupled cavity with the arm cavities, thus increases the overall sensing gain of the GW detector.

2.1.3 Sensitivity of Advanced LIGO detectors

The sensitivity of an aLIGO detector is limited by numerous noise sources including ground motion, thermal noises, quantum noises and noises arising from changes in the local Newtonian gravitational field. Each of these noise sources limits the sensitivity of the detectors in specific frequency bands (see Figure 2.2). At lower frequencies the sensitivity is limited by ground motion and thermal noises. The sensitivity at higher frequencies is limited by quantum shot noise.

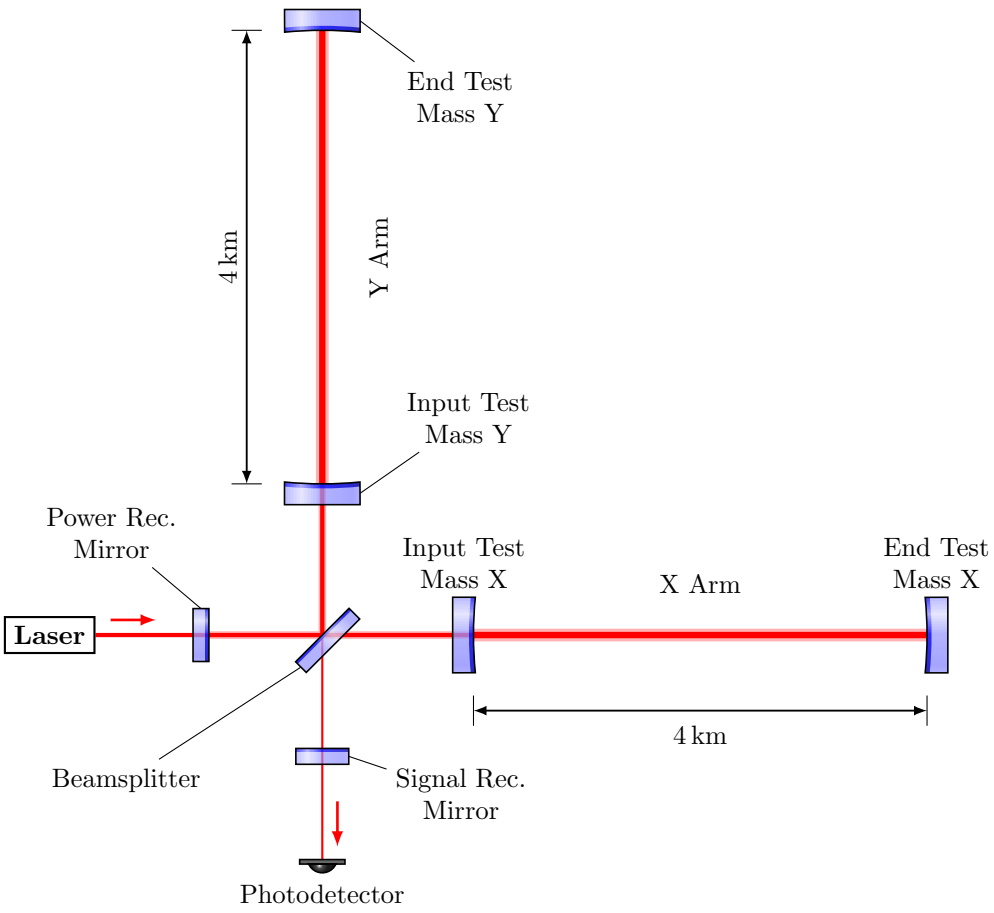

Figure 2.1: Main optics layout of an Advanced LIGO detector. A pre-stabilized Nd:YAG laser generates laser at $\lambda = 1064\,\mathrm{nm}$. The beam enters the dual-recycled Fabry-Perot Michelson Interferometer. Power fluctuations measured by the photodetector at the anti-symmetric port are proportional to changes in the apparent differential arm length.

Test masses of an aLIGO interferometer are 40 kg fused silica mirrors with diameters of 34 cm. To isolate from ground vibrations the test masses are suspended as the bottom stages of quadruple pendulum systems. Above the pendulum resonance frequencies the test masses are free to move in the longitudinal direction, thus they act as free-falling test masses. The masses themselves, i.e. the bottom stages of the quadruple pendulums, are attached to the next stage by fused silica fibers that reduce vibrations from thermal noise [57, 58].

One of the fundamental sensing noises is quantum shot noise. It scales proportionally to the inverse of the square-root of the laser power measured by the photodetector.

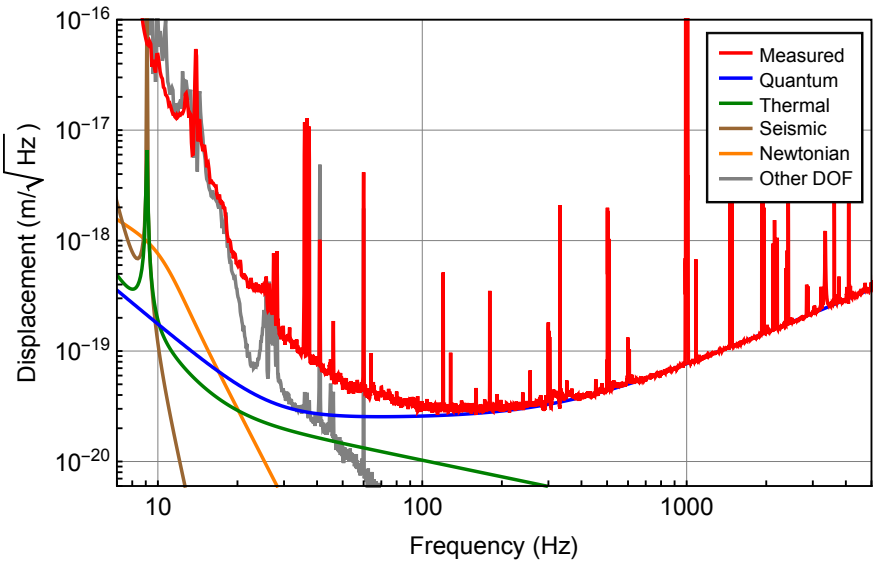

Figure 2.2: The displacement sensitivity of the Advanced LIGO detector in Hanford during the first observation run O1. Advanced LIGO sensitivity is limited both by the displacement noise, e.g. seismic activity, and and by the sensing noise, e.g. quantum shot noise (see Section 2.1.3). From [56].[3]

More detailed descriptions of the noise sources can be found in [56, 59].

2.2 Overview of the Advanced LIGO calibration

A gravitational wave passing through an interferometer causes its arm lengths fluctuate, i.e. to expand and contract. An interferometer, such as an Advanced LIGO detector, essentially measures variations in distances laser beams travel along the two interferometer arms. At the same time, the nominal operating state of the detector is maintained with a number of feedback control loops and the differential arm length is one of the degrees of freedom that is being controlled. The servo that suppresses fluctuations in the DARM length is called the DARM control loop. It is shown schematically in Figure 2.3.

The DARM control loop suppresses external disturbances to the differential arm length degree of freedom to keep the interferometer in the nominal operating state. Reconstruction of the unsuppressed DARM fluctuations induced by external sources such as GWs involves combining the

[3]Reprinted figure with permission from B. P. Abbott et al. *Phys. Rev. Lett.*, 116:131103, 2016 [56]. Copyright 2016 by the American Physical Society.

DARM loop error and control signals to produce a calibrated interferometer output signal. Accurate models of the DARM loop sensing and actuation function are required. Sensing and actuation transfer function measurements are made when the LIGO detector is operating in the so-called *nominal state* or *nominal configuration*. In this state, the laser beam of the interferometer is set to resonate in both of the Fabry-Perot arm cavities and both the power recycling and the signal recycling cavities are also locked at resonances.

The procedure for calibrating Advanced LIGO detectors consists of taking a set of measurements that enable determination of their responses to differential length variations during observation periods, i.e. when the detector is collecting science quality data. Advanced LIGO displacement calibration is traceable to the National Institute of Standards and Technology (NIST).

The GW-port output signal is denoted by d_{err}. The feedback signal is generated by passing d_{err} through a set of digital filters to generate the control signal, which then is sent to actuators on one of the test masses. An actuation signal is transferred to the force that displaces the test mass via the so-called *actuation function*. A function that converts the physical differential arm length displacement into the power at the antisymmetric port photodetector is called the *sensing function*.

2.3 Differential arm length control loop

The servo loop that keeps the differential arm length degree of freedom of the interferometer in a nominal state is called the *DARM control loop*. A block diagram of the loop is shown in Figure 2.3.

Due to interference, variations in the differential arm length produce power fluctuations at the antisymmetric port. These fluctuations are measured with photodetectors. The function that describes how the physical length fluctuations are converted to digital counts is called the *sensing function*, $C(f)$. Its output, the d_{err} signal, is defined as $d_{\mathrm{err}} \equiv C(f)\Delta L_{\mathrm{err}}$, where ΔL_{err} is the deviation of the differential arm length from its nominal value. The control loop passes this signal through a set of digital filters, $D(f)$, and sends it to test mass actuators. The test mass actuators are characterized by the *actuation function*, $A(f)$.

The response of the digital filters is fully described by the responses of infinite impulse response

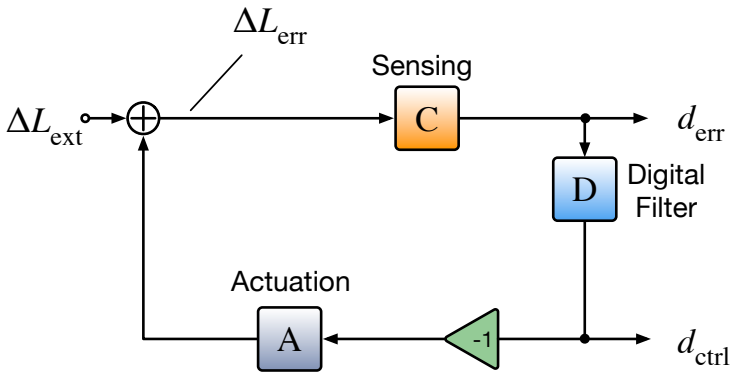

Figure 2.3: Schematic diagram of the differential arm length (DARM) control loop. Block "C" represents the sensing function, the response of the readout signal, $d_{\rm err}$, to changes in the apparent differential arm length, $\Delta L_{\rm err}$. Block "D" represents the digital control filters, and block "A" is the DARM actuation function that includes the transfer functions of the upper-intermediate (U), penultimate (P) and test mass (T) stages of the quadruple pendulum suspension system. Differential arm length disturbances from sources outside (external) the control loop, e.g. gravitational waves, are indicated by $\Delta L_{\rm ext}$. Error and control signals of the loop are represented by $d_{\rm err}$ and $d_{\rm ctrl}$.

filters designed to ensure the stable operation of the DARM loop. The sensing and actuation functions are modeled by characterizing their physical responses.

2.3.1 Sensing function

The *sensing function* represents the response of the dual-recycled Fabry-Perot Michelson interferometer (DRFPMI) to differential arm length fluctuations measured at the anti-symmetric port, also called the GW readout port. Power fluctuations at this port are measured with *DC photodetectors*.[4] The output of these photodetectors is the DARM error, $d_{\rm err}$ signal (see Figure 2.3).

A detailed analytic form for the aLIGO detector response can be found in a recent study performed by Izumi and Sigg [61]. A frequency-domain model of the sensing function includes a simplified coupled-cavity response, the signal recycling cavity detuning and a delay associated

[4]The DARM error signal is produced from the sum of two sensor outputs. They are called the DCPD A and DCPD B (see the 'aLIGO DARM Signal Chain' diagram [60]). However, because in the DARM loop relies on (and sees only) the sum of the two outputs, the sensing function is modeled as an output of a single photodetector.

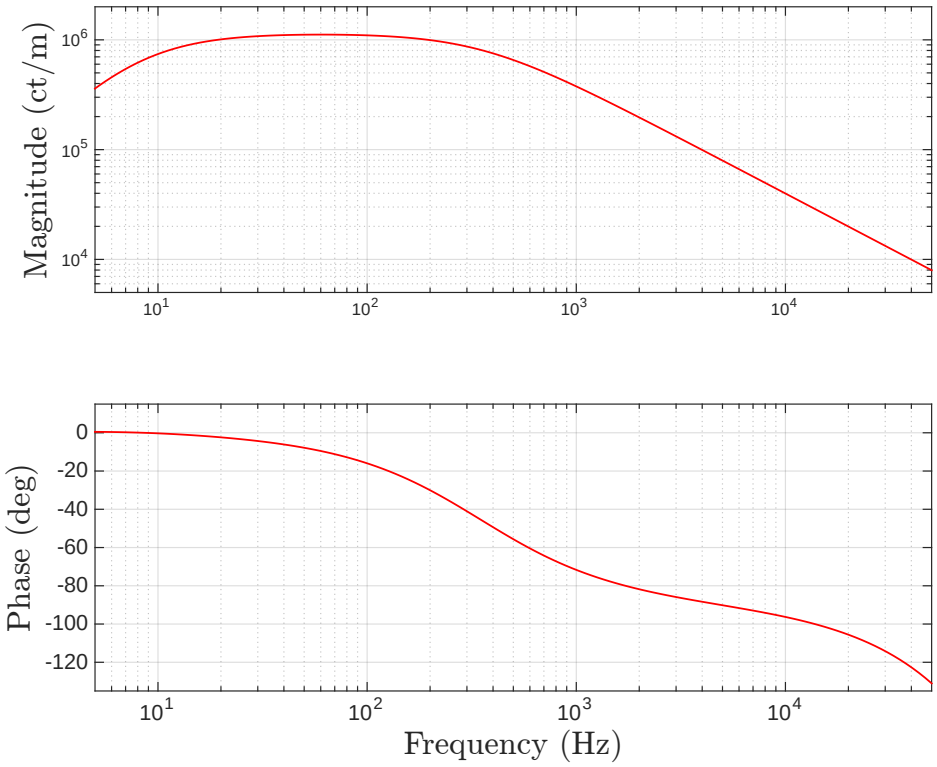

Figure 2.4: Bode plot of the LIGO Hanford DARM loop sensing function for the O2 run. The optical gain scales the magnitude of the sensing function. At frequencies below $\sim$ 10 Hz, the frequency dependent response of the sensing function is dominated by the signal recycling cavity detuning. At frequencies near and above the coupled-cavity pole frequency ($\sim$ 350 Hz), the response is dominated by the coupled-cavity response of the interferometer, in addition to that the phase is also affected by the delay of the response arising from the light travel time in the arms.

with the light travel time in the 4-km-long arms of the interferometer (see Figure 2.4):

$$C_0(f) = \frac{\mathcal{K}_\mathrm{C}}{1 + if/f_{\mathrm{C},0}} \frac{f^2}{f^2 + f_{\mathrm{S},0}^2 - if f_{\mathrm{S},0}/Q_{\mathrm{S},0}} e^{2i\pi f \tau_\mathrm{C}} \tag{2.14}$$

where the first fraction, $\frac{\mathcal{K}_\mathrm{C}}{1 + if/f_{\mathrm{C},0}}$, is a low-frequency approximation of the coupled-cavity response; the second fraction, $\frac{f^2}{f^2 + f_{\mathrm{S},0}^2 - if f_{\mathrm{S},0}/Q_{\mathrm{S},0}}$, is an approximation of an optical spring response due to a detuned signal recycling cavity; and the exponent represents the frequency response from a delay from the light travel time along 4-km-long interferometer arms. More specifically, $f_{\mathrm{C},0}$ is the coupled-cavity pole frequency, $\mathcal{K}_\mathrm{C}$ is the optical gain, $f_{\mathrm{S},0}$ and $Q_{\mathrm{S},0}$ are the optical spring frequency and its Q factor, τ_C is the time delay, and f is the frequency at which the sensing

function is evaluated. The subscript 0 indicates that a quantity or a function is evaluated at the reference time, $t = t_0$, e.g. $f_{\mathrm{C},0}$ is the reference-time coupled-cavity pole frequency. This notation is needed because parameters κ_{C}, f_{C}, f_{S} and Q_{S} change slowly over time. A method for tracking and compensating for these slow temporal variations is discussed in Chapter 3. The reference-time model parameters, $\mathcal{K}_{\mathrm{C}}$, f_{C}, f_{S}, $1/Q_{\mathrm{S}}$, τ_{C}, were determined with a maximum likelihood search. The generative model for the search was based on Eq. 2.14.

The two parameters of the signal recycling cavity detuning are new to the sensing model for the O2 run. A study by Hall *et. al.* [62] showed that the discrepancy of the LIGO Hanford sensing model for the O1 run at low frequencies can be explained by small detuning of the signal recycling cavity. Further investigations of this effect showed that the f_{S} and Q_{S} parameters vary over time [63]. However, this effect was not yet characterized and included into the sensing model before the O1 run. These parameters have not yet been incorporated into the method for tracking temporal variations (see Chapter 3).

2.3.2 Actuation function

Advanced LIGO test masses are fused-silica mirrors suspended as the lowest stages of the quadruple pendulum system [58, 65]. The main purpose of this suspension system is to provide seismic isolation to the longitudinal motion of the test mass [57]. The suspension system allows the test mass to move freely along the axis of the main interferometer beam. Each quadruple pendulum system supporting a test mass is coupled with a chain of reaction masses, called the *reaction chain*. Stages of the reaction chain masses are equipped with actuators that can apply forces to the corresponding masses in the pendulums that support the test mass. The actuators on the lower three stages, the upper-intermediate, the penultimate mass and the test mass stage, are used by the DARM servo. Thus, the actuation function includes the responses of these actuators to the displacement of the test mass, $A_{\mathrm{U}}(f)$, $A_{\mathrm{P}}(f)$ and $A_{\mathrm{T}}(f)$, as shown in Figure 2.6.

Forces to the penultimate (PUM) and upper-intermediate (UIM) masses are applied through a set of coil-magnet actuators on the corresponding stage of the reaction chain. Actuation of

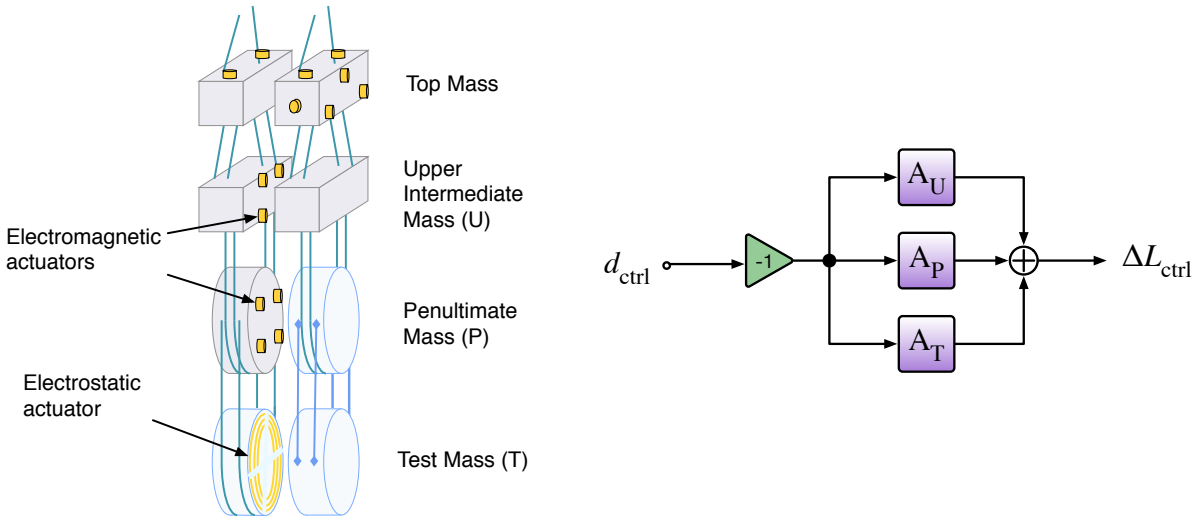

Figure 2.5: *Left:* Quadruple pendulum suspension system. Actuators of the three bottom stages, the upper-intermediate mass (U), penultimate mass (P) and test mass (T), are used for DARM loop actuation. From [64]. *Right:* Schematic diagram of the DARM loop actuation. Blocks "A_{U}," "A_{P}" and "A_{T}" represent the responses of the test mass displacement to the requested actuation signals sent to the upper-intermediate, the penultimate mass and the test mass stage actuators.

the upper-intermediate stage is strongest below $\sim$ 10 Hz and it drops rapidly as the frequency increases. The penultimate stage actuators are dominant from $\sim$ 10 Hz to $\sim$ 35 Hz. The test mass stage actuation is accomplished with an electrostatic force actuator, also denoted as the electrostatic drive (ESD). Actuation of this stage is dominant above $\sim$ 35 Hz. However, due to the pendulum response, its actuation to displacement response drops as $1/f^2$. Dynamical responses of the three actuation stages are shown in Figure 2.6.

2.4 Transfer function measurements

The characterization of the DARM sensing and actuation functions requires making multiple-frequency measurements of their responses. The primary tools used for taking these measurements are Advanced LIGO Photon Calibrators (discussed in Chapter 4). These actuators induce fiducial displacements of test masses with radiation pressure from auxiliary laser beams.

The sensing transfer function is obtained from two multiple-frequency measurements: *a)* the

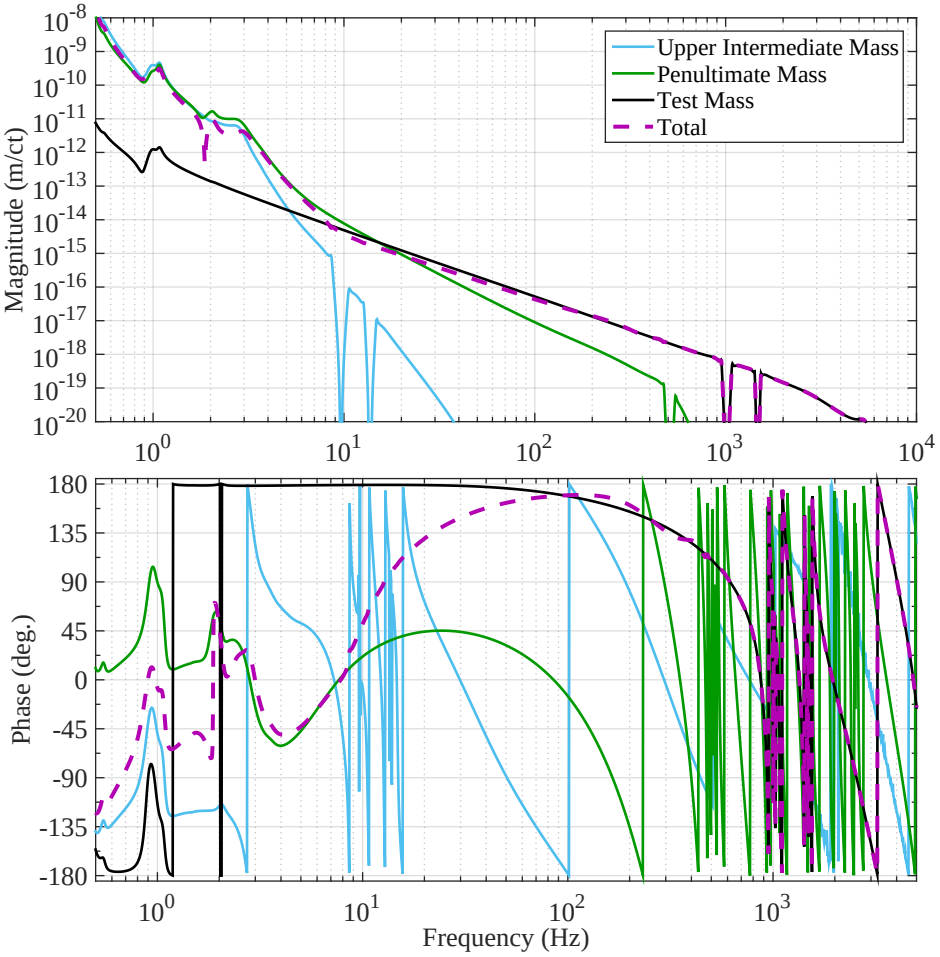

Figure 2.6: Bode plot of the DARM loop actuation function model. The functions show the response of the test mass to the upper-intermediate mass, penultimate mass and test mass stage actuators at LIGO Livingston. From [64].[5]

response of the DARM loop, d_{err}, to sinusoidal excitations injected into the DARM control signal and *b)* its response to excitations from Photon Calibrators. The first measurement allows the evaluation of the DARM loop suppression effect and the second measurement provides a transfer function of the sensing function suppressed by the loop. Frequency vectors for the two transfer function measurements are chosen to be identical so that the loop suppression effect can be excluded by taking the ratio of the two measurements.

Transfer functions of each of the suspension stage actuators are also estimated from a pair of

[5]Reprinted figure with permission from B. P. Abbott et al. *Phys. Rev. D*, 95:162003, 2017 [64]. Copyright 2017 by the American Physical Society.

multiple-frequency measurements. For a given stage i, where $i \in \{\mathrm{U}, \mathrm{P}, \mathrm{T}\}$, its actuation function is obtained by *a)* injecting excitations into the control signal of the measured actuators, x_i and *b)* injecting excitations via the Photon Calibrator. Then, the ratio of the two responses (also taken on an identical frequency vector) gives the measurement of the actuation transfer function $A_i(f)$.

2.5 Estimation of the model parameters

Throughout past observational periods of Advanced LIGO, the calibration methods used for estimation of the interferometer parameters have evolved. Descriptions of calibration procedures for measuring and estimating the sensing and actuation function parameters that were utilized in the first observational period (the O1 run) are given in [64].

Methods used for obtaining the sensing and actuation parameters in the second observing run, i.e. the O2 run, are briefly described in this section. Bayesian confidence intervals reported in this section account for statistical uncertainties associated with multiple-frequency measurements of the sensing and actuation transfer functions. Overall uncertainties, that incorporate other sources of systematic errors, e.g. absolute power calibration of Photon Calibrator sensors and residual frequency-dependent systematic errors in the response function, are reported in [66].

2.5.1 Parameters of the sensing function

Fitting parameters for the sensing model are optical gain, coupled-cavity pole frequency, time delay, optical spring frequency and the inverse of its Q factor, denoted by $\boldsymbol{\theta} = \{\mathcal{K}_{\mathrm{C}}, f_{\mathrm{C}}, \tau_{\mathrm{C}}, f_{\mathrm{s}}, Q_{\mathrm{s}}^{-1}\}$. The likelihood function is given by

$$p(\boldsymbol{\theta}, \{d_n\}) = -\sum_n \left[\frac{|d_n - C(f_n, \boldsymbol{\theta})|^2}{2\sigma_n^2} - \log\left(\frac{\sqrt{2\pi}\sigma_n}{C(f_n, \boldsymbol{\theta})} \right) \right], \tag{2.15}$$

where f_n are frequencies at which the multiple-frequency transfer function measurements, d_n, were made, and σ_n are statistical uncertainties associated with the data points. The particular maximum likelihood search technique used for estimating the sensing model parameres for the O2 run was

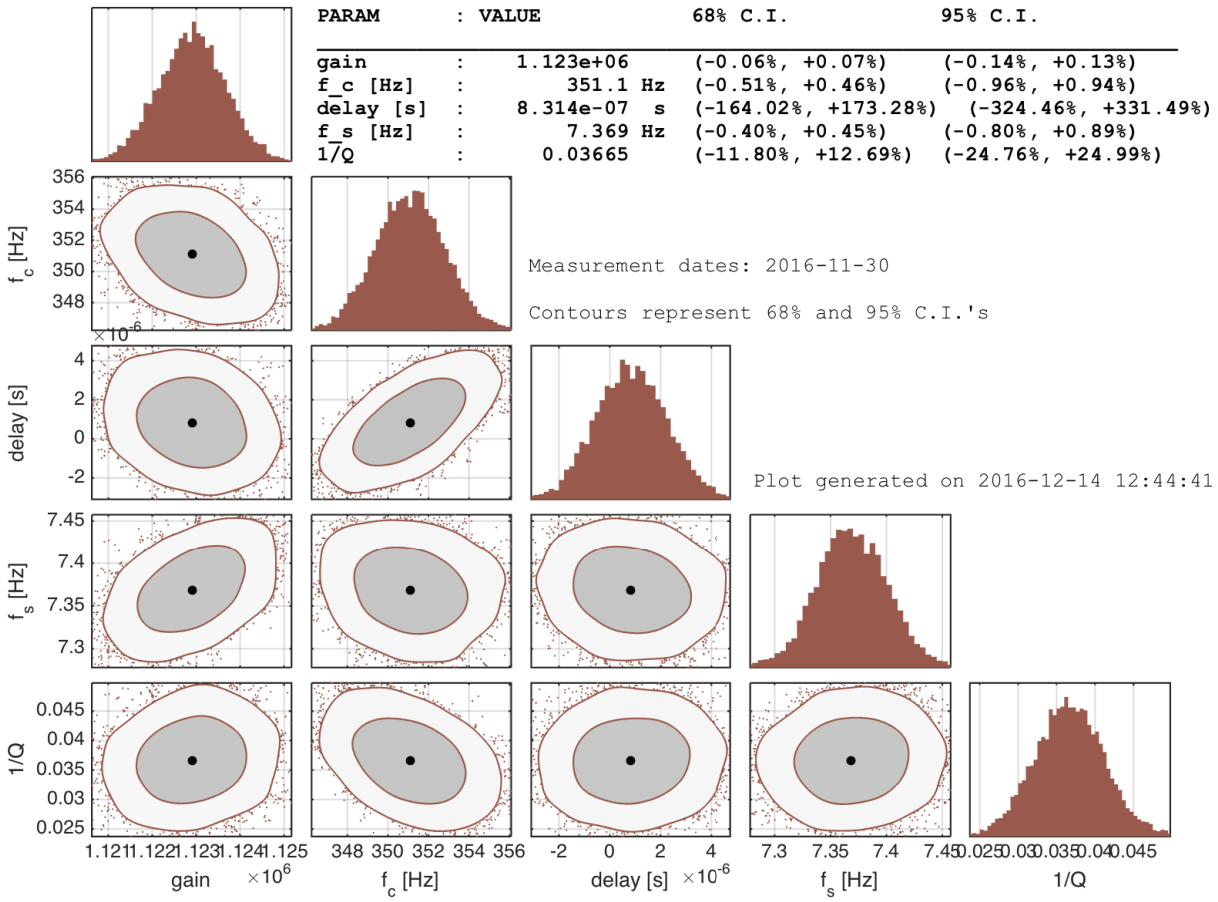

Figure 2.7: Estimation of the DARM loop sensing function parameters for the O2 run at LIGO Hanford. The parameters were estimated with the Markov Chain Monte Carlo search (MCMC). A verification of these results with an alternative search method can be found in a study by E. Goetz *et al.* in [67].

an implementation of the Markov Chain Monte Carlo (MCMC) method. The fitting results are shown in Figure 2.7. Parameter values estimated with this method were compared to the values found by another search that utilized a MATLAB function, `nlinfit()`.[6] While this study, that was reported in [67], concluded that the two methods converge to the same values, is was shown that the MCMC search gives more robust confidence intervals compared to the `nlinfit()`-based method.

[6]The MCMC search was implemented in two languages: MATLAB and Python. The `nlinfit()`-based method was implemented in MATLAB.

2.5.2 Parameters of the actuation function

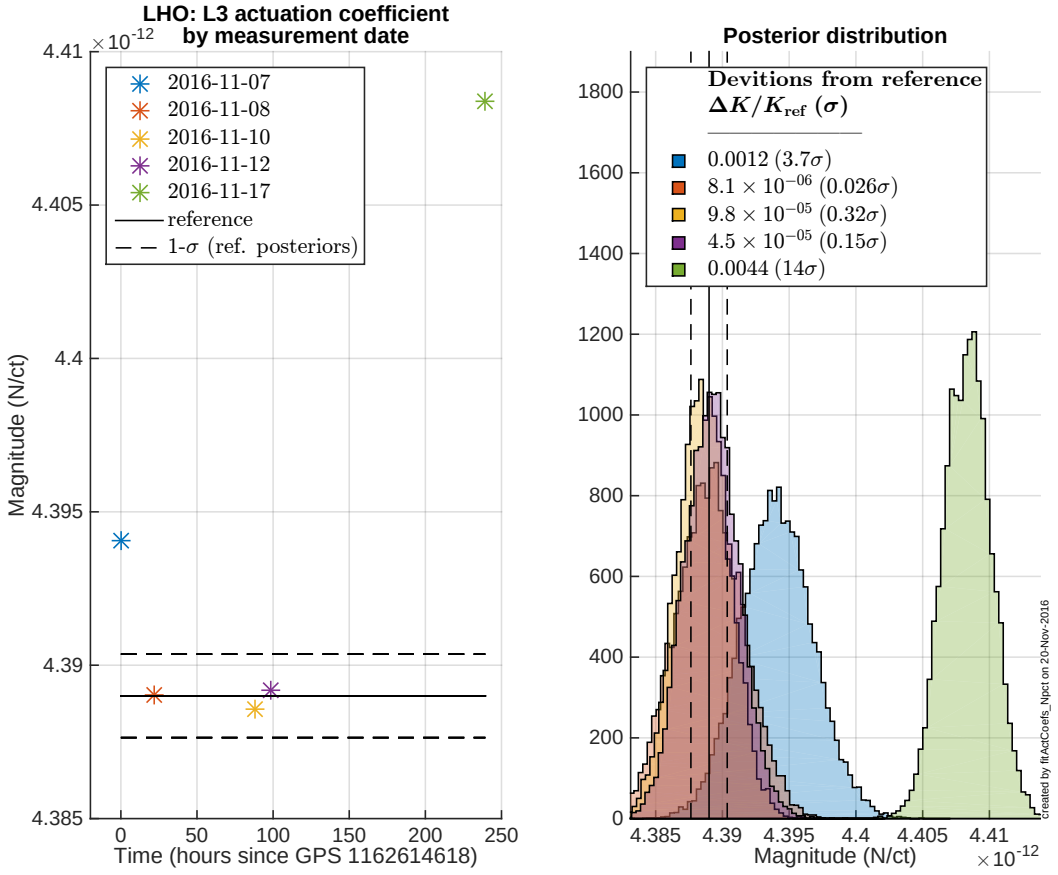

Figure 2.8: Estimation of the Force coefficient of the electrostatic driver (ESD) for the O2 run. The ESD force coefficient value for the LIGO Hanford detector was based on transfer function measurements taken on November 8 – 12, 2016.

For each of the suspension stage actuation functions a scalar force coefficient is estimated. Given stage i for $i \in \{\mathrm{U}, \mathrm{P}, \mathrm{T}\}$, the actuation function of this stage is $A_i(f)$ which is written in the form of a normalized, frequency-dependent part, $\hat{A}_i(f)$, and a scalar force coefficient, $\mathcal{K}_i$, thus

$$A_0(f) = \left[\mathcal{K}_\mathrm{T}\hat{A}_\mathrm{T}(f) + \mathcal{K}_\mathrm{P}\hat{A}_\mathrm{P}(f) + \mathcal{K}_\mathrm{U}\hat{A}_\mathrm{U}(f)\right] e^{2\pi i f \tau_A} \tag{2.16}$$

In the procedure for determining force coefficients each of the scalar coefficients, $\mathcal{K}_i$ is estimated

independently based on measurements for the respective suspension stage. Thus, likelihood functions used for estimating these coefficients can be written as

$$p(\mathcal{K}_i, \{d_n\}) = -\sum_n \left[\frac{|d_n - \mathcal{K}_i|^2}{2\sigma_n^2} - \log\left(\frac{\sqrt{2\pi}\sigma_n}{\mathcal{K}_i} \right) \right], \tag{2.17}$$

where σ_n are statistical uncertainties associated with the measurements. Data that enter the actuation parameter estimation search are the multiple-frequency transfer function measurement results divided by normalized models, i.e. $d_n = A_{i,\mathrm{meas}}(f_n)/\hat{A}_i(f_n)$. The example of fitting the electrostatic driver force coefficient, $\mathcal{K}_\mathrm{T}$, is shown in Figure 2.8. Details of this analysis are reported in [68].

Chapter 3: TIME-VARYING PARAMETERS

The calibration process of the Advanced LIGO sensing and actuation functions that was discussed in Chapter 2 summarizes the construction of the DARM loop model and estimated values of the model parameters. These models determine the accuracy of the reconstructed GW strain time-series. The strain signal together with the measurement uncertainties constitute a complete set of information reported by the calibration group, that is incorporated into GW signal analyses. For a system which does not evolve during the course of an observation period, the initial calibration parameters and the uncertainties associated with them remain applicable to the instrument outputs throughout the given period. However, both the aLIGO sensing and the actuation functions have inherent temporal dependences, i.e. they are changing over time. As a consequence, the overall response of the DARM control loop is also a time-varying function. Characterizing and compensating for these temporal dependences is one of the important issues that need to be addressed in the ground-based advanced GW detectors.

This chapter discusses the method for tracking temporal variations in the response function and compensating them in the computation of the GW strain time series. The method uses periodic excitations continuously injected via the actuators of the DARM control loop and via the Photon Calibrator tool (discussed in Chapter 4). It was utilized to address the temporal variations during the first and second observational periods of Advanced LIGO [64, 66, 69].

The chapter starts with a description of physical effects that likely cause temporal variations in the sensing and actuation functions of the Advanced LIGO detectors (Section 3.1). The description of the method for tracking the temporal variations and compensating for these variations in the calibrated GW strain signal is given in Section 3.2. Aspects of implementing the method in the aLIGO infrastructure are discussed in Section 3.3. The results of employing this method in the first and second observation periods of Advanced LIGO (the O1 and O2 runs) are reported in Section 3.4. Lastly, Section 3.5 explores possible research directions that can help to further improve the time-varying calibration of the detectors. Scientific implications of the results are discussed

separately in Chapter 5.

3.1 Temporal variations in Advanced LIGO

The time-dependence of the differential arm response is not unique to the Advanced LIGO interferometer. In the Initial LIGO detectors, all of the slow temporal variations in the DARM loop were attributed to frequency-independent changes in the total optical gain of the sensing function [70]. However, since the detectors in the Advanced LIGO configuration are more complex compared to the Initial LIGO detectors, they experience an increased complexity of time-dependences in the response function. Hence, the time-dependences of the Advanced LIGO response function cannot be described with a simple frequency-independent scaling factor, but rather require a set of parameters that alter the response function in a frequency-dependent manner.

The sensing function of an Advanced LIGO interferometer includes the optical response of the signal recycled Fabry–Pérot Michelson interferometer and the frequency dependence of the output readout photodetector electronics [64].

The optical gain and coupled-cavity pole frequency vary due to slow drifts in the alignment and the thermal state of the main interferometer mirrors. Drifts in the alignment of the interferometer optics can be caused by temperature fluctuations inside of the buildings. Thermal distortion of mirrors caused by laser power in the cavities affect the spatial eigenmodes of the arm cavities and the signal recycling cavity. Changes in the mode-matching between these cavities alter the coupled-cavity (CC) pole frequency. Lowering of coupled-cavity pole frequency reduces the signal recycling gain.

The test masses of an Advanced LIGO detector are suspended as the final stages of quadruple pendulum suspension systems forming free-swinging but damped systems [71]. The suspensions isolate the test masses from seismic disturbances and other environmental noise sources. The DARM control loop uses the last three stages of the quadruple pendulum system: the upper-intermediate (U), penultimate (P) and the test mass (T) stages. The upper-intermediate and the penultimate stages use voice coil actuators, and the test mass stage uses an electrostatic force actu-

ator (electrostatic driver, ESD). The upper-intermediate stage actuators are dominant below 5 Hz, the penultimate stage between 5 and 20 Hz and the test mass stage above 20 Hz. Details of actuation stage authority are discussed in greater detail in [64]. The actuation function is the transfer function between a signal sent to the actuators and the induced displacement of the test mass at the end of a detector arm (end test mass, ETM).

Changes in the strength of the electrostatic actuator are attributed to charge accumulation and drift in the bias voltage [72, 73]. Coil-magnet actuators of the upper-intermediate mass and penultimate mass suspension stages are similar to the ones earlier used in the Initial LIGOdetectors [70]. Despite the fact that strengths of these actuators are not expected to evolve over time, tracking their responses can help reveal unexpected problems in their respective electronics chains early on.

An effect that was discovered after the method for tracking temporal variations reported here had been implemented in the aLIGO infrastructure is the response of the detuned signal recycling cavity. Thus, tracking of variations caused by detuning of the signal recycling cavity has not been incorporated into the method. Close to the end of the O1 run, a study showed that changes in the coupling of the signal recycling cavity produced variations in the sensing response of the LIGO Hanford detector at low frequencies [62]. Measurements showed agreement with the theoretical predictions of the effect described in [74]. This effect was included into the sensing model for the O2 run as a static function of frequency (see Section 2.3).

3.2 Method for compensating for slow temporal variations

This section explains the method used for tracking and compensating for slow temporal variations in the differential arm length response of the aLIGO detectors. Subsection 3.2.1 outlines how the temporal variations have been incorporated into parameters of the sensing and actuation functions. Parametrizing the time-dependences is helpful for analyzing possible changes in the shape of the response function; it enables us to look at the known systematic calibration errors that can be minimized by adjusting the parameters to compensate for these variations. If temporal variations are not compensated, the maximum possible systematic errors would have to be included in the

uncertainty budget of the Advanced LIGO calibration. Prior estimates of such systematic errors obtained by simulating small variations in the model parameters are given in Subsection 3.2.2. Details of the method for tracking and compensating these variations, by injecting periodic excitations into the DARM control chain and by directly exciting the test mass with Pcal, are given in Subsection 3.2.3.

3.2.1 Introduction of the time-dependent parameters

The DARM loop response is modeled in terms of a sensing function, digital filters and an actuation function. Transfer function measurements, discussed in Chapter 2, are used to determine initial values of the sensing and actuation model parameters. These parameters produce the *reference-time models* of the sensing and actuation functions. They remain valid within a limited time interval (close to the time when the measurements were made).

Extended forms of the sensing and actuation models introduced in this chapter, which were previously given as time-independent functions of frequency alone (see Chapter 2), are functions of both frequency and time.

In the model of the sensing function, the time dependence of the optical gain is represented by a multiplicative factor $\kappa_{\mathrm{C}}(t)$ and temporal variations in the coupled cavity (CC) response are approximated by the absolute value of the CC pole frequency, $f_{\mathrm{C}}(t)$. A complete analytic form of the optical response of an aLIGO detector can be found in a recent study by Izumi and Sigg [61]. The analytic form of the time-dependent sensing function can be written as

$$C(f,t) = \frac{\kappa_{\mathrm{C}}(t)}{1 + if/f_{\mathrm{C}}(t)}\, Q(f) \equiv S(f,t)\, Q(f), \tag{3.1}$$

where the two functions $Q(f)$ and $S(f,t)$ represent the static and time-dependent parts of the sensing function respectively. $Q(f)$ includes the DC photodetector response to laser power, responses of the electronics in the sensing chain, and the signal delay from the light travel time in the 4 km-long interferometer arms. The time-dependent portion of the sensing model includes the optical gain scaling factor, $\kappa_{\mathrm{C}}(t)$, and a single pole function $1/\big(1 + if/f_{\mathrm{C}}(t)\big)$ which represents an

approximated coupled cavity response of the detector.

It is useful to reiterate some facts about the actuation function of the DARM loop before considering its parameters. Currently the loop relies on the actuators of the three bottom stages of the quadruple suspension system: the upper-intermediate (U), penultimate mass (P) and test mass (T) stages. The actuation model is constructed as a sum of the $A_{\rm U}$, $A_{\rm P}$ and $A_{\rm T}$ terms that represent the actuator responses of the individual stages. As was explained in Section 3.1, temporal variations in the actuation function are expected to arise primarily from changes in the strength of the test mass stage actuator. These changes are represented in the model by a scaling factor $\kappa_{\rm T}(t)$. Another scaling factor, $\kappa_{\rm PU}(t)$ is set to represent potential changes in the remaining terms, the combined responses of the upper-intermediate and penultimate mass stages. Their stability can be assessed by tracking this value. Incorporating these scale factors in terms of the reference-time models, the actuation function can be written as

$$A(f,t) = \kappa_{\rm PU}(t)\big(A_{\rm P,0}(f) + A_{\rm U,0}(f)\big) + \kappa_{\rm T}(t)A_{\rm T,0}(f). \tag{3.2}$$

In this equation and throughout this chapter the subscript "0" is used to indicate that a function is evaluated at the reference time, t_0. The nominal values (at $t = t_0$) of the factors $\kappa_{\rm PU}$ and $\kappa_{\rm T}$ are set to 1.0.

3.2.2 Prior estimations of systematic errors from slow temporal variations

After parametrizing the drifts in the sensing and actuation responses with the time-dependent model parameters, it is possible to estimate the effect of the temporal variations on the systematic errors associated with the GW strain signal.

Variations in the DARM control loop response, if not compensated for, can affect the systematic errors in the reconstruction of $\Delta L_{\rm ext}$. The parameters that were introduced above can help to estimate potential errors as a function of frequency. One way of doing it would be to take the reference-time model of the DARM loop response (constructed from the reference-time sensing and actuation models) in the frequency domain and comparing it to a model with slightly altered

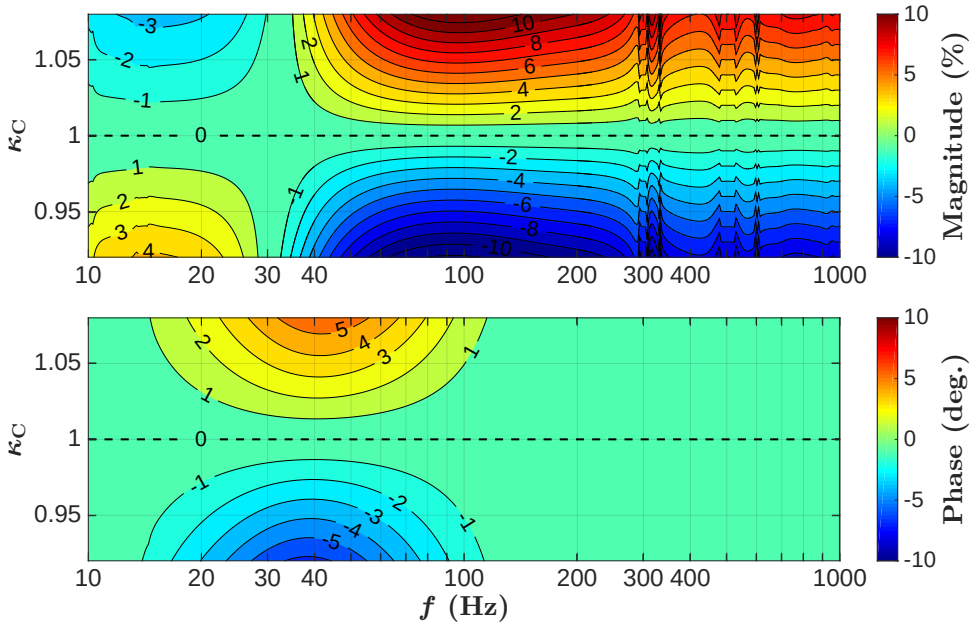

Figure 3.1: Estimated systematic calibration errors in the magnitude and phase of the response function resulting from uncorrected changes in the scale factor for the sensing function, κ_C. Solid lines represent boundaries of ± 1 %, ± 2 %, ± 3 %, etc. From [69].[7]

parameter values.

Potential systematic errors in the reconstruction of $\Delta L_{\rm ext}$ produced by varying the optical gain scaling factor are presented in Figure 3.1. Well above the unity gain frequency of the DARM loop the response function is dominated by the sensing function, i.e. $R(f) \simeq 1/C(f)$ for $|G| \ll 1$. This explains the stronger impact of the variations in the optical gain at higher frequencies.

Contrary to that, as shown in Figure 3.2, variations in the coupled cavity pole frequency produce the strongest effect near and above the pole frequency, leaving the lower frequency band of the response function virtually unaffected. The nominal cavity pole frequency of the reference-time model for the LIGO Hanford detector is 341 Hz.

Variations in the actuation function mostly affect the DARM response below the unity gain frequency, $R(f) \simeq A(f)\, D(f)$ for $|G| \gg 1$. Magnitudes of the test mass stage actuation and the sum of the upper-intermediate and penultimate mass actuation responses cross at approximately

[7]Reprinted figure with permission from D. Tuyenbayev, S. Karki, J. Betzwieser, et al. *Classical and Quantum Gravity*, 34(1):015002, 2017 [69]. Copyright 2016 IOP Publishing Ltd.

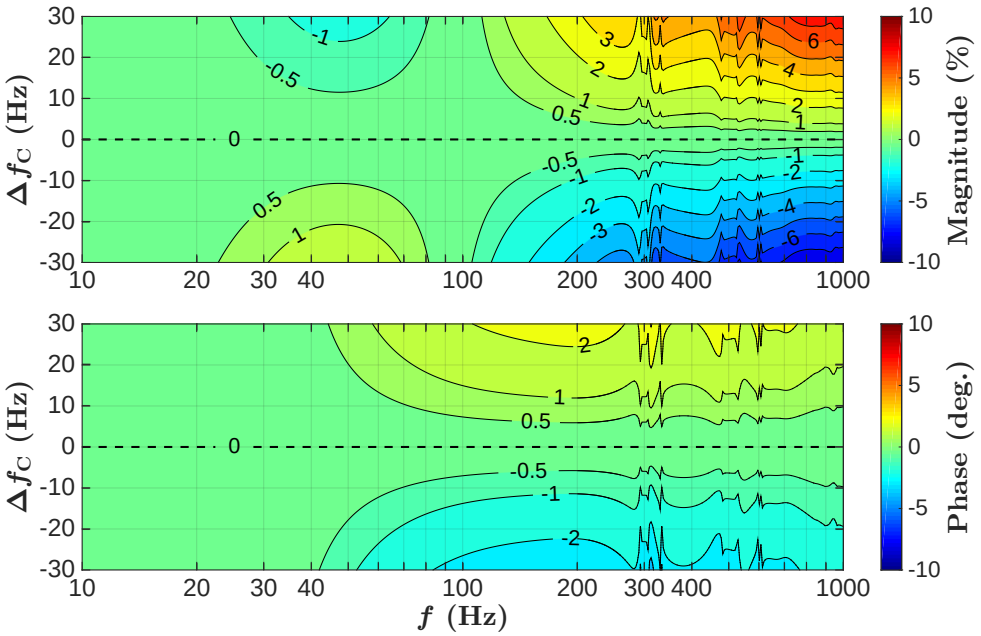

Figure 3.2: Estimated systematic calibration errors in the response function of the detector from uncorrected changes in the coupled cavity pole frequency, Δf_{C}. Solid lines represent boundaries of ± 0.5 %, ± 1 %, ± 2 %, ± 3 %, etc. From [69].[7]

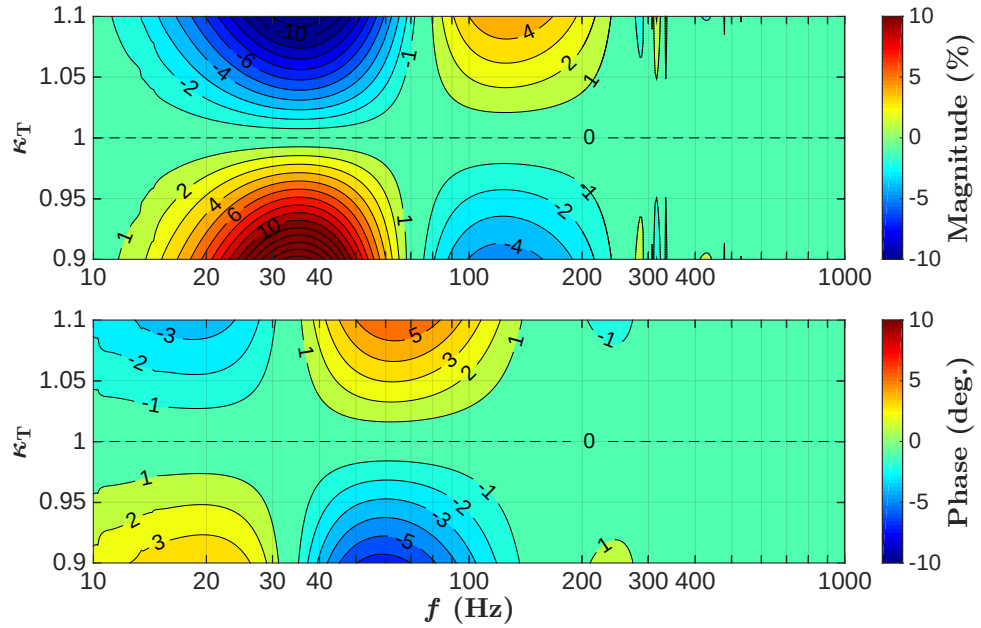

Figure 3.3: Estimated fractional systematic calibration errors from uncorrected scalar changes in the test mass stage actuation, κ_{T}. Solid lines represent boundaries of ± 1 %, ± 2 %, ± 3 %, etc. systematic error regions and the case for the nominal value of κ_{T} is indicated with a dashed line. From [69].[7]

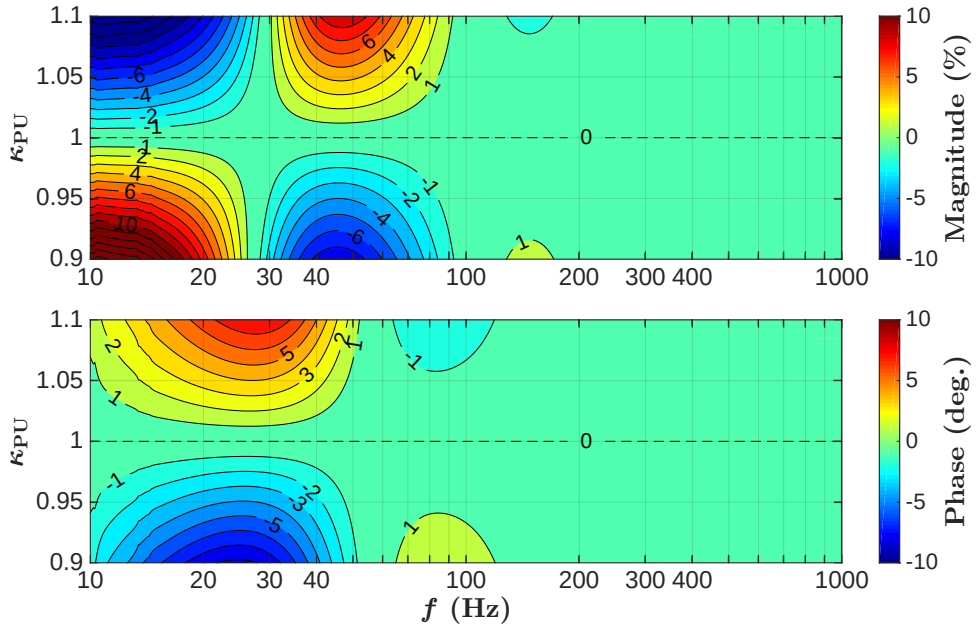

Figure 3.4: Estimated systematic calibration errors from uncorrected scalar changes in the combined actuation of the upper-intermediate and penultimate mass stages, κ_{PU}. Solid lines represent boundaries of ± 1 %, ± 2 %, ± 3 %, etc. systematic error regions and the case for the nominal value of κ_{PU} is indicated with a dashed line.

30 Hz, above which the former is stronger. Thus, as shown in Figure 3.3, changes in the strength of the test mass stage actuator produce the strongest variations in the DARM response in the frequency band from 20 to 60 Hz (as was noted above, at higher frequencies the DARM response is dominated by the sensing function).

One might also look into possible systematic errors due to deviations of the κ_{PU} from its nominal value (see Figure 3.4). Although, as was discussed in Section 3.1, it is unlikely that κ_{PU} will drift significantly over time, a non-unity value of κ_{PU} could still indicate biases in the initial model parameters or some failure in the actuator electronics.

3.2.3 Tracking and compensating temporal variations

For a given input signal, provided that the parameters of a linear system are known, it is possible to calculate the form of the expected output signal. Any mismatches between the calculated and the measured signals would indicate that the real response of the loop deviates from the initial model. Therefore, assessment of temporal changes of a linear system's parameters can be made by continuous measurements of the responses of the system to a set of excitations.

Analysis of the transfer function measurements of the DARM loop (see Chapter 2) gives initial forms (models) of the sensing and actuation functions, their reference-time representations. Temporal variations in the parameter values of the models can be then monitored by injecting periodic excitations, i.e. *calibration lines*, into specific locations of the DARM loop and observing the DARM error signal (output signal) time series. Figure 3.5 shows injection points of the calibration lines, $x_{\rm pcal}$, $x_{\rm ctrl}$ and $x_{\rm T}$, in the DARM control loop.

Of course, the primary purpose of DARM error signal is to measure gravitational waves. Any disturbances of the DARM signals, such as deliberate excitation signals, can potentially compromise measurements of GWs. Thus, it is important that during GW observation periods a sufficient but not excessive number of frequencies are set aside for calibration purposes.

Each of the aLIGO Pcal systems is capable of injecting modulated excitations, i.e. calibration lines, into the differential arm length response. A Pcal calibration line is produced by sinusoidally modulating the power of the Pcal beams (see Chapter 4), which translate into sinusoidal modulations in the radiation pressure from the beams. The physical displacements of a test mass, however, are suppressed by the DARM control loop. Measurements of these displacements in the $d_{\rm err}$ signal at any given time t' are given by

$$d_{{\rm err},t'}(f_{\rm pcal1,2}) = \frac{C(f,t)}{1+G(f,t)} x_{{\rm pcal},t}(f) \Big|_{f=f_{\rm pcal1,2},\, t=t'} \tag{3.3}$$

where $f_{\rm pcal1}$ and $f_{\rm pcal2}$ are frequencies of the two Pcal lines that are used, as discussed further in this section, for tracking the actuation and sensing parameters. Variables $d_{{\rm err},t}(f)$ and $x_{{\rm pcal},t}(f)$

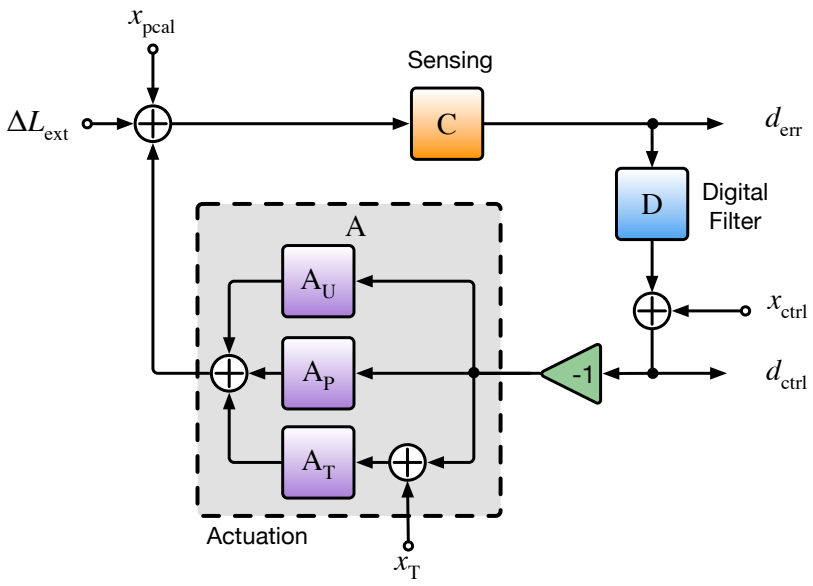

Figure 3.5: Schematic diagram of the differential arm length control loop. Block "C" represents the sensing function, the response to changes in the apparent differential arm length; block "D" represents the transfer function of the digital control filters; and blocks "A_{U}," "A_{P}" and "A_{T}" are the actuation transfer functions of the upper-intermediate (U), penultimate (P) and test mass (T) stages of the quadruple pendulum suspension system. Differential arm length disturbances from sources outside (external) the control loop, e.g. GWs, are denoted by ΔL_{ext}. Injection points for modulated sinusoidal excitations (calibration lines) are denoted by: x_{pcal} – excitations from a photon calibrator (Pcal), x_{ctrl} – excitations injected into the DARM control signal, and x_{T} – excitations injected into the test mass actuation stage. Error and control signals are represented by d_{err} and d_{ctrl}. From [69].[7]

represent complex values in the frequency domain.

A calibration line injected into the overall DARM actuation, i.e. the location x_{ctrl} in the DARM diagram (see Figure 3.5), produces a response given by

$$d_{\mathrm{err},t'}(f_{\mathrm{ctrl}}) = \frac{-A(f,t)\,C(f,t)}{1+G(f,t)} x_{\mathrm{ctrl},t}(f)\,\Big|_{f=f_{\mathrm{ctrl}},\,t=t'}. \tag{3.4}$$

Similarly, the response of the DARM loop to an excitation injected into the test mass stage actuators alone, i.e. x_{T}, is given by

$$d_{\mathrm{err},t'}(f_{\mathrm{T}}) = \frac{\kappa_{\mathrm{T}}(t) A_{\mathrm{T},0}(f)\,C(f,t)}{1+G(f,t)} x_{\mathrm{T},t}(f)\,\Big|_{f=f_{\mathrm{T}},\,t=t'} \tag{3.5}$$

With the $x_{\mathrm{T}}(f_{\mathrm{T}})$, $x_{\mathrm{ctrl}}(f_{\mathrm{cltr}})$ and $x_{\mathrm{pcal}}(f_{\mathrm{pcal1}})$ calibration lines placed at nearby frequencies, variations of the actuation parameters are monitored as described below. The expression for tracking temporal variations in the test mass stage actuation, parametrized with the κ_{T} scaling factor, is obtained by taking the ratios of Equations (3.5) and (3.3), and solving for $\kappa_{\mathrm{T}}(t)$:

$$\kappa_{\mathrm{T}}(t) = \frac{1}{A_{\mathrm{T},0}(f_{\mathrm{T}})} \frac{d_{\mathrm{err},t}(f_{\mathrm{T}})}{x_{\mathrm{T},t}(f_{\mathrm{T}})} \left(\frac{d_{\mathrm{err},t}(f_{\mathrm{pcal1}})}{x_{\mathrm{pcal},t}(f_{\mathrm{pcal1}})} \right)^{-1} \frac{C_0(f_{\mathrm{pcal1}})}{1 + G_0(f_{\mathrm{pcal1}})} \left(\frac{C_0(f_{\mathrm{T}})}{1 + G_0(f_{\mathrm{T}})} \right)^{-1}, \tag{3.6}$$

where C_0 and G_0 are the sensing and DARM open loop transfer functions at the reference time $t = t_0$ and x_{pcal} is a calibrated length modulation induced by the photon calibrator. For typical variations in the DARM parameters, the shape of the overall DARM response function in a narrow frequency band of few hertz does not vary by more than a small fraction of a percent. This allows us to approximate the ratio of the loop responses at these nearby frequencies (the last two terms in the equation) with the ratio of the reference-time responses.

The parameter $\kappa_{\mathrm{PU}}(t)$ is monitored to ensure the stability of the combined response of the upper-intermediate and penultimate mass stage actuators. Its value is calculated from the response of the x_{ctrl} line in the d_{derr} signal and incorporating an updated response of the A_{T}, i.e. using the value of $\kappa_{\mathrm{T}}(t)$ from Equation (3.6). Thus,

$$\kappa_{\mathrm{PU}}(t) = \frac{1}{A_{\mathrm{P},0}(f_{\mathrm{ctrl}}) + A_{\mathrm{U},0}(f_{\mathrm{ctrl}})} \Big(A(f_{\mathrm{ctrl}}, t) - \kappa_{\mathrm{T}}(t) A_{\mathrm{T},0}(f_{\mathrm{ctrl}}) \Big) \tag{3.7}$$

where the overall actuation at the x_{ctr} line frequency is estimated as

$$A(f_{\mathrm{ctrl}}, t') = -\frac{d_{\mathrm{err},t}(f_{\mathrm{ctrl}})}{x_{\mathrm{ctrl},t}(f_{\mathrm{ctrl}})} \left(\frac{d_{\mathrm{err},t}(f_{\mathrm{pcal1}})}{x_{\mathrm{pcal},t}(f_{\mathrm{pcal1}})} \right)^{-1} \frac{C_0(f_{\mathrm{pcal1}})}{1 + G_0(f_{\mathrm{pcal1}})} \left(\frac{C_0(f_{\mathrm{ctrl}})}{1 + G_0(f_{\mathrm{ctrl}})} \right)^{-1} \Bigg|_{t=t'} \tag{3.8}$$

The complex, time-dependent part of the sensing function can be calculated at the photon calibrator line frequency using its response function (Equation (3.3)) and the sensing function

model (Equation (3.1)):

$$S(f_{\mathrm{pcal2}}, t') = \frac{1}{Q(f_{\mathrm{pcal2}})} \left(\frac{x_{\mathrm{pcal},t}(f_{\mathrm{pcal2}})}{d_{\mathrm{err},t}(f_{\mathrm{pcal2}})} - D(f_{\mathrm{pcal2}}) A(f_{\mathrm{pcal2}}, t) \right)^{-1} \Bigg|_{t=t'} \tag{3.9}$$

where $A(f_{\mathrm{pcal2}}, t)$ is the full DARM actuation function corrected with $\kappa_{\mathrm{T}}(t)$ and $\kappa_{\mathrm{PU}}(t)$. Then $\kappa_{\mathrm{C}}(t)$ and $f_{\mathrm{C}}(t)$ can be written in terms of $S(f_{\mathrm{pcal2}}, t)$ as

$$\kappa_{\mathrm{C}}(t) = \frac{|S(f_{\mathrm{pcal2}}, t)|^2}{\Re[S(f_{\mathrm{pcal2}}, t)]}, \tag{3.10}$$

$$f_{\mathrm{C}}(t) = -\frac{\Re[S(f_{\mathrm{pcal2}}, t)]}{\Im[S(f_{\mathrm{pcal2}}, t)]} f_{\mathrm{pcal2}}. \tag{3.11}$$

Finally, the time-dependent parameter values and the time-domain models of the sensing and actuation functions can be used to reconstruct $\Delta L_{\mathrm{ext}}(t)$ from the DARM error signal as follows:

$$\begin{aligned} \Delta L_{\mathrm{ext}}(t) =& (\mathcal{P}_i(t)/\kappa_{\mathrm{C}}(t)) * \big(\mathcal{Q}_i * d_{\mathrm{err}}(t)\big) \\ &+ \Big(\kappa_{\mathrm{PU}}(t)\big(\mathcal{A}_{\mathrm{P},0} + \mathcal{A}_{\mathrm{U},0}\big) + \kappa_{\mathrm{T}}(t)\mathcal{A}_{\mathrm{T},0}\Big) * \big(\mathcal{D} * d_{\mathrm{err}}(t)\big), \end{aligned} \tag{3.12}$$

where $\mathcal{P}_i(t)$ and $\mathcal{Q}_i$ are the time-domain filters created from inverses of the coupled cavity response, $1 + if/f_{\mathrm{C}}(t)$, and the time-independent part of the sensing function, $1/Q(f)$. $\mathcal{D}$, $\mathcal{A}_{\mathrm{P},0}$, $\mathcal{A}_{\mathrm{U},0}$ and $\mathcal{A}_{\mathrm{T},0}$ are time-domain filters created from a model of the digital filters and reference-time models of the actuation functions, and $*$ denotes convolution.

Note that $\mathcal{P}_i(t)$ is a function of time. Therefore, generating the $\Delta L_{\mathrm{ext}}(t)$ time-series, in which changes in all four time-dependent parameters are compensated, requires continuously updating the $\mathcal{P}_i(t)$ time-domain filter. Compensating for changes only in scalar factors κ_{C}, κ_{PU} and κ_{T} can be accomplished using the $\mathcal{P}_i(t)$ filter created from the coupled-cavity response at the reference-time (at $t = t_0$).

3.3 Implementation of the method

This section describes the implementation of the method for tracking temporal variations. These include considerations that went into choosing proper excitation frequencies for the method, aspects of implementing the excitations and computations in the control system of the aLIGO detectors, and changes made to the software that produces the calibrated strain signal.

3.3.1 Frequencies and magnitudes of periodic excitations

As it was noted in the description of the method, tracking of the time-dependent parameters requires injecting periodic excitations (calibration lines) into various points of the DARM loop. Table 3.1 lists the frequencies of the calibration lines used for tracking temporal variations in the Advanced LIGO detectors. The choice of calibration line frequencies is governed by the parameters of the loop components into which the excitations are added as well as by the complete closed-loop response.

Table 3.1: Frequencies of calibration lines for the LIGO Hanford (H1) and LIGO Livingston (L1) detectors used for tracking temporal variations in the response of the DARM control loop during the O1 run. Lines 1-3 are used for estimation of $\kappa_{\rm T}$ and $\kappa_{\rm PU}$, and line 4 for $\kappa_{\rm C}$ and $f_{\rm C}$. From [69].[7]

#	Inj. point	Variable	Freq. (Hz)		Line Purpose
			H1	L1	
1	$x_{\rm T}$	$f_{\rm T}$	35.9	35.3	Strength of the test mass stage actuation, Equation (3.6).
2	$x_{\rm pcal}$	$f_{\rm pcal1}$	36.7	34.7	DARM actuation, Equations (3.6), (3.7).
3	$x_{\rm ctrl}$	$f_{\rm ctrl}$	37.3	33.7	Strength of the combined penultimate and upper intermediate actuation, Equation (3.7).
4	$x_{\rm pcal}$	$f_{\rm pcal2}$	331.9	331.3	Sensing scale factor and coupled-cavity pole frequency, Equations (3.10), (3.11).

For instance, calibration lines injected at points $x_{\rm pcal}$, $x_{\rm T}$ and $x_{\rm ctrl}$ are used to estimate temporal variations in the actuation. The $\kappa_{\rm T}$ factor in particular is estimated from responses to the $x_{\rm pcal1}$ and

x_{T} calibration lines. These two lines must be placed at nearby frequencies to reduce systematic errors associated with the changes in the shape of the overall response function of the detector. Similarly, to reduce errors in the estimation of $A(f_{\mathrm{ctrl}}, t)$, which is an intermediate quantity used for calculation of κ_{PU}, the lines injected into x_{ctrl} and x_{pcal1} also must be placed at nearby frequencies. These two conditions dictate that all three calibration lines (x_{pcal1}, x_{T} and x_{ctrl}) must be placed in a narrow frequency band.

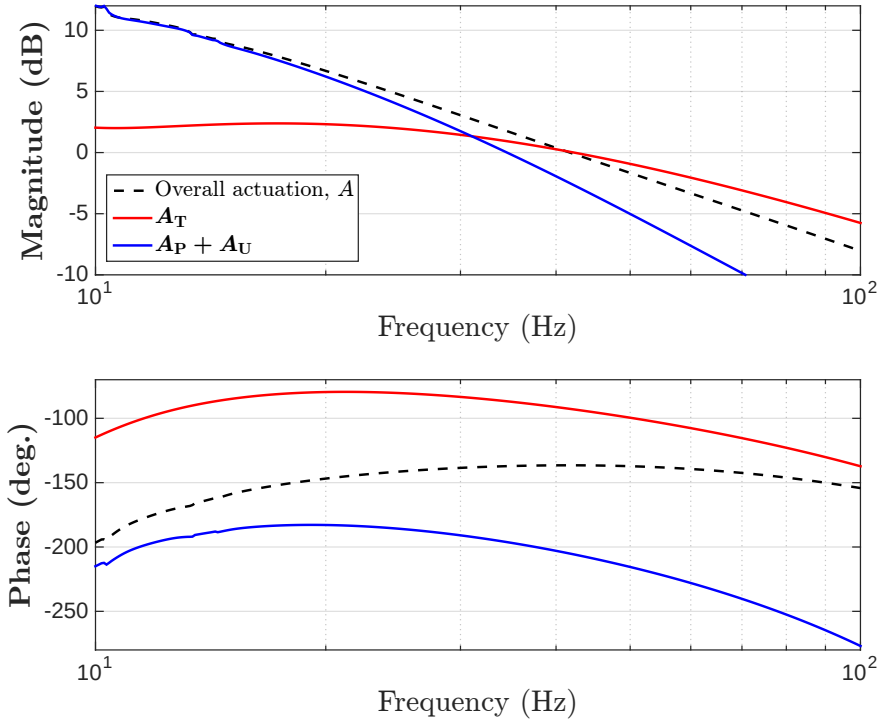

Figure 3.6: Bode plot of the DARM loop actuation functions for the test mass stage and the combined penultimate mass and the upper-intermediate stages, *i.e.* A_{T} and $A_{\mathrm{P}} + A_{\mathrm{U}}$, zoomed at the frequency band $[10, 100]$ Hz. Actuation response magnitudes of the test mass stage and the combined "P" and "U" stages cross at approximately 35 Hz. Calibration line frequencies for tracking temporal variations in the actuator responses were selected close to this frequency.

As explained in Section 3.2.1 the actuation transfer function consists of three terms that represent the actuators of the three stages of the suspension system. From the individual transfer functions of the three stages it can be seen that above the quadruple pendulum resonance frequencies the responses are roughly proportional to $1/f^6$, $1/f^4$ and $1/f^2$. At the frequency where the responses of the test mass stage and the combined penultimate mass and the upper-intermediate

mass stages overlap, *i.e.* the crossover frequency, the sensitivity of the DARM error signal to variations in these stages is roughly the same. During the engineering runs preceding aLIGO's first observation period, measurements of the actuation functions indicated that the crossover frequency was near $35\ \mathrm{Hz}$ (see Figure 3.6). For this reason the frequency band for the three calibration lines used for tracking temporal variations in the actuation functions is near this value.

Temporal variations in the sensing function are tracked with a single calibration line injected via Pcal, x_{pcal2}. In order to maximize the sensitivity of the DARM response to the variations of κ_{C} and f_{C} we need to look at frequencies where $S(f,t)$, the time-dependent part of the sensing function, varies the most as a function of these parameters, *i.e.* where $\partial S/\partial\kappa_{\mathrm{C}}$ and $\partial S/\partial f_{\mathrm{C}}$ normalized to $|S(f,t)|$ are maximized. Given that the derivative $\partial S/\partial\kappa_{\mathrm{C}}$ is not frequency dependent, the choice of the calibration line frequency is determined from $\partial S/\partial\kappa_{\mathrm{C}}$, which is greatest at the coupled cavity (CC) pole frequency. Therefore the line frequency for tracking temporal variations in the sensing functions was chosen to be near the nominal CC pole frequency, $341\ \mathrm{Hz}$ at LIGO Hanford and $388\ \mathrm{Hz}$ at LIGO Livingston [75].[8]

Another important consideration in choosing calibration line frequencies is that LIGO data is also used for long-term searches for pulsar signals. As a result, the calibration line frequencies were selected to be at least $0.1\ \mathrm{Hz}$ apart from the frequencies of known pulsars.

Magnitudes of the excitations were set at levels which provide measurements with a signal-to-noise ratio (SNR) of 100 in the frequency domain with $10\,\mathrm{s}$ integration times, i.e. the magnitudes of excitations in the amplitude spectral density plot of the DARM error signal are two orders of magnitude larger than the background noise levels.

Secondary Pcals (see Section 4.2) are also used to inject additional calibration lines at frequencies above $1\,\mathrm{kHz}$ with comparably smaller SNRs. These lines are used for verification of the calibration accuracy at high-frequencies.

[8]The line frequencies for both sites were chosen based on the LIGO Hanford CC pole frequency, $341\ \mathrm{Hz}$, since this was a known value at the moment.

3.3.2 aLIGO controls infrastructure updates

During operation, an aLIGO detector is maintained in the nominal state by a set of control loops. All of the control signals in the detector are realized via a dedicated software and hardware infrastructure called the LIGO Control and Data System (CDS). Processors that interact with and control servo loops are called the *front-end processors* and software modules running on them are called *front-end models*. Implementation of the method for tracking temporal variations in the DARM loop required modifications of the front-end infrastructure of the DARM loop. These included: *a)* addition of stored data channels needed for further analysis, *b)* insertion of synchronized oscillators that generate periodic signals that are injected into the DARM loop at designated locations, and *c)* a module that calculates the time-dependent parameters and outputs them to data channels. Implementation of these modifications is done through editing of the front-end models with the MATLAB Simulink® model editor and re-compiling of the front-end modules (see Figure 3.7). Details of these modifications are reported in the LIGO lab logbooks [76, 77].

The synchronized oscillators added to the front-end blocks are used for injection of calibration lines at points that correspond to $x_{\rm ctrl}$, $x_{\rm T}$ and $x_{\rm pcal}$ (see Figure 3.5). The reason they are called "synchronized" is that regardless of the launching time, the phases of these oscillators are always tied to GPS time (thus, in the CDS system they are called 'fixed-phase oscillator' parts).

Calculation of the time-dependent parameter values in CDS requires implementation of the tracking calculations in the front-end models. The calculations use reference-time sensing and actuation model TFs. A convenient way of storing these values and feeding them to the front end calculations is via the Experimental Physics and Industrial Control System (EPICS), a low-bandwidth CDS operator interface. The updates made to the aLIGO controls include the addition of dedicated EPICS records used for calculation of the time-dependent parameters in the front end models.

The equations for calculating the time-dependent parameters are modified by combining the reference-time factors in them into complex numbers. These values are then precalculated from the reference-time models and stored in corresponding EPICS records. For the purposes of read-

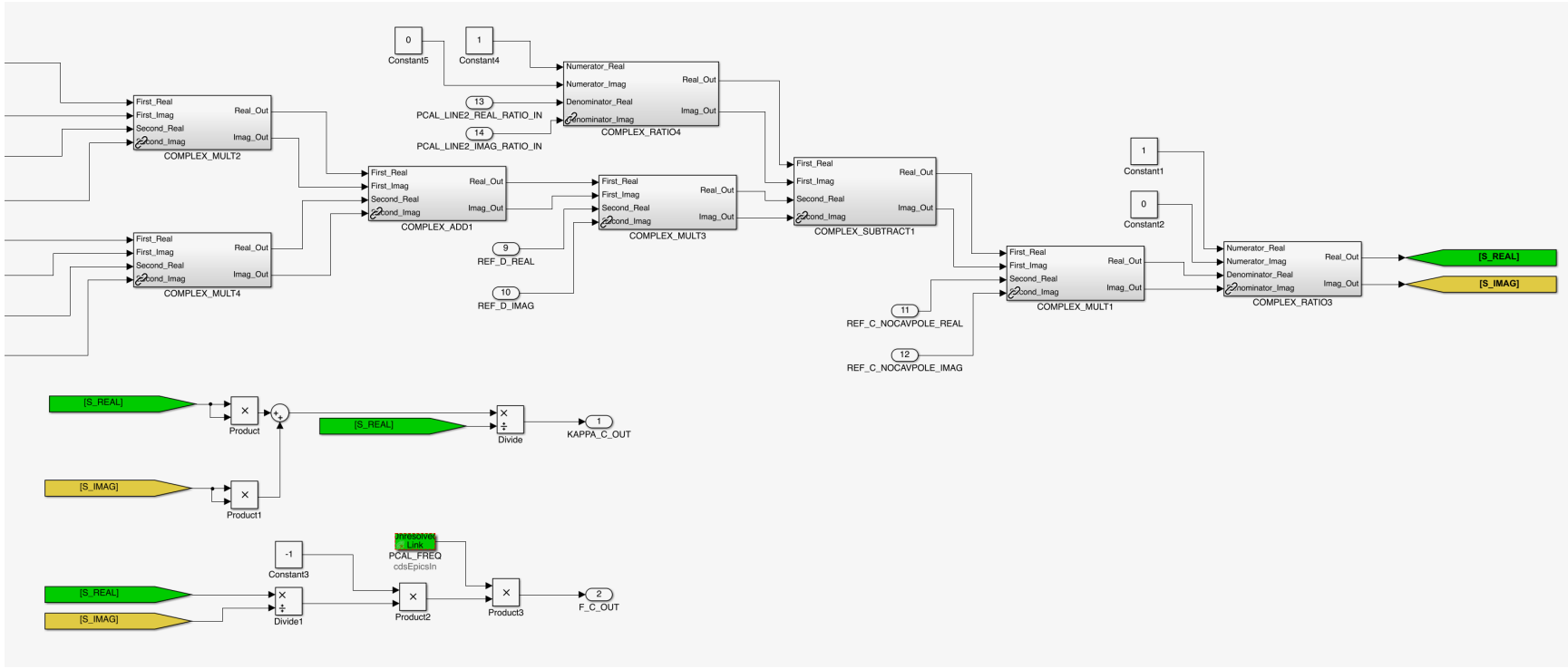

Figure 3.7: Sample of the calibration front-end model in the CDS system. This diagram shows the part of the model in which the complex time-dependent factor of the sensing function at the Photon Calibrator line frequency ($\sim 340\,\mathrm{Hz}$) is calculated. In other words, it implements the calculation of $S(f_{\mathrm{pcal2}}, t)$ given in Equation (3.20). For detailed implementation reports see [76, 77].

ability of the equations below, instead of writing rather long names of the EPICS variables, they are represented by short identifiers EPn. Corresponding full EPICS record names are listed in Table 3.2. Their real and imaginary components, represented with _R and _I in the table, have also been omitted in the equations.

Table 3.2: Definition of constants for EPICS records used in the aLIGO controls infrastructure (equations in Section 3.3.2). Each of the complex-valued constants, EPn, in the EPICS database are represented with their real and imaginary values, EPn_R and EPn_I. The prefix '${ifo}' in an EPICS record name is set to 'H1' for LIGO Hanford and 'L1' for LIGO Livingston [76, 78].

Const.	EPICS record name
EP1_R	${ifo}:CAL-TDEP_REF_INVA_CLGRATIO_TST_REAL
EP1_I	${ifo}:CAL-TDEP_REF_INVA_CLGRATIO_TST_IMAG
EP2_R	${ifo}:CAL-CS_TDEP_REF_CLGRATIO_CTRL_REAL
EP2_I	${ifo}:CAL-CS_TDEP_REF_CLGRATIO_CTRL_IMAG
EP3_R	${ifo}:CAL-CS_TDEP_DARM_LINE1_REF_A_USUM_INV_REAL
EP3_I	${ifo}:CAL-CS_TDEP_DARM_LINE1_REF_A_USUM_INV_IMAG
EP4_R	${ifo}:CAL-CS_TDEP_DARM_LINE1_REF_A_TST_REAL
EP4_I	${ifo}:CAL-CS_TDEP_DARM_LINE1_REF_A_TST_IMAG
EP5_R	${ifo}:CAL-CS_TDEP_DARM_LINE1_REF_A_USUM_REAL
EP5_I	${ifo}:CAL-CS_TDEP_DARM_LINE1_REF_A_USUM_IMAG
EP6_R	${ifo}:CAL-CS_TDEP_PCALY_LINE2_REF_C_NOCAVPOLE_REAL
EP6_I	${ifo}:CAL-CS_TDEP_PCALY_LINE2_REF_C_NOCAVPOLE_IMAG
EP7_R	${ifo}:CAL-CS_TDEP_PCALY_LINE2_REF_D_REAL
EP7_I	${ifo}:CAL-CS_TDEP_PCALY_LINE2_REF_D_IMAG
EP8_R	${ifo}:CAL-CS_TDEP_PCALY_LINE2_REF_A_TST_REAL
EP8_I	${ifo}:CAL-CS_TDEP_PCALY_LINE2_REF_A_TST_IMAG
EP9_R	${ifo}:CAL-CS_TDEP_PCALY_LINE2_REF_A_USUM_REAL
EP9_I	${ifo}:CAL-CS_TDEP_PCALY_LINE2_REF_A_USUM_IMAG

For $\kappa_{\mathrm{T}}(t)$ Equation (3.6) was rewritten as

$$\kappa_{\mathrm{T}}(t') = \frac{d_{\mathrm{err},t}(f_{\mathrm{T}})}{x_{\mathrm{T},t}(f_{\mathrm{T}})} \left(\frac{d_{\mathrm{err},t}(f_{\mathrm{pcal1}})}{x_{\mathrm{pcal},t}(f_{\mathrm{pcal1}})} \right)^{-1} \times \mathtt{EP1} \Bigg|_{t=t'} \tag{3.13}$$

where

$$\mathtt{EP1} = \frac{1}{A_0^{\mathrm{T}}(f_{\mathrm{T}})} \cdot \frac{C_0(f_{\mathrm{pcal1}})}{1 + G_0(f_{pcal1})} \left(\frac{C_0(f_{\mathrm{T}})}{1 + G_0(f_{\mathrm{T}})} \right)^{-1} \tag{3.14}$$

A temporary value that represents the total actuation function at f_{ctrl} (Equation (3.8)) is calculated as

$$A(f_{\mathrm{ctrl}}, t') = -\frac{d_{\mathrm{err},t}(f_{\mathrm{ctrl}})}{x_{\mathrm{ctrl},t}(f_{\mathrm{ctrl}})} \left(\frac{d_{\mathrm{err},t}(f_{\mathrm{pcal1}})}{x_{\mathrm{pcal},t}(f_{\mathrm{pcal1}})} \right)^{-1} \times \mathtt{EP2} \Bigg|_{t=t'} \tag{3.15}$$

where

$$\mathtt{EP2} = \frac{C_0(f_{\mathrm{pcal1}})}{1 + G_0(f_{\mathrm{pcal1}})} \left(\frac{C_0(f_{\mathrm{ctrl}})}{1 + G_0(f_{\mathrm{ctrl}})} \right)^{-1}. \tag{3.16}$$

Then, the equation for $\kappa_{\mathrm{PU}}(t)$ is written as

$$\kappa_{\mathrm{PU}}(t') = \mathtt{EP3} \times \left[A(f_{\mathrm{ctrl}}, t) - \kappa_{\mathrm{T}}(t) \cdot \mathtt{EP4} \right] |_{t=t'} \tag{3.17}$$

where

$$\mathtt{EP3} = \frac{1}{A_0^{\mathrm{PU}}(f_{\mathrm{ctrl}})} \tag{3.18}$$

and

$$\mathtt{EP4} = A_0^{\mathrm{T}}(f_{\mathrm{ctrl}}) \tag{3.19}$$

Calculation of the time-dependent parameters of the sensing function, $\kappa_{\mathrm{C}}(t)$ and $f_{\mathrm{C}}(t)$ is accomplished by calculating the time-dependent factor containing them, $S(f_{\mathrm{pcal2}}, t)$, as follows

$$S(f_{\mathrm{pcal2}}, t') = \frac{1}{\mathtt{EP6}} \left(\frac{x_{\mathrm{pcal},t}(f_{\mathrm{pcal2}})}{d_{\mathrm{err},t}(f_{\mathrm{pcal2}})} - \mathtt{EP7} \left[\kappa_{\mathrm{T}}(t) \cdot \mathtt{EP8} + \kappa_{\mathrm{PU}}(t) \cdot \mathtt{EP9} \right] \right)^{-1} \Bigg|_{t=t'} \tag{3.20}$$

where

$$\texttt{EP6} = C_{\rm res}(f_{\rm pcal2}), \tag{3.21}$$

$$\texttt{EP7} = D_0(f_{\rm pcal2}), \tag{3.22}$$

$$\texttt{EP8} = A_0^{\rm T}(f_{\rm pcal2}), \tag{3.23}$$

$$\texttt{EP9} = A_0^{\rm PU}(f_{\rm pcal2}). \tag{3.24}$$

The equations for $\kappa_{\rm C}(t)$ and $f_{\rm C}(t)$ are the same as those given in the description of the method, Equations (3.10) and (3.11).

Note that for clarity of the discussion, some of the details such as the need to use dewhitening filters when analyzing calibrated Pcal channels and the need to incorporate digital and analog anti-aliasing filters [79], have been omitted from the equations in this section.

3.3.3 Computation of the calibrated strain signal

A code that computes the calibrated GW strain time-series, $h(t)$, runs within a software pipeline called the Data Monitoring Tool (DMT) on computer clusters located at both LIGO sites. It produces the strain time series from the LIGO CDS data streams with minimal delay and is commonly referred to as the *low-latency pipeline*. A detailed description of this software is given in [80].

The final step of the method, application of corrections for temporal variations in the DARM loop, is implemented in this pipeline. For its inputs the pipeline takes timestamped Pcal and DARM signals stored in the so-called *science frames*. The EPICS values (see Section 3.3.2) and the $x_{\rm pcal}$, $d_{\rm err}$ and $d_{\rm ctrl}$ time-series from the frames are used to calculate the $\kappa_{\rm T}(t)$, $\kappa_{\rm PU}(t)$, $\kappa_{\rm C}(t)$ and $f_{\rm C}(t)$ parameters. To reduce noise, these values are averaged over 128 seconds. If the calculated parameter values are within accepted thresholds, they are marked as "good" values (i.e. *good kappas*) and are used in calculation of $h(t)$, thus producing a time series corrected for temporal variations in the DARM response. On the other hand, the values that fall outside of their respective thresholds are marked as "bad" and the strain is calculated with the most recent "good" values of the

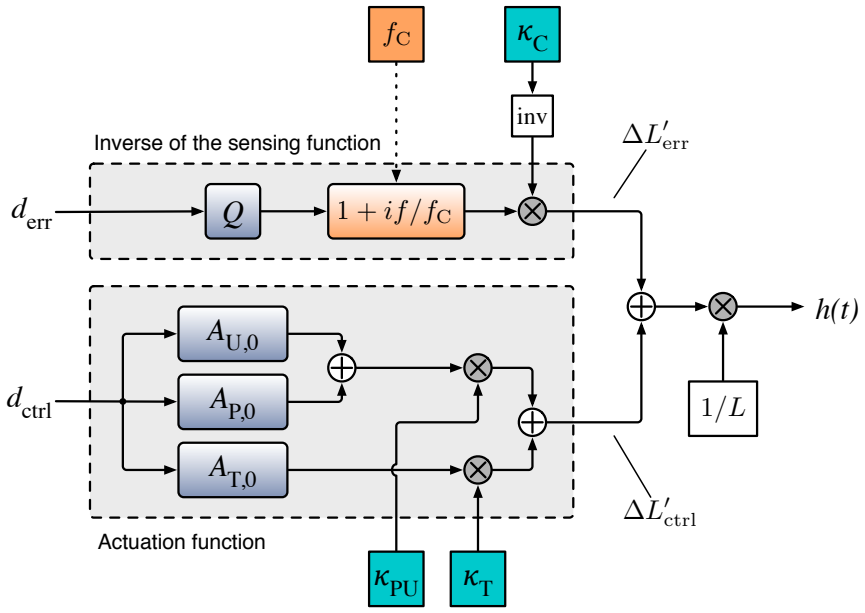

Figure 3.8: A simplified diagram of the low-latency calibration pipeline, a software pipeline that computes the strain signal. Both the inverse of the sensing function and three of the quadruple pendulum actuation functions in the pipeline are represented by finite impulse response (FIR) filters. The Q FIR filter represents the time-independent part of the sensing function. The inverse of the coupled cavity response is represented as a separate FIR filter denoted by $1 + if/f_C$. This FIR filter, for full correction of the temporal variations in the coupled cavity response, must evolve dynamically to accurately represent variations in f_C. During the O1 and O2 runs the inverse of the sensing function was represented with constant FIR filters (based on the reference-time coupled cavity pole frequency). The diagram does not show the calculation of averaged "kappa" values and conditional inclusion or exclusion of the corrections based on "goodness" of the "kappas."

parameters. The low-latency pipeline stores the computed $h(t)$ time-series and a status vector which contains, among other flags, the goodness of the time-dependent parameters, in the science frames. A simplified diagram of this process is outlined in Figure 3.8 (for a more detailed diagram see [60]).

Note that compensating for variations in the CC pole frequency requires actively updating the finite impulse response (FIR) filter that represents the inverse of the CC response. Ways of implementing this feature are being investigated. Thus, during the O1 and O2 runs the inverse of the sensing function (blocks "Q" and "$1 + if/f_C$" in the diagram) was represented by a constant FIR filter that was generated based on the reference-time sensing model.

To summarize, the modifications made in the low-latency pipeline include calculation of the

time-dependent parameters (raw and averaged values), generation of status information on "goodness" of the calculated parameter values, and application of the averaged values in the computations of the GW strain time-series.

3.4 Results and discussions

The method described in this chapter was used for compensating for slow temporal variations in the Advanced LIGO calibration during its first and second observing runs (the O1and O2runs). Implementation of the method proceeded in several iterations. Results from preliminary tests as well as from the O1 run are presented below. Implications of the corrections for temporal variations in the DARM control loop are further discussed in Chapter 5.

3.4.1 Preliminary tests of tracking the time-varying parameters (ER7)

The initial assessment of tracking temporal variations in the coupled-cavity (CC) pole response was made during the seventh engineering run (ER7). This concept was tested by monitoring variations in the responses of a calibration lines at about $35\,\mathrm{Hz}$ and $500\,\mathrm{Hz}$ that were injected with both of the Pcal systems, the X-end and Y-end Pcals.

The results of these tests were reported in [81]. During this period the model used for analyzing the responses included two time-dependent parameters: variations in the optical gain and the coupled-cavity pole frequency.

From this test it was concluded that temporal variation captured from two different Pcal systems are consistent with each other. Analysis of the calibration line responses showed that variations in the optical gain can be assessed from any of the four calibration lines. Contrary to that, variations in the CC pole frequency are more clearly seen from lines at higher frequencies (see Figure 3.9). This is an expected outcome, because changes in the optical gain scale the sensing function equally at all frequencies, while changes in the coupled-cavity response are greatest in the band near the pole frequency. In retrospect, the choice of the calibration line frequency for tracking the sensing parameters in O1, as was noted in Section 3.3, was chosen near the nominal CC pole frequency.

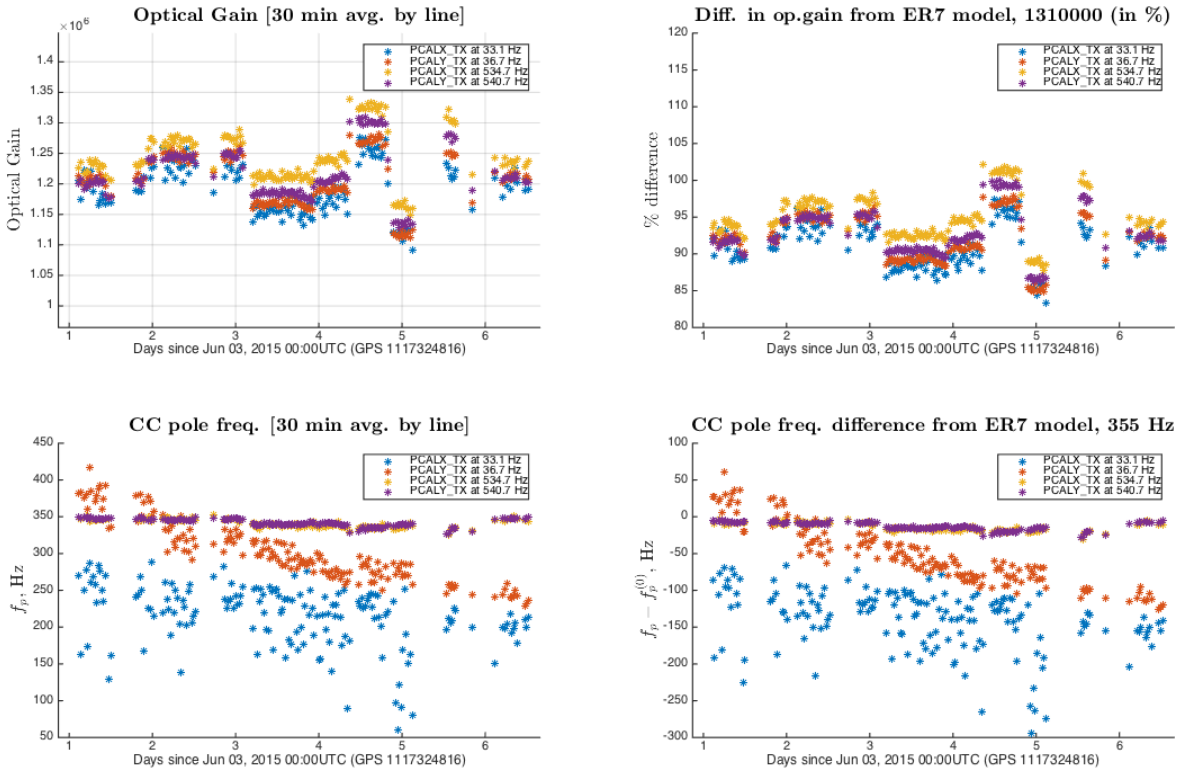

Figure 3.9: Optical gain and coupled cavity pole frequency measurements during the ER7 run (LIGO Hanford). Both of the parameters are estimated independently using calibration lines injected with both the X- and Y-end Pcals at $33.1\,\mathrm{Hz}$, $36.7\,\mathrm{Hz}$, $534.7\,\mathrm{hz}$ and $540.7\,\mathrm{hz}$. The observed trend in the optical gain is seen with all four calibration lines and the coupled cavity pole frequency trends are consistent for lines near $\sim 500\,\mathrm{Hz}$. From [81].

Results from other tests during ER7, in which calibration line amplitudes were increased, helped to determine calibration line drive levels that are needed to reduce parameter uncertainties to the desired levels [82].

An analysis of 30-minute averaged values from the $\sim 500\,\mathrm{Hz}$ lines during the ER7 run (see Figure 3.10) showed that the optical gain varied up to $11\,\%$ from the reference-time value and the coupled-cavity pole frequency varied between 335 and $350\,\mathrm{Hz}$. Observed discrepancies between parameter values estimated using different calibration lines are the result of model imperfections, such as previously unknown time-delay of $125\,\mu\mathrm{s}$ between the signals. This was mostly resolved before ER8.

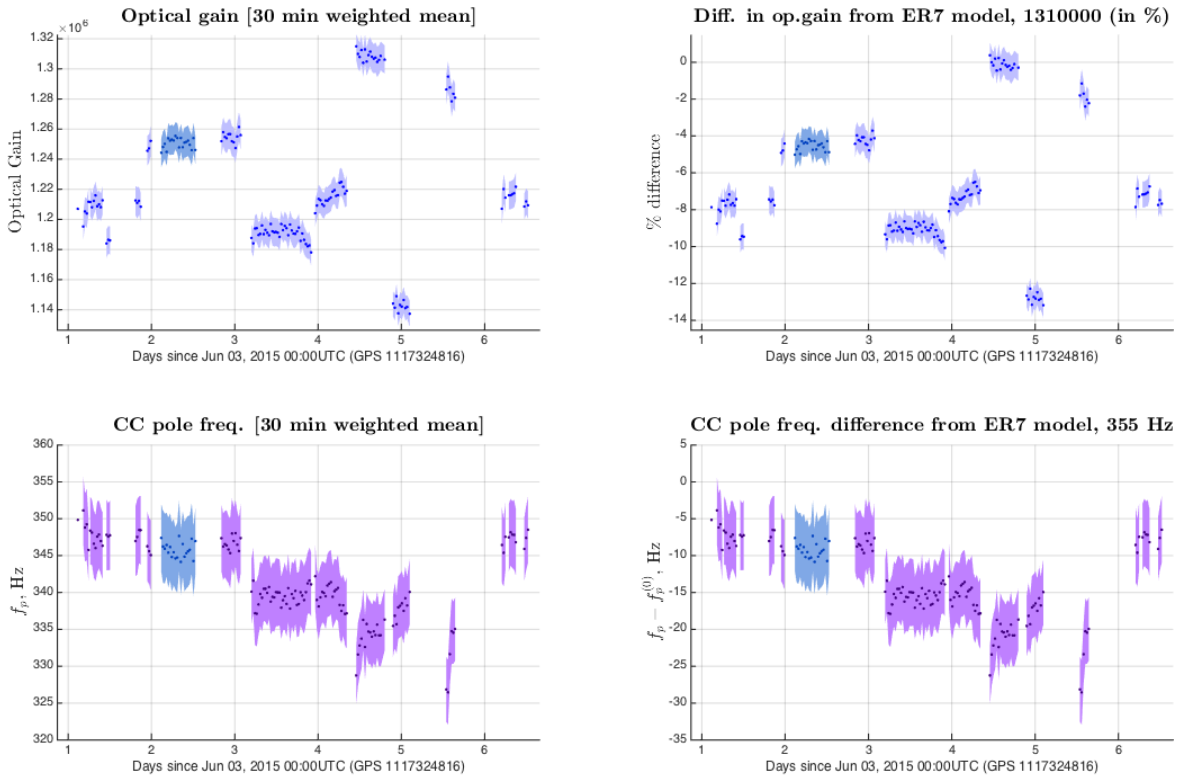

Figure 3.10: Averaged values of the optical gain and coupled cavity pole frequency during the ER7 run (LIGO Hanford). Data points are 30-minute averages estimated from the two high-frequency calibration lines ($534.7\,\mathrm{Hz}$ and $540.7\,\mathrm{Hz}$). Variations in the optical gain are about $11\,\%$. The CC pole frequency varied between 335 and $350\,\mathrm{Hz}$. From [81].

3.4.2 Parameter values during the first observing run (O1)

Trends of the time-dependent parameter values obtained from calibration lines during the O1 run are presented in Figure 3.11. As was discussed in Section 3.2.2, not compensating for temporal variations in the DARM control loop will result in a time-dependent increase of systematic errors in the calibration of the detectors.

At both observatories, κ_T exhibited a steady drift, which indicates a reduction in the response of the test mass stage actuators. These are electrostatic force actuators (see Section 2.3.2); the drifts in the responses of these actuators are attributed to charge accumulation on the surface of the ETMs. The rapid change in the κ_T trend for LIGO Hanford seen in Figure 3.11 was caused by a scheduled flip in the voltage bias sign [83], which reverses the effect of the charge accumulation. By inverting

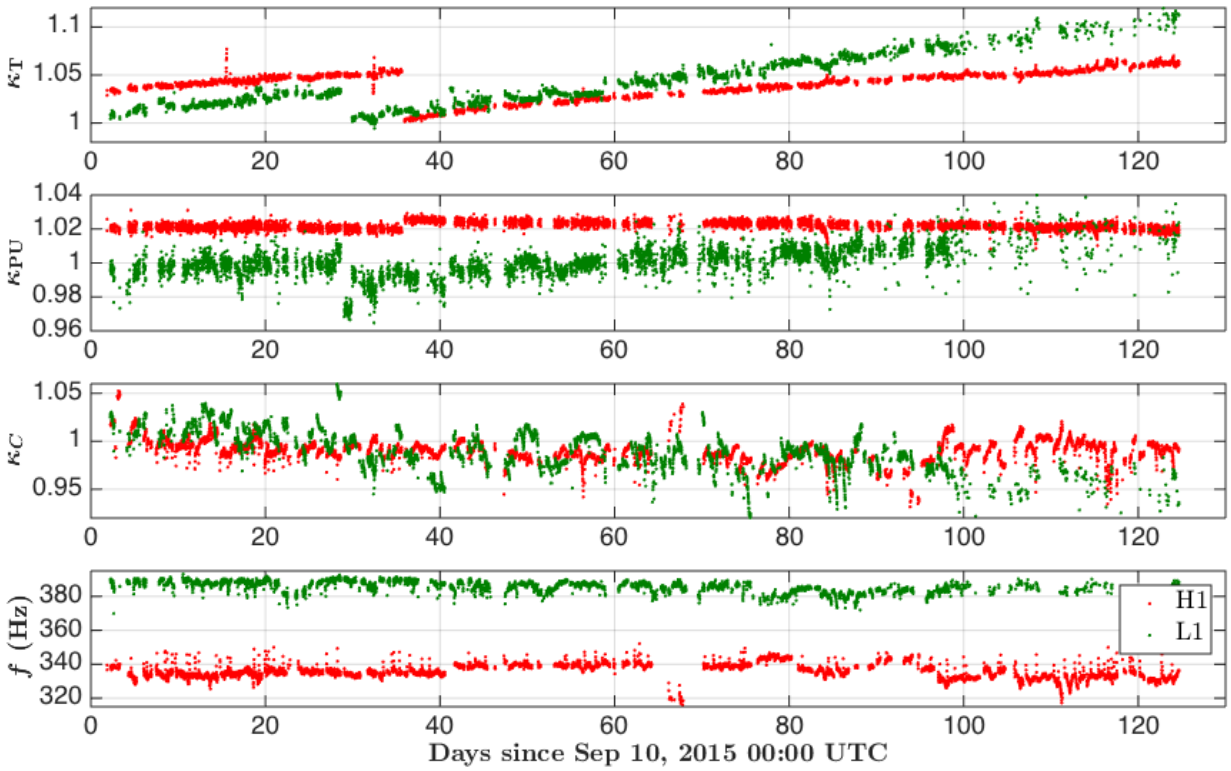

Figure 3.11: DARM time-dependent parameters calculated from calibration lines at LIGO Hanford (*red traces*) and LIGO Livingston (*green traces*). Nominal values of all three scalar factors, κ_{T}, κ_{PU} and κ_{C} are 1.0, and the nominal value of the coupled cavity pole frequency, f_{C}, for LIGO Hanford is 341 Hz and for LIGO Livingston is 388 Hz.

the d_{ctrl} to actuation sign, the sign of the overall actuation function remains unchanged [83]. One might also observe a sudden change of this parameter at LIGO Livingston (as seen in Figure 3.11, on day ~ 30), this is the result of doubling of the ESD driver bias voltage. Throughout the rest of the O1 run the test mass stage actuator configurations, i.e. the ESD bias voltage and its sign, at the LIGO Livingston detector remained unchanged. This resulted in the overall discrepancy between the reference-time actuator model and the true response to reach $\sim 10\,\%$ at the end of the run.

The combined strengths of the upper-intermediate and penultimate mass stage actuators are monitored by the κ_{PU} parameter. The LIGO Hanford κ_{PU} trend shows a sudden shift in the κ_{PU} parameter at a sub-percent level coincident with the rapid changes in κ_{T}. Due to the fact that the κ_{PU} parameter estimation is based on the calibration line injected into the overall actuation (see Section 3.2), such a change in the parameter value is expected to appear when the initial actuator

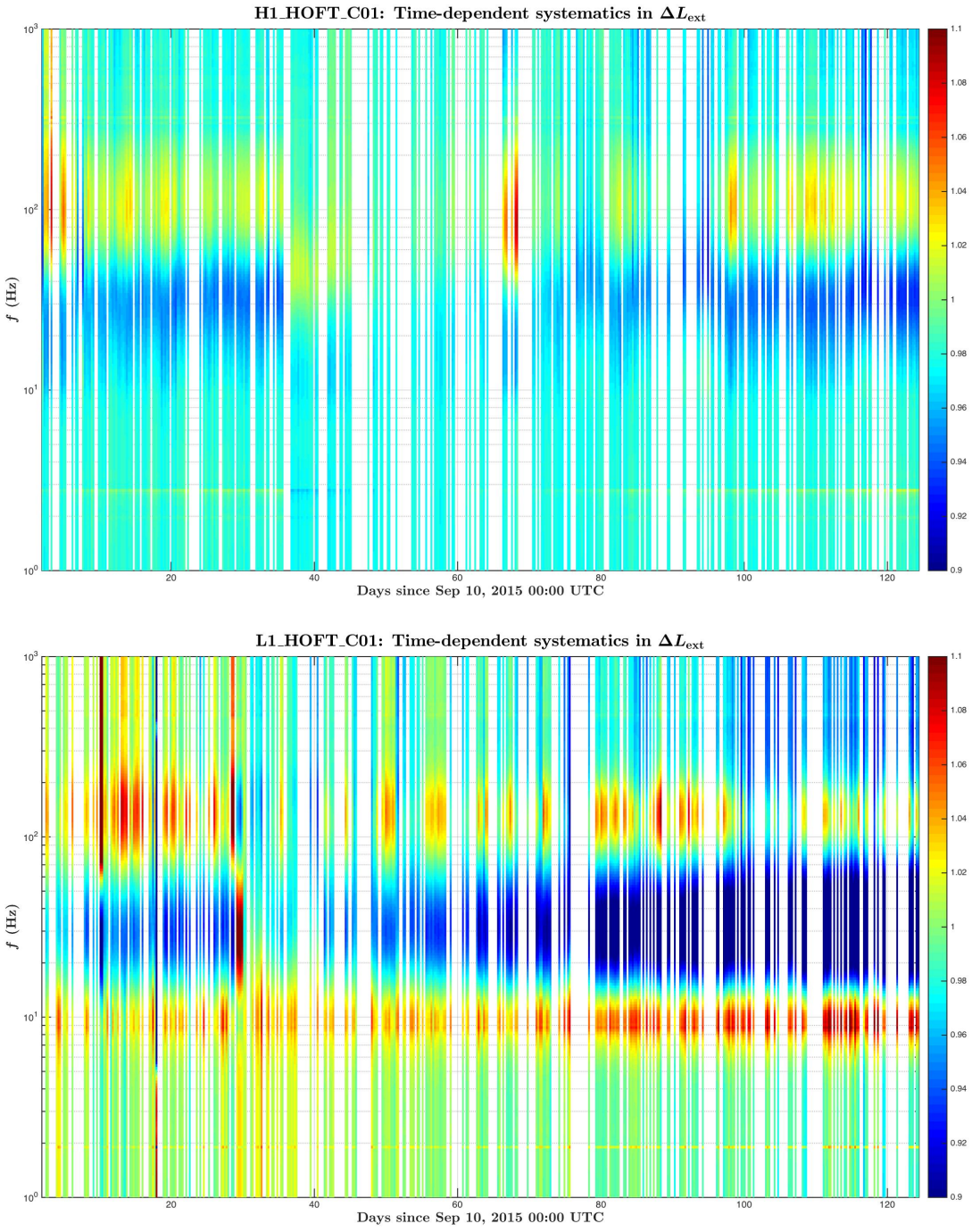

Figure 3.12: Time-dependent systematic errors in the static response function models of the LIGO Hanford (*upper panel*) and LIGO Livingston (*lower panel*) detectors, R, calculated using κ_{T}, κ_{PU}, κ_{C} and f_{C}. The time span of the spectrograms includes the entire duration of the O1 run. The color axis is the fractional systematic error.

models have small discrepancies.[9] In the O1 run, the low-frequency calibration lines at LIGO Livingston had smaller SNRs compared the lines in LIGO Hanford, as a consequence statistical errors in the estimated values of κ_{PU} at the Livingston detector are greater than those of the Hanford detector.

Changes in the sensing function happen on a more short-term basis. As shown in Figure 3.11, both the κ_{C} and f_{C} change mostly at the beginning of a lock stretch. This indicates to changes in the optical modes in the signal recycling and arm cavities due to thermal effects impacting the main interferometer beam. The drifts start when the temperature of test masses start increasing due to high beam power circulating in the interferometer cavities. The optical response of the interferometer stabilizes within $\sim 20 - 30\,\mathrm{min}$; it is believed that the mirrors at this point reach their operating temperatures.

Overall changes in the detector response caused by temporal variations, i.e. the combination of the four time-dependent parameters, are shown in Figure 3.12. These spectrograms show potential increases in the systematic errors in the calibrated differential arm length displacements of LIGO detectors. As shown in Sections 3.4.3 and 3.4.4, the implemented corrections for temporal variations enabled a significant reduction of systematic errors.

3.4.3 Reduction of discrepancies in the multiple-frequency transfer function measurements

In Advanced LIGO, the responses of the sensing and actuation functions are determined from multiple-frequency sinusoidal excitation measurements. These measurements are commonly referred to as *swept-sine measurements*. Evaluation of both the sensing and overall actuation functions is accomplished using two swept-sine measurements that are taken within a short time interval: a DARM open loop response measurement and the response of DARM error to the Pcal excitations (see Chapter 2).

Periodically, on the scale of weeks, these measurements are repeated throughout an observation period to ensure the correctness of the models. Fractional systematic errors in the sensing

[9] The value of κ_{PU} at LIGO Hanford being $\sim 2\,\%$ off from the nominal value on September 10, 2015 ($\kappa_{\mathrm{PU}}(t_0) \approx 1.02$) indicates to a discrepancy between $A_{\mathrm{PU},0}$ (reference-time model) and the true responses of the actuators.

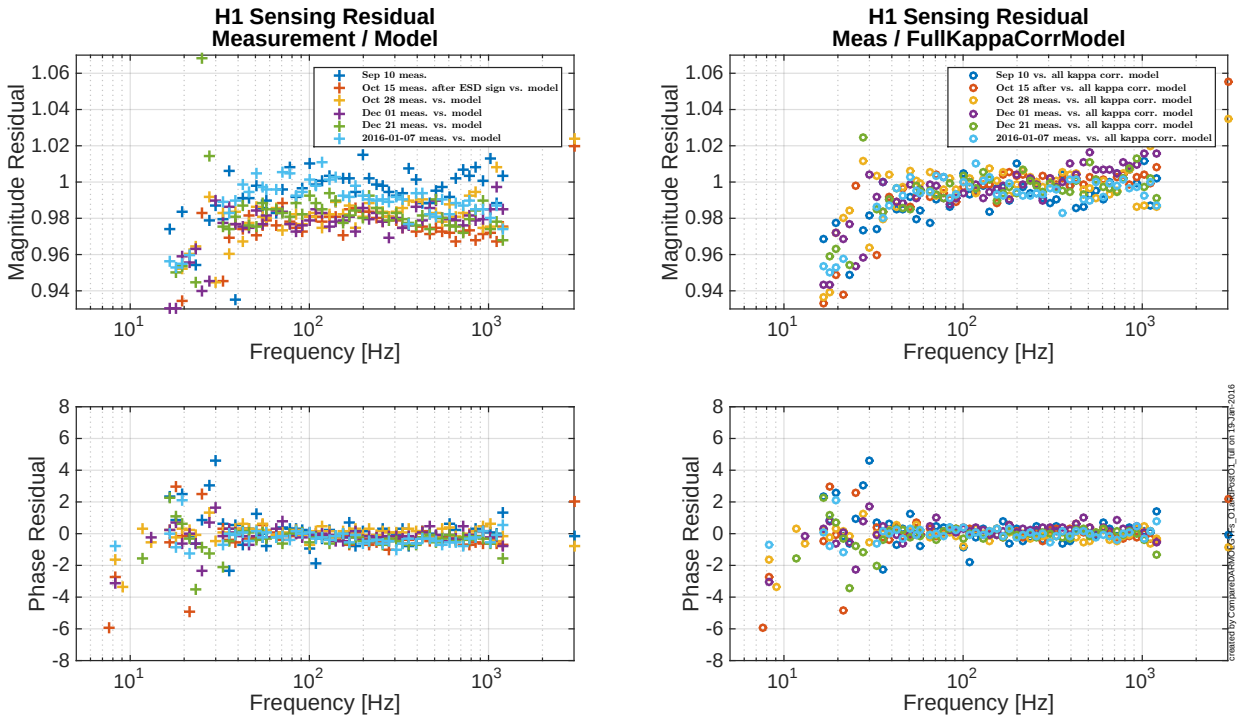

Figure 3.13: Comparison of multiple-frequency measurements of the sensing function with the reference-time model (*left panels*) and with the models that incorporate time-dependent correction factors (*right panels*). Over the course of the O1 run, as the result of time-dependent parameter corrections, the discrepancy between the measurements and the models above $\sim 40\,\mathrm{Hz}$ decrease from $\pm 3\,\%$ to approximately $\pm 1\,\%$.

and actuation models are obtained by taking ratios of these measurements with their respective models. By comparing systematic errors in subsequent measurements one can track the evolution of systematic errors.

The comparisons of the sensing function measurements (see Figure 3.13, left panels) show that, over the course of the O1 run, above $\sim 40\,\mathrm{Hz}$ the systematic errors were $\pm 3\,\%$. These errors were reduced to approximately $\pm 1\,\%$ after the temporal variations were corrected with the $\kappa_\mathrm{C}(t)$ and $f_\mathrm{C}(t)$ values (Figure 3.13, right panels). During the O1 run the signal recycling mirror detuning effect was not incorporated into the sensing model, which is a possible source of discrepancy at frequencies below $20\,\mathrm{Hz}$.

Discrepancies in the overall actuation model are shown in Figure 3.14. In this case, a more dramatic drift, from $-2\,\%$ to $+8\,\%$ in the band between 30 and $300\,\mathrm{Hz}$, in the actuation strength

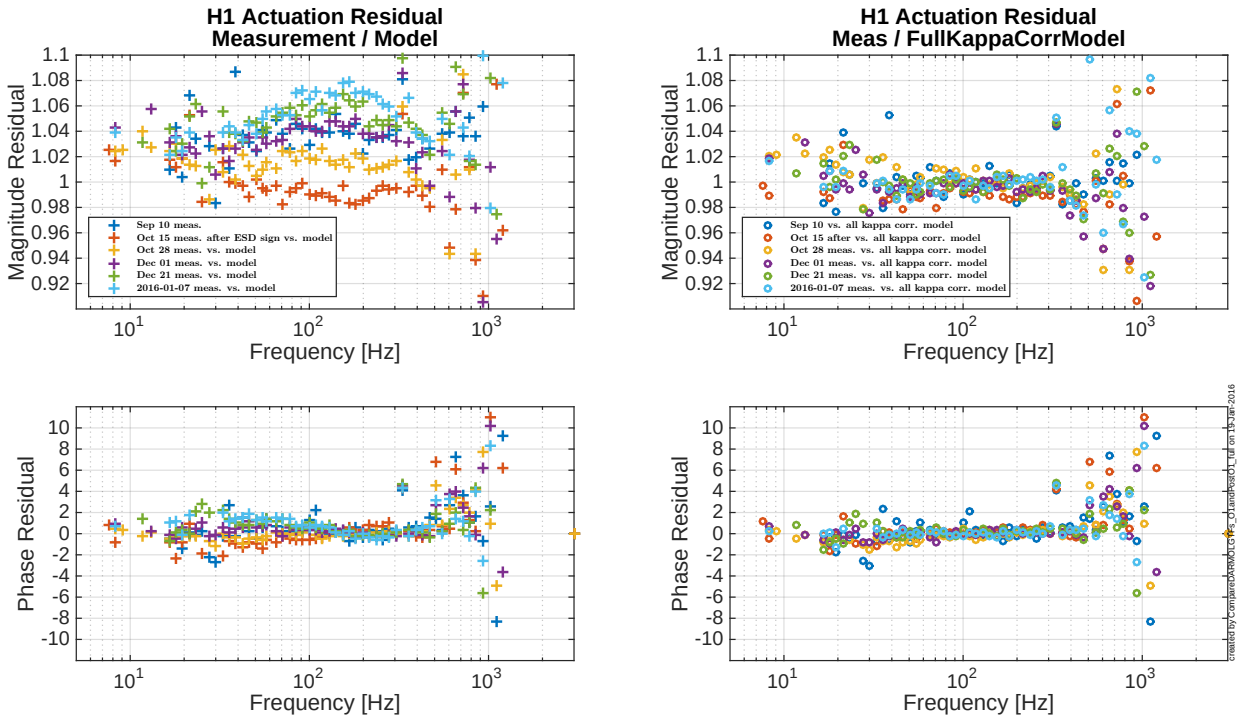

Figure 3.14: Comparison of multiple-frequency measurements of the actuation function with the reference-time model (*left panels*) and with the models that incorporate time-dependent correction factors (*right panels*).

was observed over the course of the observation period. The temporal evolution of the systematic errors in the model was also reduced to approximately $\pm 1\,\%$ in magnitude. In each case the values of the time-dependent parameters used in the models were obtained immediately before the swept-sine measurements.

3.4.4 Compensating the temporal variations in the calibrated strain signal

Variations in three of the four time-dependent parameters introduced in Section 3.2, in particular $\kappa_{\mathrm{T}}(t)$, κ_{PU} and κ_{C}, were used to compensate temporal variations in the reconstructed strain time-series according to Equation 3.12 (also see Section 3.3.3 "Computation of the calibrated strain signal"). Together with the time dependence-corrected strain, during the O1 run, the low-latency pipelines also produced the strain signal according to an old scheme in which these corrections are not applied.

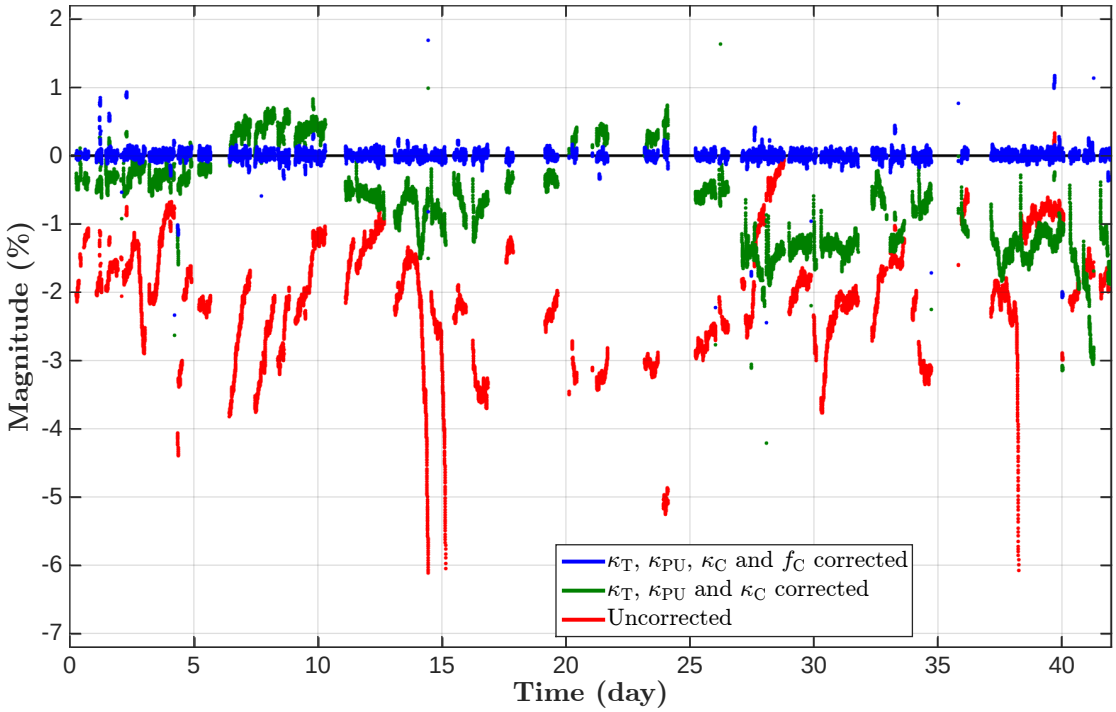

Figure 3.15: Systematic errors in the magnitude of $\Delta L_{\rm ext}$ reconstructed using static models of the sensing and actuation functions (*red*), models with the parameters corrected for time-dependences in $\kappa_{\rm PU}(t)$, $\kappa_{\rm T}(t)$ and $\kappa_{\rm C}(t)$ (*green*), and models that additionally include corrections for changes in the coupled-cavity pole frequency, $f_{\rm C}(t)$ (*blue*). The data are averaged over 30-minute intervals. From [69].[7]

A Pcal calibration line at $\sim$ 350 Hz was used to assess the agreement of the known Pcal excitations with the calibrated line amplitudes from the low-latency pipeline. Figure 3.15 shows three versions of the line amplitude compared to the displacements from Pcal over the course of 42 days during the O1 run. The comparison shows that the time-dependence-corrected time series (*green*) deviates significantly less from the expected amplitudes compared with the uncorrected time-series (*red*).

Values for the third trace which includes corrections of all four time-dependent parameters (*blue*) were calculated offline, because for the interval shown on the plot such a time-series was not produced by the low-latency pipeline. This trace was obtained by multiplying Fourier transforms of the (three-parameter) corrected strain signal (*green*) by $\dfrac{1+if/f_{\rm C}(t)}{1+if/f_{\rm C,0}}$. This quotient is the ratio of the CC response at the reference time and the response estimated using values of $f_{\rm C}(t)$.

Possibilities for incorporating corrections for variations in the coupled-cavity pole frequency into the production of the strain time series in the low-latency pipeline are being investigated.

3.5 Prospects for improving the method

This section gives prospects for improving the method for tracking temporal variations in the Advanced LIGO detectors. Some of the potential improvements discussed in this section are being actively pursued by the aLIGO calibration group.

As noted in Section 3.3.3, the variations in the CC pole frequency, $f_{\rm C}(t)$, were not implemented in the low-latency calibration pipeline for the O1 and O2 runs. Not compensating for variations in this parameter affects systematic errors at frequencies near the CC pole frequency and above. In its operation the pipeline relies on FIR filters generated from frequency-domain sensing and actuation models. Typically the installation of new FIR filters into the pipeline is a manual process. Variations in $f_{\rm C}(t)$ are a consequence of frequency-dependent changes in the sensing response, thus compensation for this effect in the reconstruction of $h(t)$ requires using a dynamically evolving time-domain filter that represents the CC pole response. The LIGO calibration group is currently investigating the implementation of this feature in the low-latency pipeline.

During the O1 run, a study performed by E. Hall [62] concluded that reduction in the sensing response below ~ 20 Hz at LIGO Hanford, which was not included in the sensing model (e.g. the sensing TF comparisons in Figure 3.13 show discrepancies in the models at these frequencies), can be explained by small detuning of the signal recycling cavity [74]. A simplified model of this effect, incorporated into the sensing model for the O2 run, is parametrized with an optical spring frequency f_s and a Q factor [84]. These parameters estimated from several transfer function measurements were shown to vary over time [63]. Although, temporal variations in this parameters are now monitored with an additional calibration line at ~ 8Hz, incorporating them into the method for tracking temporal variations is an ongoing task.

The overall calibration uncertainties in the strain signal are affected by the uncertainties associated with the initial (reference-time) models and the uncertainties in the time-varying parameters.

Different analytic approaches for determining frequencies and amplitudes of calibration lines to improve their power in resolving the parameter values are being studied.

During the O1 and O2 run temporal variations in the actuation function were parametrized with two time-dependent parameters $\kappa_{\mathrm{PU}}(t)$ and $\kappa_{\mathrm{T}}(t)$. If a non-nominal value in κ_{PU} were observed, the method would not allow pinpointing which of the two actuators, the upper-intermediate or penultimate mass stage, is in disagreement. To independently monitor these actuators a set of calibration lines, each driving a single stage (U, P and T), must be used. Preliminary results from injecting temporary independent calibration lines were used to cross-check the actuation models of the three stages [85, 86]. In order to incorporate these calibration lines into the tracking method, a more extended study is needed.

Chapter 4: THE ADVANCED LIGO PHOTON CALIBRATORS

Calibration of GW detectors is a challenging task, one that requires inducing fiducial displacements of the detector test masses on the order of $10^{-18}\,\mathrm{m}/\sqrt{\mathrm{Hz}}$. In the Advanced LIGO detectors a subsystem called the Photon Calibrator serves this purpose. Photon Calibrators utilize auxiliary lasers to induce fiducial displacements of test masses via photon radiation pressure. Various implementations of such tools have been tested on gravitational wave detectors across the globe [87–89]. In Advanced LIGO the Photon Calibrators (Pcals) play a significant role in the detector calibration process. In part, this became possible due to a set of upgrades that the system underwent for aLIGO [90, 91]. The capacity of aLIGO Pcals to induce test mass displacements at levels of $10^{-18}\,\mathrm{m}/\sqrt{\mathrm{Hz}}$ with an accuracy of $1\,\%$ enable them to be used as primary calibration tools.

The overview of the Advanced LIGO Photon Calibrators given in this chapter covers the design of the aLIGO Pcals and the process of calibrating the Pcal power sensors. A complete review of the Advanced LIGO Photon Calibrators can be found in a recent paper by S. Karki, *et. al.* [91].

Although various Photon Calibrator systems have been implemented or are under construction on different GW detectors, most of the discussions in this chapter apply specifically to the Advanced LIGO Pcals. Therefore, for the convenience of the reader, it is implied that the term Photon Calibrator (Pcal) in the text refers to the aLIGO systems.

4.1 Photon radiation pressure

Force applied perpendicularly to the reflective surface of an end test mass (ETM) pushes it in a longitudinal direction. In the frequency domain the displacement of an ETM sensed by an interferometer from a modulated force can therefore be written as follows:

$$\widetilde{x}(f) = -\left[1 + \frac{M}{I}(\vec{a}\cdot\vec{b})\right] S(f)\widetilde{F}(f), \tag{4.1}$$

where x is the induced displacement, the term $(\vec{a} \cdot \vec{b})\frac{M}{I}$ accounts for the rotational motion of the ETM induced by the applied force, $S(f)$ is the force-to-displacement transfer function, $\widetilde{F}(f)$ is the magnitude of the force vector and $\vec{a}$ is the point on the surface of the ETM at which it is applied. Fourier transforms are indicated with ˜ (tilde). M is the mass of the ETM and I is its moment of inertia. The vector $\vec{b}$ points to the location on the ETM at which the displacement x is measured by the interferometer's laser beam. Since an interferometric GW detector senses displacements of ETMs with a Michelson interferometer, $\vec{b}$ points to the position of the main interferometer beam. $\vec{a}$ and $\vec{b}$ are vectors in the 2-d coordinate system in the plane perpendicular to the measured displacement and with the origin at the center of the ETM (see Figure 4.1).

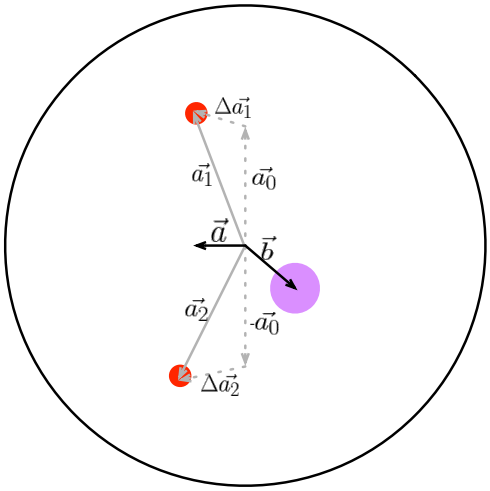

Figure 4.1: Schematic diagram of positions of the main interferometer beam and the Photon Calibrator beams that induce displacements of a test mass via radiation pressure on the surface of a test mass. Vector $\vec{b}$ points to the beam spot of the main interferometer beam, vector $\vec{a}$ points to the center of force of beams that induce displacements via radiation pressure as shown in Equation (4.1). From [91].[10]

Although Equation 4.1 has a generalized form, in that it does not imply a particular nature of the applied force, in the realm of the Pcal system F is produced via radiation pressure from the Pcal beams and $\vec{a}$ corresponds to the center of force of the Pcal beams (see Section 4.3).

The energy of a laser beam is transferred through space by photons, fundamental particles of

[10]Reprinted from S. Karki, D. Tuyenbayev, S. Kandhasamy, et al. *Review of Scientific Instruments*, 87(11):114503, 2016, with the permission of AIP Publishing.

the electric field. When a photon interacts with an object, by being absorbed or reflected from its surface, the momentum or twice the momentum it carries is transferred to the object. This process creates *photon radiation pressure*.

Momentum carried by an individual photon is inversely proportional to the wavelength of the electric field, λ. It is expressed as

$$p = \frac{h}{\lambda}, \tag{4.2}$$

where p is the momentum and h is the Planck constant. Therefore, the energy carried by a photon is

$$E = pc, \tag{4.3}$$

where c is the speed of light. When a photon is absorbed upon reaching a surface of an object the momentum of the photon is fully transferred to the object. On the other hand, when a photon is reflected, the normal component of its momentum vector is inverted, $\vec{p}_r \cdot \hat{n} = -\vec{p}_i \cdot \hat{n}$, where $\hat{n}$ is the normal to the surface and subscripts i and r stand for "incident" and "reflected." Thus, momentum transferred upon reflection is double the normal component of the original momentum of the photon, $|\Delta\vec{p}| = 2|\vec{p}_i \cdot \hat{n}|$.

At the macroscopic level, the force exerted upon a perfectly reflective surface via radiation pressure can be expressed as follows:

$$F = \frac{2\cos\theta}{c} P, \tag{4.4}$$

where P is the beam power in watts and θ is the angle of incidence $[\mathrm{rad}]$. The factor of "2" indicates that twice the photon momentum is transferred upon reflection from the surface of the test mass.

The Pcal system uses power-modulated laser beams to induce longitudinal displacements of an ETM and is capable of driving with various waveforms. Given that displacements induced by Pcals are often analyzed in the frequency domain, it makes sense to write the force-to-displacement relation as a function of frequency. Combining Equations (4.1) and (4.4) we get the so-called *Pcal*

power to displacement equation:

$$\widetilde{x}_{\mathrm{pcal}}(f) = -\frac{2\cos\theta}{c}\left[1 + \frac{M}{I}(\vec{a}\cdot\vec{b})\right] S(f)\widetilde{P}(f). \tag{4.5}$$

Photon radiation pressure is inherently repulsive ($P \geq 0$), thus to allow induction of periodic sinusoidal displacements the power modulation of the Pcal beams is set to run with a constant offset. For example, for a single-frequency modulation, $P(t) = P_{\mathrm{offset}} + A\sin(2\pi f t)$.

4.2 The Photon Calibrator instrumentation

The increased design sensitivity of the Advanced LIGO detectors over the Initial LIGO detectors puts higher constraints on the performance of detector subsystems. For the Pcals to meet the new requirements they also underwent a major upgrade within the Advanced LIGO project. Key aspects that have been taken into account in the design of the Advanced LIGO Pcal system include

- the capacity to induce fiducial displacements of a test mass at the level of 10^{-18}–$10^{-15}\,\mathrm{m}/\sqrt{\mathrm{Hz}}$,
- calibration of the absolute power in the Pcal beams with a specified accuracy of $\sim 1\,\%$,
- minimization of the induced noise in the most sensitive frequency band of the detector,

Each LIGO site hosts two sets of Photon Calibrators, one at each of the end stations. All four Pcal installations have the same specification, and any of the two Pcals installed at an aLIGO detector can be used and is sufficient for calibration of the detector. Therefore, only one of the two Pcals is used for main calibration tasks, while the second system serves as a backup and as a tool for investigations of the calibration accuracy. The system that is being utilized for the detector calibration for a given observation period is referred to as the *primary* Pcal system, and the other one as the *secondary* Pcal system. Since specifications of all Pcals are identical, on an aLIGO detector either of the two Pcals, i.e. an X-end or a Y-end Pcal, can be chosen as the primary system. During normal operation of the detector the primary Pcal is used for continuously tracking the detector calibration and the secondary system is used for other tasks such as injection

of temporary low-SNR calibration lines at high frequencies or simulated GW waveforms.

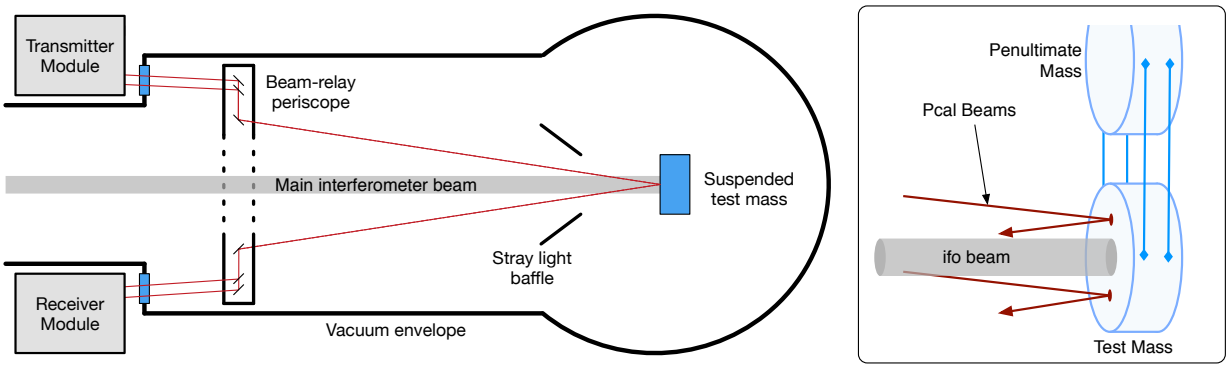

Figure 4.2: Schematic diagram of an Advanced LIGO Photon Calibrator installation. From [91].[10]

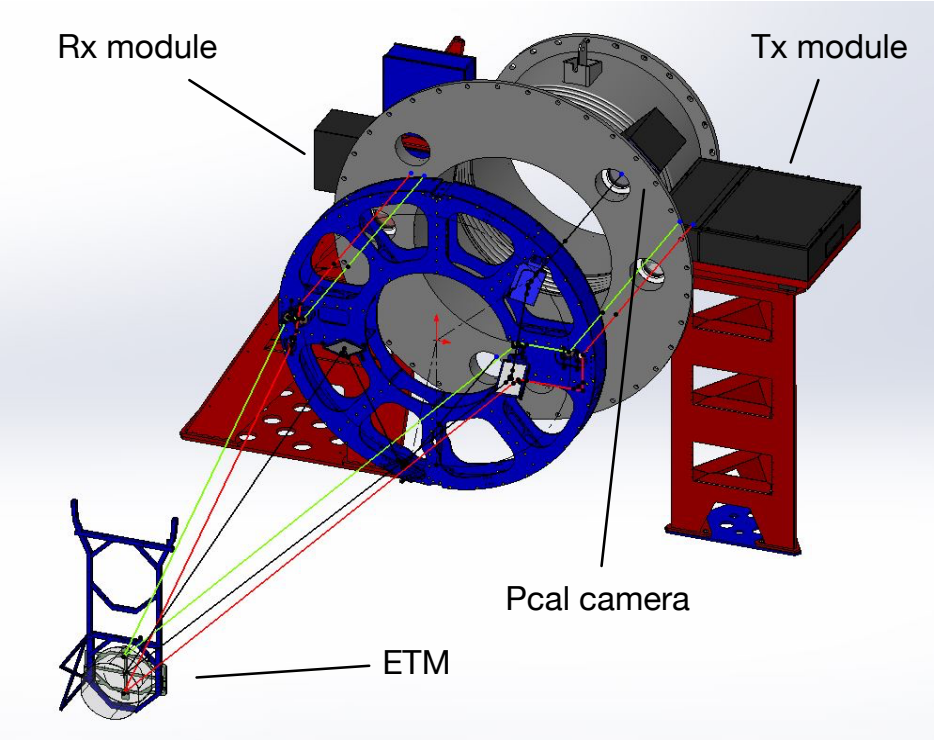

Figure 4.3: The aLIGO Photon Calibrator periscope structure. From [92].

A Pcal system consists of the transmitter (Tx) and receiver (Rx) modules, an in-vacuum periscope structure, electronics modules and a digital camera. A schematic diagram of the Tx and Rx modules and the periscope structure is shown in Figure 4.2. The Tx and Rx modules are mounted on top of stainless steel pylons at opposing sides of the vacuum envelope that encloses the main optics

of the Advanced LIGO interferometer as shown in the detailed drawing of the periscope structure (Figure 4.3). The digital camera is attached directly to a dedicated viewport on the vacuum tube.

Pcal beams are generated in the transmitter module (see Section 4.2.1). After transmitting through a dedicated viewport, they reach an in-vacuum periscope structure, which directs the beams towards the test mass. After the beams are refected from the test mass, with the help of another set of mirrors on the periscope structure, they are directed out of the vacuum chamber through a different viewport. Finally, the beams terminate inside of the Pcal receiver module.

Displacements of an ETM induced by the Pcal depends on the power in the beams directly incident on it; and it is worth noting that the power is monitored by the photodetectors in the `Tx` and `Rx` modules, not right on the ETM. Thus, power losses occurring along the beam paths, e.g. due to transmission through the viewports and reflections from the periscope mirrors, limits the accuracy of determining the actuation power by Pcals.

In the Advanced LIGO the Pcal viewport windows are made of optical quality super-polished glass and the surfaces have been processed with an anti-reflection coating, giving a specified transmissivity of $99.6\,\%$ for infrared frequencies. Utilization of these windows and highly reflective periscope mirrors allowed to significantly reduce the optical losses and reach an overall Pcal optical efficiency of better than $98\,\%$. The remaining $< 2\,\%$ power losses are included in the Pcal uncertainty budget (see Section 4.5).

4.2.1 Transmitter and receiver modules

The optical layout of the Pcal transmitter module (the Tx module) is given in Figure 4.4, (a). The module houses a 2-W Nd:YLF laser source which generates a laser beam with wavelength $1047\,\mathrm{nm}$. The beam is sent to an acousto-optic modulator (AOM) which produces a diffracted beam. The fraction of the diffracted beam power is controlled by the amplitude of the $80\,\mathrm{MHz}$ drive signal; the undiffracted portion of the original beam is terminated with a beam block. The diffracted beam is sent to a wedge beamsplitter that produces two sample beams. One of the sample beams is sent to a photodetector used by the *Optical Follower Servo* (OFS) whose purpose is to

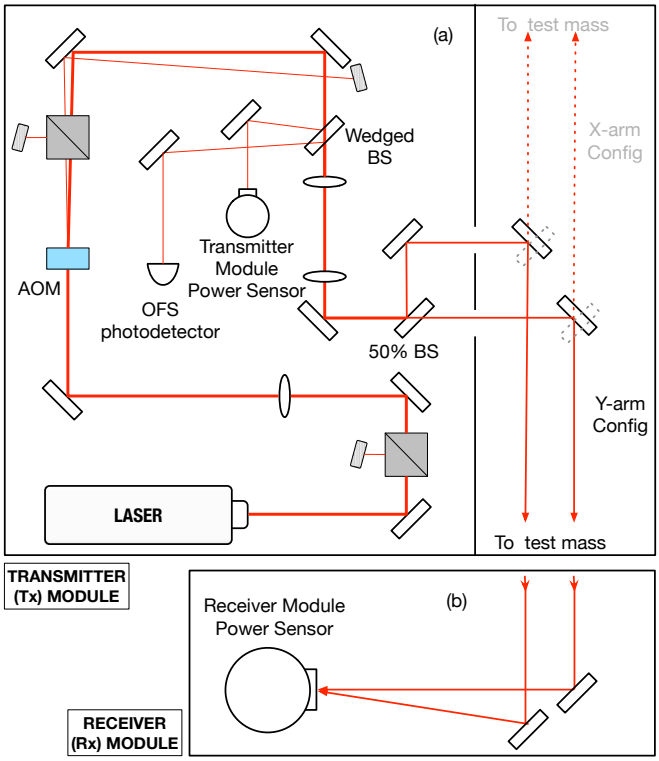

Figure 4.4: Optical layouts of the Photon Calibrator transmitter and receiver modules. Descriptions of the layouts are given in Section 4.2.1. From [91].[10]

ensure an accurate reproduction of the requested waveforms and suppression of unintended noises and harmonic modes by controlling the AOM drive signal. The characteristics of the OFS are outlined in Section 4.2.2. The other sample beam is sent to an integrating sphere-based photodetector, called the TxPD. Two lenses in the path of the beam transmitted through the wedge beamsplitter (see Figure 4.4), are used to focus the beam on the surface of an ETM (i.e. at an effective distance of the test mass along the beam path). Before exiting the Tx module the beam is split into two beams of equal power.

Since the sole function of the receiver module (the Rx module) is monitoring the combined power in the beams reflected from the ETM, contrary to the Tx module, its layout is noticeably simple. The Rx module houses an integrating-sphere-based photodetector assembly, the RxPD. It measures the combined power in the Pcal beams reflected from the surface of the ETM, relayed by the periscope mirrors and transmitted through the vacuum envelope viewport. Each Pcal beam is

relayed to the input port of a $4\,\mathrm{in}$ integrating sphere where they are terminated. The layout of the receiver module is shown in Figure 4.4.

Note that both the TxPD and the OFS PD estimate the Pcal beam power by sampling constant fractions of the beam, whereas the RxPD directly measures the total power in the beams reflected from the ETM.

4.2.2 Optical Follower Servo

In addition to external noises, the sensitivity of an aLIGO detector is limited by background noises from its sensing and control systems. For aLIGO to reach its design sensitivity, systems of the GW detector must satisfy their respective noise requirements. The Pcal being one of the systems that directly induces forces onto the test masses, it was determined that the displacement noise from the Pcal beams must be kept one order of magnitude below the aLIGO design sensitivity. The Optical Follower Servo (OFS) limits the power noise in the Pcal beams by controlling the amount of light from the laser that is diffracted by the acousto-optic modulator. Another function of the OFS control loop is to ensure that modulated excitations used for assessment of the sensing and actuation function responses are accurately reproduced by the Pcal induced displacements.

The schematic diagram of the servo loop is given in Figure 4.5. The OFS monitors the beam power with a dedicated photodetector, the OFS PD. It measures a constant fraction of the beam power extracted with an uncoated wedge beam splitter (see Figure 4.4). The difference between the OFS PD measurements and the requested waveform is sent to the AOM driver which, based on this difference, adjusts the magnitude of the radio-frequency signal to the AOM.

The unity gain frequency of the OFS closed-loop transfer function is $\sim 100\,\mathrm{kHz}$ and the phase margin is 62°. As shown in Figure 4.6, the loop suppression brings the relative power noise of the Pcal laser to below the aLIGO requirements.

The relationship between the beam power diffracted by the AOM and the amplitude of the drive signal is not linear. In fact, the AOM is capable of diffracting up to $\sim 80 - 85\,\%$ of the total beam power, and the nonlinearity of its response to the drive is strongest as the diffracted power

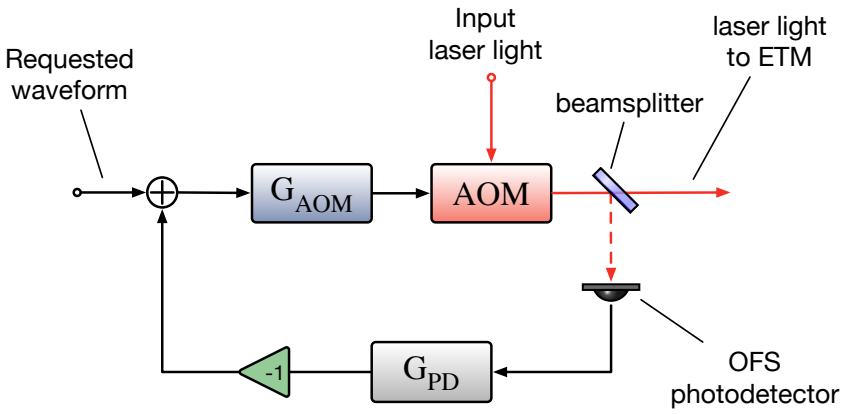

Figure 4.5: A simplified optical layout showing the Pcal Optical Follower Servo (OFS) control loop. Block "AOM" represents the acousto-optic modulator that diffracts a portion of the input laser beam that will be sent to an ETM. The OFS photodetector is the sensor for the OFS feedback signal that measures power in a small fraction of the diffracted beam. The output of the OFS photodetector is multiplied by a gain factor that is indicated with the "G_{PD}" block to produce the feedback signal. The difference of the requested waveform (input signal) and the feedback signal is multiplied by the gain of the AOM driver, G_{AOM}, and then it is sent to the AOM.

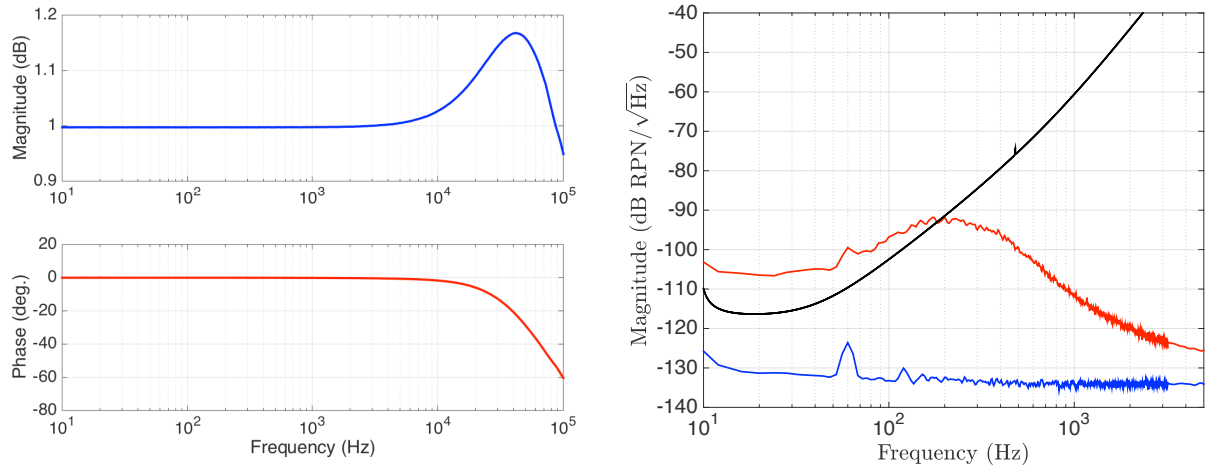

Figure 4.6: *Left:* Measured open- (*blue*) and closed-loop (*red*) transfer function of the Optical Follower Servo. The unity gain frequency of the closed-loop response is about 100 kHz. *Right:* The relative power noise (RPN) of the Pcal laser. The free running, i.e. open-loop, RPN (*red*) exceeds the Advanced LIGO required levels (*black*); the suppressed, i.e. closed-loop, RPN (*blue*) is below the required levels. Taken from [91].[10]

approaches this maximum. As shown in Figure 4.7, the drive signal to the AOM has been adjusted by the OFS loop such that the power modulations mimic requested sinusoidal signal.

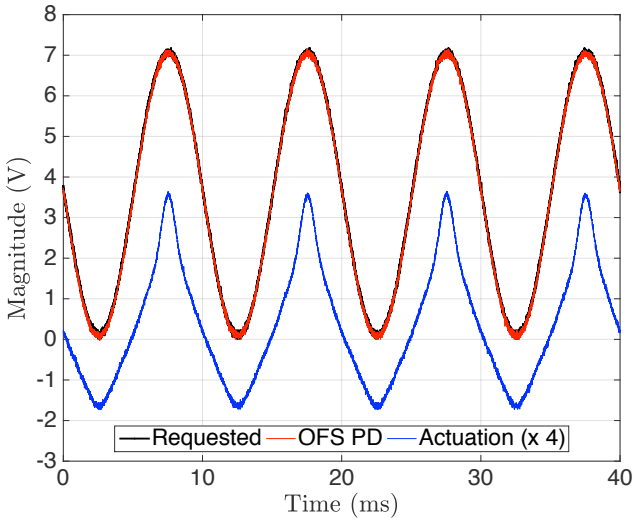

Figure 4.7: Comparison of the requested waveform, the optical follower servo (OFS) photodetector output signal and the AOM drive (actuation) signal. The requested trace (*black* overlapped by the red trace) is closely reproduced by the power modulation from the AOM drive as measured by the OFS photodetector (*red*). The drive (actuation) signal sent to the AOM (*blue*) shows a non-linear response of the AOM. Taken from [91].[10]

4.3 Beam positions on the ETM

In 2007, a study completed by Hild *et. al.* showed that when the main beam of the detector and the Pcal beam both targeted to the center of an ETM local elastic deformations of the test mass surface from Pcal radiation pressure affected displacements measurements made with the main beam [93]. A follow-up study by Goetz *et. al.* showed that the errors due to the local deformations can reach $50\,\%$ [89]. As a consequence, the Advanced LIGO Pcal system was designed to use two beams directed to the points on the ETM symmetrically offset from its center (see Figure 4.2).

The force-to-displacement factor that was discussed in Section 4.1 (Equation 4.1) is affected, among other quantities, by the coordinates of the point on the test mass at which the actuation force is applied. A vector representing these coordinates, the so-called *center of force* (COF) of the Pcal

beams, is calculated as their power weighted mean coordinates,

$$\vec{a} = \frac{\sum_{i=1,2} P_i \vec{a}_i}{\sum_{i=1,2} P_i}, \tag{4.6}$$

where $\vec{a}_1$ and $\vec{a}_2$ are vectors pointing to the spot positions from the two Pcal beams on the ETM surface (Pcal spot positions), P_1 and P_2 are the beam powers. Given that the Advanced LIGO employs a single AOM for controlling power in both Pcal beams, *i.e.* the ratio P_1/P_2 is constant, the above equation can be written in a simplified form as

$$\vec{a} = \frac{\beta \vec{a}_1 + \vec{a}_2}{\beta + 1}, \tag{4.7}$$

where $\beta = P_1/P_2$ is the ratio of the powers.

The Pcal spot positions are determined with the help of the Pcal beam localization system. It consists of a high-resolution (6000×4000 pixels) digital single lens reflex camera (Nikon D7100) with the infrared filter removed from its sensor. The camera is coupled with a telephoto lens. The Pcal cameras are mounted on separate viewports of the vacuum envelope and are operated remotely via the Ethernet interface. A mostly unobstructed view of the ETM from the point of view of the camera is provided by relay mirrors installed on the periscope structure.

Images acquired with the cameras are processed in the MATLAB application. A collection of scripts used for determining Pcal spot positions from the images is called the *Pcal image analysis* library. The procedure for localizing Pcal spot positions requires analyzing two images from Pcal cameras (Figure 4.8). First, an image with a test mass illuminated with background light is used to determine the transformation between the pixel matrix and the coordinate system of the surface of an ETM in metric units. High-contrast details in this image are sufficient to determine the position of the test mass with respect to the frame of the image, at the same time the illumination obscures the Pcal spots. The position of the test mass in the frame of the image is calculated from several points of the electrostatic actuator electrodes on the reaction mass. Then, another

image is given as an input to the code. This time the only light on the image is coming from the Pcal beams which allows pinpointing the pixel coordinates of the Pcal beams. Finally, using the transformation between the image and the coordinates of the test mass surface (obtained from the first image), pixel coordinates of Pcal beams are transformed to their positions on the ETM (in metric units).

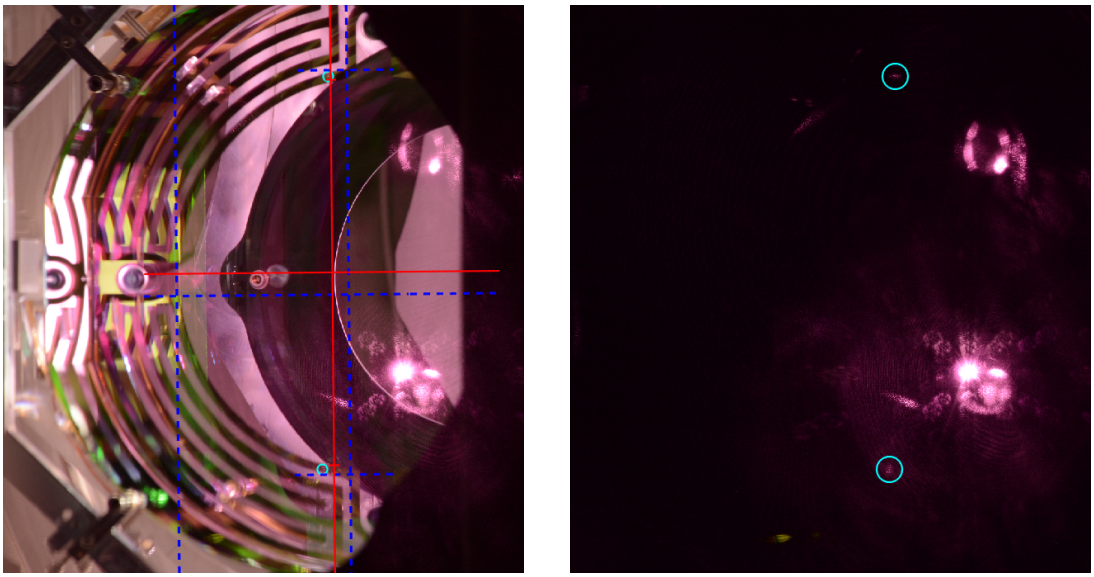

Figure 4.8: Photon Calibrator (Pcal) beam localization images. Two images taken with a Pcal camera are used in the beam localization procedure: an image of an illuminated test mass (*left*) and an image of test mass with illumination turned off (*right*). The pattern of the electrostatic actuator electrodes on the reaction mass, that is visible on the first image, is used for estimating the position of the test mass with respect to the frame of the image. The second image is used for determination of the positions of Pcal beams on the surface on the test mass.

One way the information about the beam positions obtained from the Pcal image analysis procedure can be used is by adjusting the Pcal force calibration factor. This would be a reasonable assumption given that the force-to-displacement equation already includes a term that approximates the effect caused by the beam offsets (see Section 4.1). However, for a number of reasons that will be discussed below, not having such an offset is more preferable. Thus, instead, the Pcal image analysis results are used to make manual in-place adjustments of the beams positions on an ETM and direct them to their nominal positions. The adjustments are made until the remaining Pcal beam offsets from their nominal positions are less than, ideally, $\sim 2\,\mathrm{mm}$. The combined offset

of the Pcal beams is used in the Pcal force uncertainty estimation.

Now, one of the reasons it is not preferred to leave the Pcal spots on the ETM with undesired offsets, is that applying forces to an ETM can in general excite internal vibration modes of the mirror, which will result in frequency-dependent errors of the estimated displacement of the test mass to the applied force.

4.4 Pcal power sensor calibration

The Pcal beams reflected from an ETM exert forces due to photon radiation pressure. Therefore the displacement of the test mass scales proportionally with absolute power in the Pcal beams. Power in the beams is continuously monitored with power sensors in the transmitter and the receiver modules, the TxPD and RxPD sensors (see Section 4.2).

Laser power sensors in Pcal are power-to-voltage transducers, i.e.

$$V_i = P\rho_i, \tag{4.8}$$

where i identifies a particular sensor (TxPD, RxPD, etc.), P is the measured laser power, V_i is the voltage response of a given sensor and ρ_i is the *calibration coefficient* of the given sensor. Values of these coefficients are determined through a set of measurements which comprise the *Pcal power sensor calibration* process. This process involves the use of intermediate power sensors, calibration standards – the *Gold Standard* (GS) that holds the absolute calibration from NIST, and *Working Standards* (WSs) which are used to transfer the GS calibration to the TxPD and RxPD sensors.

4.4.1 Calibration standards

In Advanced LIGO the devices used to transfer the NIST calibration to the Pcal sensors installed at the end stations are called *calibration standards*. Although these devices share the same design[11], we distinguish the one which is annually calibrated at the National Institute of Standards and

[11]Except for the Checking Standard, which is a thermopile-based device used for cross-checks of GS and WS calibrations. Its assembly is described in [94].

Technology (NIST) in Boulder, CO as the Gold Standard, while we refer to the other devices as Working Standards.

The GS and WSs use unbiased InGaAs photodetectors mounted on 4-inch diameter integrating spheres (see Figure 4.9). Each photodetector is coupled with a Keithley 428 PROG current amplifier and a Keithley 2100 digital voltmeter.

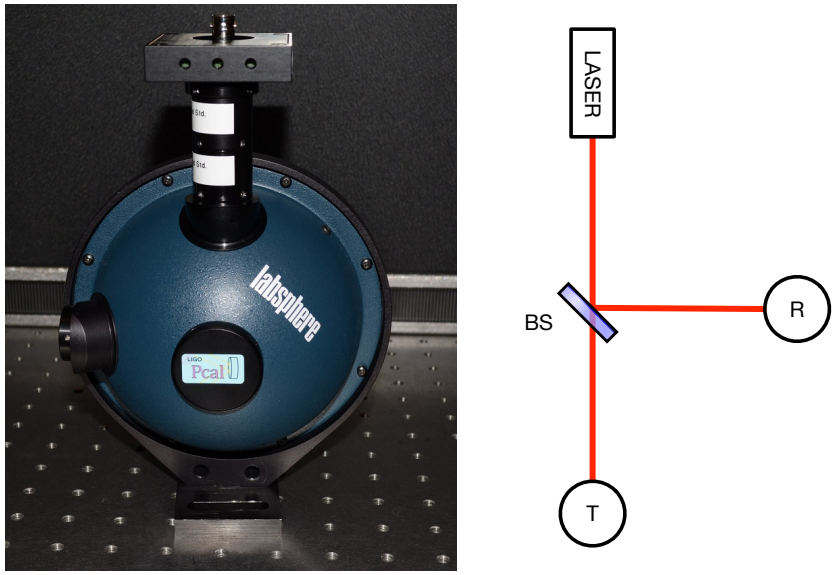

Figure 4.9: *Left:* Calibration standard assembly. aLIGO calibration standards (i.e. GS and WSs) are used for transferring the NIST calibration to the Pcal TxPD and RxPD sensors. They use unbiased InGaAs photodetectors mounted on $4\,\mathrm{in.}$ integrating spheres. *Right:* Experimental setup used for measuring the WS over GS response ratio. The beamsplitter is used to split the output beam from a $0.5\,\mathrm{W}$ laser operating at a wavelength $\lambda = 1047\,\mathrm{nm}$. The calibration standards are placed at points "T" and "R" to measure the transmitted and reflected beam powers. Simultaneous recording of the time series from both devices allows elimination of laser power fluctuations from the response ratios.

The GS calibration is transferred to the WSs with the "procedure for measuring the $\mathrm{WS}n/\mathrm{GS}$ response ratio" [95]. The experimental setup used in the procedure is shown in Figure 4.9. A $0.5\,\mathrm{W}$ laser source operating at $1064\,\mathrm{nm}$ and a beam splitter are used to produce two beams with a constant power ratio. First, a pair of simultaneous time-series is recorded when the GS and a WS are placed in the paths of the transmitted (T) and reflected (R) beams respectively. After this measurement, the calibration standards are swapped, i.e. the device that was in the transmitted beam path "T" is moved to point "R" and vise-versa, and another set of time-series are recorded.

These four time-series measurements are used to determine the *response ratio of the devices*, α_{W}, and the uncertainty associated with it, $\sigma_{\alpha_{\mathrm{W}}}$ [91]. Furthermore, the response ratio together with the absolute calibration factor of the GS provided by NIST, ρ_{G}, can be used to calculate the calibration factor of the WS:

$$V_{\mathrm{W}} = P\alpha_W\rho_{\mathrm{G}} \equiv P\rho_{\mathrm{W}} \tag{4.9}$$

There are currently four calibration standards that are routinely used for calibration and cross-checking of the results: the gold standard, two working standards and a checking standard (CS). The LIGO calibration group refers to the two working standards the "WSH" and "WSL," the first one is used for calibration of the Pcal transmitter and receiver modules at LIGO Hanford and the second is used at LIGO Livingston. Calibrations of both of the WSs are traceable to NIST via the GS device.

4.4.2 Calibration of the TxPD and RxPD sensors

The TxPD and RxPD of each Pcal system at both the LIGO detectors are calibrated with the help of a corresponding WS device. The calibration procedure involves taking six sets of measurements.[12] The WS device, in particular, is used to directly measure power in the two beams exiting the transmitter module and the power in the beams entering the receiver module. This is done by placing the WS in the dedicated section of the transmitter module and then placing it the receiver. Similarly to the $\mathrm{WS}n/\mathrm{GS}$ procedure, in each configuration time series are recorded simultaneously with two devices to avoid biases from variations in the Pcal beam power.

The outcomes of these measurements are the estimated ratios of the TxPD and RxPD sensor responses to the WS response, α_{T} and α_{R}. Thus for input power P the TxPD and RxPD outputs

[12] Additionally, background levels of all three power sensors, TxPD, RxPD and WS, are also measured and subtracted.

(in volts) are

$$V_{\mathrm{T}} = P\alpha_{\mathrm{T}}\rho_{\mathrm{W}} \equiv P\alpha_{\mathrm{T}}\alpha_{\mathrm{W}}\rho_{\mathrm{G}}, \tag{4.10}$$

$$V_{\mathrm{R}} = P\alpha_{\mathrm{R}}\rho_{\mathrm{W}} \equiv P\alpha_{\mathrm{R}}\alpha_{\mathrm{W}}\rho_{\mathrm{G}}. \tag{4.11}$$

It is important to note that, although the TxPD measures a small fraction of the power in the Pcal beam, its calibration factor corresponds to the power in the beams exiting the transmitter module. Therefore, in the case when there are no power losses along the beam path (between the Tx and Rx modules), the calibrated TxPD and RxPD sensor outputs are expected to be the same. However, total losses in the power of Pcal beams are on the order of $1-2\,\%$, for powers measured by the TxPD and RxPD sensors P_{T} and P_{R}. The power contributing to the radiation pressure induced displacements of the test mass lie somewhere between the two measured values.[13] To set the calibration coefficients for the TxPD and RxPD sensors, the mid-point of this interval is chosen to represent power of the Pcal beams reflected from the test mass,

$$\mathcal{P} = \frac{1}{2}(P_{\mathrm{T}} + P_{\mathrm{R}}) \equiv \frac{1+e}{2}P_{\mathrm{T}} \tag{4.12}$$

$$\equiv \frac{1+e}{2e}P_{\mathrm{R}}, \tag{4.13}$$

where $e = P_{\mathrm{R}}/P_{\mathrm{T}}$ is called the *optical efficiency*, and the absolute power uncertainty from Pcal beams is expanded accordingly (see Section 4.5). In terms of power on the ETM, $\mathcal{P}$, the TxPD and RxPD outputs are

$$V_{\mathrm{T}} = \mathcal{P}\rho'_{\mathrm{T}} \equiv \mathcal{P}\frac{2}{1+e}\alpha_{\mathrm{T}}\alpha_{\mathrm{W}}\rho_{\mathrm{G}} \tag{4.14}$$

$$V_{\mathrm{R}} = \mathcal{P}\rho'_{\mathrm{R}} \equiv \mathcal{P}\frac{2e}{1+e}\alpha_{\mathrm{R}}\alpha_{\mathrm{W}}\rho_{\mathrm{G}}, \tag{4.15}$$

where ρ'_{T} and ρ'_{R} are the optical-efficiency-corrected calibration coefficients of the TxPD and RxPD

[13] If the losses happen before the beams reached the test mass, then P_{R} watts generate the force. On the other hand, if the losses happen after the beams are reflected off of the test mass, then P_{T} watts induces the displacements.

sensors. A detailed description of the procedure for measuring calibration factors of the TxPD and RxPD sensors is given in [96].

4.5 Pcal uncertainties

Uncertainties associated with Pcal-induced displacements are comprised of several factors. In the discussions in this section these factors are grouped into two categories. The first group includes all of the factors that contribute to the uncertainties in the absolute power calibration of the Pcal power sensors, TxPD and RxPD. The second group combines uncertainties of the power-to-displacement transfer function, it includes imperfections of beam spot positions on the test mass, imperfect beam balance in the two Pcal beams, uncertainties in the beam incident angle, and the mass of an ETM.

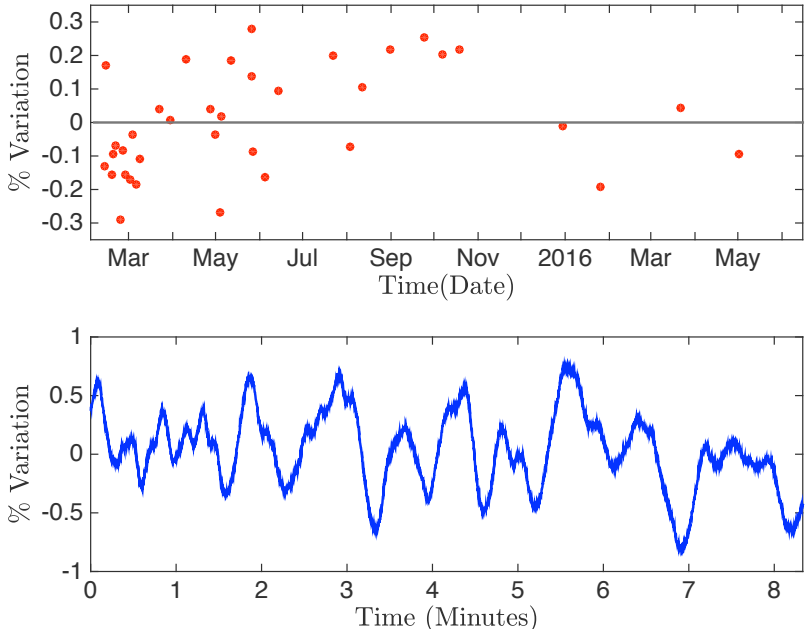

Figure 4.10: Working standard (WS) measurements. The *top panel* shows variations in the measured response ratios of a WS and the Gold Standard over three months. The standard deviation of the measurements is $0.14\,\%$ and the maximum deviation from the mean does not exceed $0.3\,\%$. The *bottom panel* shows variations in the time series recorded from a single calibration standard that arise from laser speckle. Correlation in the consequent output values are caused by slow changes in the spatial speckle patterns on the inner surface of the integrating sphere. From [91].[10]

The 1-σ uncertainty in the absolute power calibration of the GS device, ρ_{G}, provided by NIST, based on the two most recent calibration reports is $0.51\,\%$.

Table 4.1: Uncertainties associated with Photon Calibrator. *Left:* Uncertainty estimate for the RxPD power sensor calibration in terms of power reflected from the end test mass. *Right:* Uncertainty in Pcal-induced test mass displacements. The power calibration and the rotational effect introduce the most significant uncertainty. [91].[10]

Parameter	**Relative Uncertainty**	**Parameter**	**Relative Uncertainty**
NIST $\rightarrow$ GS [ρ_G]	0.51 %	Laser Power [$\mathcal{P}$]	0.57 %
WS/GS [α_W]	0.03 %	Angle [$\cos\theta$]	0.07 %
Rx/WS [α'_R]	0.05 %	Mass of test mass [M]	0.005 %
Optical efficiency [e]	0.37 %	Rotation [$(\vec{a}\cdot\vec{b})M/I$]	0.40 %
Laser Power ($\mathcal{P}$)	**0.57 %**	**Overall**	**0.75 %**

The main source of the uncertainty associated with the response ratios $\alpha_{\rm W}$, $\alpha_{\rm T}$ and $\alpha_{\rm R}$ is variations in the measured power is due to laser speckle (e.g. Figure 4.10 shows variations due to speckle in the $\mathrm{WS}n/\mathrm{GS}$ measurements). To improve the accuracy of a WS calibration, the mean value of a set of response ratio measurements is used and the uncertainty in $\alpha_{\rm W}$ is calculated from the standard error of the mean.

The uncertainty associated with the power losses between the transmitter and receiver modules (i.e. when $e < 1$) is obtained by taking the interval $[e, 1]$ as the rectangular probability window for the power contributed to the radiation pressure. Therefore, following the guidelines for Type B uncertainties in NIST-1297 [97], the fractional uncertainty due to power losses is calculated as $(1-e)(2\sqrt{3})$.

The overall displacement uncertainty reported in Table 4.1 is calculated by combining fractional uncertainties in all of the parameters in quadrature. This quantity is incorporated in the overall calibration uncertainty of the differential arm length measurements of the Advanced LIGO detectors [66].

Chapter 5: IMPLICATIONS AND CONCLUSIONS

The first and second observing runs of Advanced LIGO lead to several detections of gravitational waves (GWs) from binary black hole mergers, the GW150914, GW151226 and GW170104 events [13, 45, 46].[14,15] The GW150914 event measured on September 14, 2015 at 09:50:45 UTC, in addition to being the first direct observation of GWs, also showed that intermediate-stellar-mass black holes ($\geq 25M_{\odot}$) exist in binary systems and merge within the age of the Universe. Before aLIGO made its first direct measurement of GWs X-ray telescopes were the only instruments available for gathering scientific data about stellar-mass black hole binaries (e.g. [98, 99]). Black holes observed in the X-ray band of the electromagnetic spectrum are in the light-stellar-mass range ($\leq 25M_{\odot}$) [100–102] (see illustration on Figure 5.1). The GW170104 event, provided evidence for black hole binaries with misaligned spins, which suggests that the black holes of this binary might have formed not from an initial heavy-star binary system, but independently, after which the two black holes formed a binary. Furthermore, the GW detections helped to improve binary black hole merger rate estimates [11, 12], with the most recent rate estimate based on the three detections to be between 12 and $213\ \mathrm{Gpc}^{-2}\mathrm{yr}^{-1}$. Although, due to it being calculated soon after the most recent detection (also being based on a small sample size), this estimate is likely biased in favor of higher numbers [13]; with more future detections the accuracy of rate estimates will increase.

Gravitational wave signals are contained in the GW strain time-series computed by the low-latency calibration pipeline. Thus, it should not be surprising that calibration of the strain signal plays an important role in both the initial detection as well as in the consequent estimation of source parameters. In an aLIGO detector a passing GW induces power fluctuations at its anti-symmetric port that are measured with a dedicated power sensors, the DC photodetectors. In addition to providing measurements of GWs, they also serve as the sensor for the differential arm length (DARM) control loop that suppresses fluctuations in the DARM length degree of freedom of the interfer-

[14]The GW151226 signal arrived on December 26, 2015 at 03:38:53 UTC, and GW170104 arrived on January 4, 2017 at 10:11:58 UTC.

[15]A fourth GW transient event, LVT151012, detected on October 12, 2015 at 09:54:43 UTC had lower statistical significance [11] and therefore was excluded from discussions in this chapter.

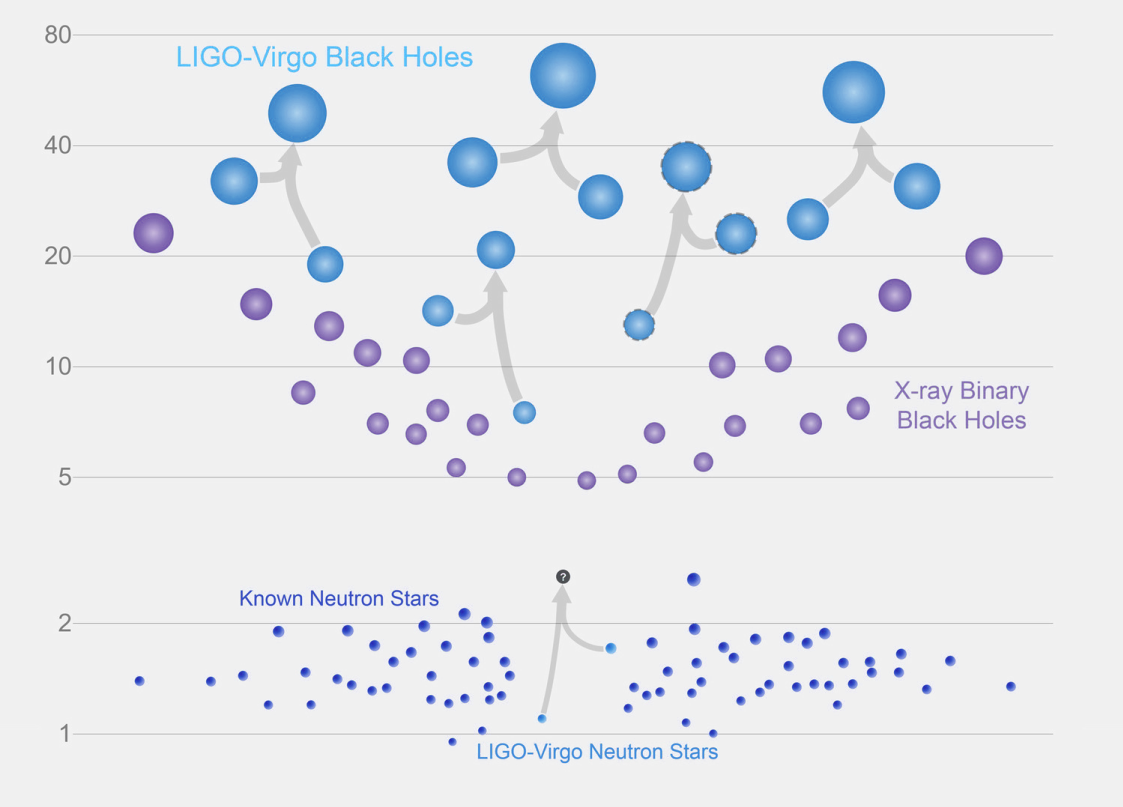

Figure 5.1: Illustration of known black hole and neutron star masses. The graph shows the contrast between the known distribution of stellar-mass black holes from X-ray observations and from the gravitational wave observations. The estimated black hole masses that produced the first detected gravitational waves, the GW150914 signal, are $36.2\,M_{\odot}$ and $29.1\,M_{\odot}$; as a result of the merger they formed a black hole with the mass of $62\,M_{\odot}$. The first event observed both in gravitational waves and in light was produced by the inspiral of a binary neutron star system which was composed of stars with masses $(1.36, 2.26)M_{\odot}$ and $(0.86, 1.36)M_{\odot}$. The mass of the object formed as a result of this merger is estimated to be $2.82^{+0.47}_{-0.09}M_{\odot}$.[16]

ometer. Computed GW strain time series must exclude the effect of the DARM loop suppression which is a function of frequency that slowly evolves over time. Therefore accurate reconstruction of the GW strain time series requires tracking and compensating for temporal variations in the response of the DARM loop.

Improving aLIGO calibration can extend our overall understanding of astrophysics in two distinct ways. First, reducing calibration uncertainties reduces the number of missed detections, thus improving the detection rate. Second, reduced calibration uncertainties improve estimated confi-

[16]Image credit: LIGO-Virgo/Frank Elavsky/Northwestern University

dence intervals on the parameters of the sources that generated the GW events.

In the frequency domain, systematic errors in the response function, $\delta R(f)$, can be expressed in terms of errors in magnitude, $\delta\xi(f)$, and phase, $\delta\phi(f)$, as

$$R(f) = R_t(f)e^{\delta\xi(f)+i\delta\phi(f)}, \tag{5.1}$$

where $R_t(f)$ is the true response of the detector. Hence, the waveform of a GW projected onto the detector, $h_G(f)$, in the reconstructed strain would be distorted by these systematic errors. These distortions can be approximated by

$$\delta h(f) \simeq h_G(f)\big[\delta\xi(f) + i\delta\phi(f)\big]. \tag{5.2}$$

Systematic errors in the magnitude of the response function increase power spectral density estimates of background noise levels by $\exp[2\delta\xi(f)]$ [103]. This discrepancy in the background noise levels and the systematic errors in recorded waveforms can affect the detection rates by increasing probabilities of missed detections. To ensure no significant drop in the detection rate in the search algorithms that rely on numerical relativity waveforms, average frequency-domain calibration errors in magnitude and phase must not exceed $3.5\,\%$ and $0.035\,\mathrm{deg}$ [104].

Source parameters of GW signals are estimated with searches that apply Bayes's theorem. Calibration errors in these searches are modeled with spline polynomials that represent errors in magnitude and phase [105]. Parameters of these polynomials are selected randomly within the calibration uncertainty intervals. Thus narrow uncertainties lead to more confined estimates of the source parameter values [49, 104]. As Lindblom pointed out in [104], to ensure no loss in the scientific information contained in the measured waveforms, the calibration errors must be an order of magnitude lower than the optimal calibration requirements for detection. The frequency-dependent systematic errors in magnitude and phase must thus be below $0.35\,\%$ and $0.0035\,\mathrm{deg}$.

Prior to the aLIGO observation runs, calibration uncertainties were on the order of $10\,\%$ in magnitude and $10\,\mathrm{deg.}$ in phase. In Advanced LIGO however, calibration uncertainties have been

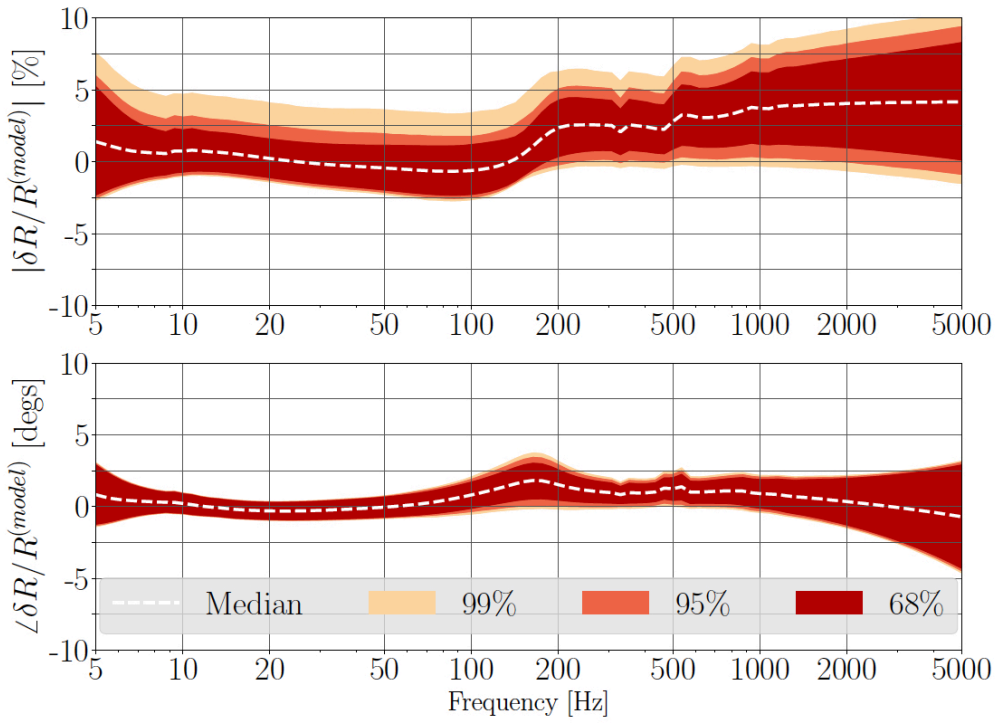

Figure 5.2: Overall LIGO Hanford calibration uncertainties during the O2 run. From [66].[17]

significantly reduced over all of the frequency band between 20 Hz and 2 kHz [64, 66], as shown in Figure 5.2 for the O2 run. These improvements have been enabled by, among other things, employment of the upgraded Photon Calibrator systems together with implementation of the method for tracking and compensating for temporal variations in the response of the DARM loop described in this dissertation.

While the current calibration uncertainties are still far from the levels required to optimize the scientific reach of the LIGO detectors, the rate of improvements during the first two years of the advanced detector era indicates that realizing optimal calibration uncertainty levels is feasible.

[17]Reprinted figure with permission from C. Cahillane, J. Betzwieser, D. A. Brown, et al. *Phys. Rev. D*, 96:102001, 2017. Copyright 2017 by the American Physical Society.

Appendix A: LIST OF PUBLICATIONS

A.1 Publications directly related to the research presented in this thesis

1. D. Tuyenbayev, S. Karki, J. Betzwieser, et al. Improving LIGO calibration accuracy by tracking and compensating for slow temporal variations. *Classical and Quantum Gravity*, 34(1):015002, 2017.

2. S. Karki, D. Tuyenbayev, S. Kandhasamy, et al. The Advanced LIGO photon calibrators. *Review of Scientific Instruments*, 87(11):114503, 2016.

3. B. P. Abbott et al. Calibration of the Advanced LIGO detectors for the discovery of the binary black-hole merger GW150914. *Phys. Rev. D*, 95:062003, Mar 2017.

4. C. Cahillane, J. Betzwieser, D. A. Brown, et al. Calibration uncertainty for Advanced LIGO's first and second observing runs. *Phys. Rev. D*, 96:102001, Nov 2017.

5. A. Viets, M. Wade, A. Urban, et al. Making $h(t)$ for Advanced LIGO. 2017. In preparation, https://dcc.ligo.org/P1700236.

A.2 Other publications

1. B. P. Abbott et al. GW170817: Observation of Gravitational Waves from a Binary Neutron Star Inspiral. *Phys. Rev. Lett.*, 119:161101, Oct 2017.

2. B. P. Abbott et al. Multi-messenger Observations of a Binary Neutron Star Merger. *The Astrophysical Journal Letters*, 848(2):L12, 2017.

3. B. P. Abbott et al. Gravitational Waves and Gamma-Rays from a Binary Neutron Star Merger: GW170817 and GRB 170817A. *The Astrophysical Journal Letters*, 848(2):L13, 2017.

4. B. P. Abbott et al. A gravitational-wave standard siren measurement of the Hubble constant. *Nature*, 551(7678):85–88, 2017.

5. B. P. Abbott et al. GW170814: A Three-Detector Observation of Gravitational Waves from a Binary Black Hole Coalescence. *Phys. Rev. Lett.*, 119:141101, Oct 2017.

6. B. P. Abbott et al. GW170104: Observation of a 50-Solar-Mass Binary Black Hole Coalescence at Redshift 0.2. *Phys. Rev. Lett.*, 118:221101, Jun 2017.

7. B. P. Abbott et al. GW151226: Observation of Gravitational Waves from a 22-Solar-Mass Binary Black Hole Coalescence. *Phys. Rev. Lett.*, 116:241103, Jun 2016.

8. B. P. Abbott et al. Binary Black Hole Mergers in the First Advanced LIGO Observing Run. *Phys. Rev. X*, 6:041015, Oct 2016.

9. B. P. Abbott et al. Observation of Gravitational Waves from a Binary Black Hole Merger. *Phys. Rev. Lett.*, 116:061102, Feb 2016.

10. B. P. Abbott et al. Observing gravitational-wave transient GW150914 with minimal assumptions. *Phys. Rev. D*, 93:122004, Jun 2016.

11. B. P. Abbott et al. GW150914: First results from the search for binary black hole coalescence with Advanced LIGO. *Phys. Rev. D*, 93:122003, Jun 2016.

12. B. P. Abbott et al. Properties of the binary black hole merger gw150914. *Phys. Rev. Lett.*, 116:241102, Jun 2016.

13. B. P. Abbott, (LIGO Scientific Collaboration, and Virgo Collaboration). The Rate of Binary Black Hole Mergers Inferred from Advanced LIGO Observations Surrounding GW150914. *The Astrophysical Journal Letters*, 833(1):L1, 2016.

14. B. P. Abbott et al. Astrophysical Implications of the Binary Black-hole Merger GW150914. *The Astrophysical Journal Letters*, 818(2):L22, 2016.

15. B. P. Abbott et al. Tests of General Relativity with GW150914. *Phys. Rev. Lett.*, 116:221101, May 2016.

16. B. P. Abbott et al. GW150914: Implications for the Stochastic Gravitational-Wave Background from Binary Black Holes. *Phys. Rev. Lett.*, 116:131102, Mar 2016.

17. B. P. Abbott et al. Characterization of transient noise in Advanced LIGO relevant to gravitational wave signal GW150914. *Classical and Quantum Gravity*, 33(13):134001, 2016.

18. S. Adrián-Martínez et al. High-energy neutrino follow-up search of gravitational wave event GW150914 with ANTARES and IceCube. *Phys. Rev. D*, 93:122010, Jun 2016.

19. B. P. Abbott et al. GW150914: The Advanced LIGO Detectors in the Era of First Discoveries. *Phys. Rev. Lett.*, 116:131103, Mar 2016.

20. B. P. Abbott et al. Localization and Broadband Follow-up of the Gravitational-wave Transient GW150914. *The Astrophysical Journal Letters*, 826(1):L13, 2016.

Appendix B: AUTHORIZATIONS FOR THE USE OF PREVIOUSLY PUBLISHED FIGURES

AIP PUBLISHING LLC LICENSE
TERMS AND CONDITIONS

Nov 09, 2017

This Agreement between Darkhan Tuyenbayev ("You") and AIP Publishing LLC ("AIP Publishing LLC") consists of your license details and the terms and conditions provided by AIP Publishing LLC and Copyright Clearance Center.

License Number	4224961057609
License date	Nov 09, 2017
Licensed Content Publisher	AIP Publishing LLC
Licensed Content Publication	Review of Scientific Instruments
Licensed Content Title	The Advanced LIGO photon calibrators
Licensed Content Author	S. Karki, D. Tuyenbayev, S. Kandhasamy, et al
Licensed Content Date	Nov 1, 2016
Licensed Content Volume	87
Licensed Content Issue	11
Type of Use	Thesis/Dissertation
Requestor type	Author (original article)
Format	Print and electronic
Portion	Figure/Table
Number of figures/tables	9
Title of your thesis / dissertation	Extending the scientific reach of Advanced LIGO by compensating for temporal variations in the calibration of the detectors
Expected completion date	Dec 2017
Estimated size (number of pages)	90
Requestor Location	
Billing Type	Invoice
Billing Address	
Total	

IOP Publishing LICENSE
TERMS AND CONDITIONS

Nov 10, 2017

This is a License Agreement between Darkhan Tuyenbayev ("You") and IOP Publishing ("IOP Publishing") provided by Copyright Clearance Center ("CCC"). The license consists of your order details, the terms and conditions provided by IOP Publishing, and the payment terms and conditions.

All payments must be made in full to CCC. For payment instructions, please see information listed at the bottom of this form.

License Number	4225680684257
License date	Nov 10, 2017
Licensed content publisher	IOP Publishing
Licensed content title	Classical and Quantum Gravity
Licensed content date	Jan 1, 1984
Type of Use	Thesis/Dissertation
Requestor type	Author of requested content
Format	Print, Electronic
Portion	chart/graph/table/figure
Number of charts/graphs /tables/figures	6
The requesting person/organization is:	Darkhan Tuyenbayev, for submission to UT San Antonio via ProQuest.
Title or numeric reference of the portion(s)	Figures 1, 2, 3, 4 and 8; Table 1 (extended with an additional column).
Title of the article or chapter the portion is from	Improving LIGO calibration accuracy by tracking and compensating for slow temporal variations
Editor of portion(s)	N/A
Author of portion(s)	D Tuyenbayev, S Karki, J Betzwieser, C Cahillane, E Goetz, K Izumi, S Kandhasamy, J S Kissel, G Mendell, M Wade, A J Weinstein and R L Savage
Volume of serial or monograph.	34
Issue, if republishing an article from a serial	1
Page range of the portion	015002
Publication date of portion	December 6, 2016

Rights for	Main product
Duration of use	Life of current edition
Creation of copies for the disabled	no
With minor editing privileges	yes
For distribution to	Worldwide
In the following language(s)	Original language of publication
With incidental promotional use	no
The lifetime unit quantity of new product	Up to 499
Title	Extending the scientific reach of Advanced LIGO by compensating for temporal variations in the calibration of the detectors
Instructor name	n/a
Institution name	The University of Texas at San Antonio
Expected presentation date	Dec 2017
Billing Type	Invoice
Billing Address	
Total (may include CCC user fee)	

BIBLIOGRAPHY

[1] I. Newton. Philosophiæ naturalis principia mathematica (Mathematical principles of natural philosophy). London, 1687.

[2] C. W. Misner, K. S. Thorne, and J. A. Wheeler. Gravitation. Macmillan, 1973.

[3] B. Schutz. A first course in general relativity. Cambridge university press, 2009.

[4] Tjonnie G. F. Li. Extracting Physics from Gravitational Waves: Testing the Strong-field Dynamics of General Relativity and Inferring the Large-scale Structure of the Universe (doctoral dissertation). 2010. https://gwic.ligo.org/thesisprize/2013/tgfli_thesis.pdf.

[5] B. S. Sathyaprakash and B. F. Schutz. Physics, Astrophysics and Cosmology with Gravitational Waves. *Living Reviews in Relativity*, 12(1):2, Mar 2009.

[6] K. S. Thorne, S. Hawking, and W. Israel. Three hundred years of gravitation, 1987.

[7] A. Einstein. Näherungsweise integration der feldgleichungen der gravitation (Approximate integration of the field equations of gravitation). *Sitzungsberichte der Königlich Preußischen Akademie der Wissenschaften (Berlin)*, 1:688–696, 1916.

[8] A. Einstein. Über Gravitationswellen (On Gravitational Waves). *Sitzungsberichte der Königlich Preußischen Akademie der Wissenschaften (Berlin)*, 1:154–167, 1918.

[9] L. Blanchet. Gravitational radiation from post-newtonian sources and inspiralling compact binaries. *Living Reviews in Relativity*, 17(1):2, Feb 2014.

[10] E. E. Salpeter. The Luminosity Function and Stellar Evolution. *Astrophysical Journal*, 121:161, January 1955.

[11] B. P. Abbott et al. Binary Black Hole Mergers in the First Advanced LIGO Observing Run. *Phys. Rev. X*, 6:041015, Oct 2016.

[12] B. P. Abbott, (LIGO Scientific Collaboration, and Virgo Collaboration). The Rate of Binary Black Hole Mergers Inferred from Advanced LIGO Observations Surrounding GW150914. *The Astrophysical Journal Letters*, 833(1):L1, 2016.

[13] B. P. Abbott et al. GW170104: Observation of a 50-Solar-Mass Binary Black Hole Coalescence at Redshift 0.2. *Phys. Rev. Lett.*, 118:221101, Jun 2017.

[14] P. A. Seoane et al. The Gravitational Universe. 2013.

[15] J. Weber. Detection and generation of gravitational waves. *Phys. Rev.*, 117:306–313, Jan 1960.

[16] L. L. Smarr. Sources of Gravitational Radiation: Proceedings of the Battelle Seattle Workshop. CUP Archive, 1979.

[17] M. E. Gertsenshtein and V. I. Pustovoit. On the Detection of Low Frequency Gravitational Waves. *Sov. Phys. JETP*, 16:433, 1962.

[18] R. L. Forward. Multidirectional, multipolarization antennas for scalar and tensor gravitational radiation. *General Relativity and Gravitation*, 2(2):149–159, 1971.

[19] R. L. Forward. Wideband laser-interferometer graviational-radiation experiment. *Phys. Rev. D*, 17:379–390, Jan 1978.

[20] R. Weiss. Quarterly progress report. *MIT Research Lab of Electronics*, 105:54, 1972.

[21] R. W. P. Drever et al. Gravitational wave detectors. *Proceedings of the Royal Society of London. Series A, Mathematical and Physical Sciences*, 368(1732):11–13, 1979.

[22] H. Billing et al. An argon laser interferometer for the detection of gravitational radiation. *Journal of Physics E: Scientific Instruments*, 12(11):1043, 1979.

[23] D. Shoemaker et al. Noise behavior of the garching 30-meter prototype gravitational-wave detector. *Phys. Rev. D*, 38:423–432, Jul 1988.

[24] A. Abramovici et al. LIGO: The Laser Interferometer Gravitational-Wave Observatory. *Science*, 256(5055):325–333, 1992.

[25] A Giazotto et al. The VIRGO experiment: status of the art. In *First Edoardo Amaldi Conference on Gravitational Wave Experiments*, volume 1, page 86. World Scientific, Singapore, 1995.

[26] K. Danzmann et al. GEO 600 - a 600 m laser interferometric gravitational wave antenna. In E. Coccia, G. Pizzella, and F. Ronga, editors, *First Edoardo Amaldi Conference on Gravitational Wave Experiments*, 1995.

[27] K. Tsubono et al. 300-m laser interferometer gravitational wave detector (TAMA300) in Japan. In E. Coccia, G. Pizzella, and F. Ronga, editors, *First Edoardo Amaldi Conference on Gravitational Wave Experiments*, 1995.

[28] R. Adhikari, P. Fritschel, and S. Waldman. Enhanced LIGO. *LIGO Document Control Center*, 2006. https://dcc.ligo.org/LIGO-T060156/public.

[29] B. P. Abbott et al. LIGO: the Laser Interferometer Gravitational-Wave Observatory. *Reports on Progress in Physics*, 72(7):076901, 2009.

[30] J. Aasi et al. Characterization of the LIGO detectors during their sixth science run. *Classical and Quantum Gravity*, 32(11):115012, 2015.

[31] The VIRGO collaboration. VIRGO Website, 2017. [Online; accessed 28-August-2017] http://www.virgo-gw.eu/.

[32] The VIRGO collaboration. VIRGO joins LIGO for the O2 data-taking period, 2017. [Online; accessed 01-August-2017] http://www.virgo-gw.eu/docs/AdV_joins_O2_en.pdf.

[33] K. Kuroda and the LCGT Collaboration. Status of LCGT. *Classical and Quantum Gravity*, 27(8):084004, 2010.

[34] The KAGRA collaboration. KAGRA Website, 2017. [Online; accessed 28-August-2017] http://gwcenter.icrr.u-tokyo.ac.jp/en/.

[35] B. Willke et al. The GEO-HF project. *Classical and Quantum Gravity*, 23(8):S207, 2006.

[36] K. L. Dooley et al. GEO 600 and the GEO-HF upgrade program: successes and challenges. *Classical and Quantum Gravity*, 33(7):075009, 2016.

[37] European Space Agency. Gravitational wave mission selected, planet-hunting mission moves forward, 2017. [Online; accessed 20-June-2017] http://sci.esa.int/jump.cfm?oid=59243.

[38] M. Armano et al. Sub-Femto-g Free Fall for Space-Based Gravitational Wave Observatories: LISA Pathfinder Results. *Phys. Rev. Lett.*, 116:231101, Jun 2016.

[39] European Projects Service. Einstein Telescope Website, 2017. [Online; accessed 20-June-2017] http://www.et-gw.eu/.

[40] S. Hild, S. Chelkowski, and A. Freise. Pushing towards the ET sensitivity using 'conventional' technology. 2008.

[41] S. Hild et al. A xylophone configuration for a third-generation gravitational wave detector. *Classical and Quantum Gravity*, 27(1):015003, 2010.

[42] S. Hild et al. Sensitivity studies for third-generation gravitational wave observatories. *Classical and Quantum Gravity*, 28(9):094013, 2011.

[43] R. A. Hulse and J. H. Taylor. Discovery of a pulsar in a binary system. *Astrophysical Journal, Letters*, 195:L51–L53, January 1975.

[44] J. H. Taylor and J. M. Weisberg. A new test of general relativity - Gravitational radiation and the binary pulsar PSR 1913+16. *Astrophysical Journal*, 253:908–920, February 1982.

[45] B. P. Abbott et al. Observation of Gravitational Waves from a Binary Black Hole Merger. *Phys. Rev. Lett.*, 116:061102, Feb 2016.

[46] B. P. Abbott et al. GW151226: Observation of Gravitational Waves from a 22-Solar-Mass Binary Black Hole Coalescence. *Phys. Rev. Lett.*, 116:241103, Jun 2016.

[47] B. P. Abbott et al. Observing gravitational-wave transient GW150914 with minimal assumptions. *Phys. Rev. D*, 93:122004, Jun 2016.

[48] S. Klimenko et al. Method for detection and reconstruction of gravitational wave transients with networks of advanced detectors. *Phys. Rev. D*, 93:042004, Feb 2016.

[49] B. P. Abbott et al. Properties of the binary black hole merger gw150914. *Phys. Rev. Lett.*, 116:241102, Jun 2016.

[50] B. P. Abbott et al. GW170817: Observation of Gravitational Waves from a Binary Neutron Star Inspiral. *Phys. Rev. Lett.*, 119:161101, Oct 2017.

[51] B. P. Abbott et al. GW170814: A Three-Detector Observation of Gravitational Waves from a Binary Black Hole Coalescence. *Phys. Rev. Lett.*, 119:141101, Oct 2017.

[52] B. P. Abbott et al. Multi-messenger Observations of a Binary Neutron Star Merger. *The Astrophysical Journal Letters*, 848(2):L12, 2017.

[53] B. P. Abbott et al. Gravitational Waves and Gamma-Rays from a Binary Neutron Star Merger: GW170817 and GRB 170817A. *The Astrophysical Journal Letters*, 848(2):L13, 2017.

[54] B. P. Abbott et al. A gravitational-wave standard siren measurement of the Hubble constant. *Nature*, 551(7678):85–88, 2017.

[55] J. Aasi et al. Advanced LIGO. 32:074001, 2015.

[56] B. P. Abbott et al. Gw150914: The advanced ligo detectors in the era of first discoveries. *Phys. Rev. Lett.*, 116:131103, Mar 2016.

[57] F. Matichard et al. Seismic isolation of Advanced LIGO: Review of strategy, instrumentation and performance. *Classical and Quantum Gravity*, 32(18):185003, 2015.

[58] N. A. Robertson et al. Quadruple suspension design for Advanced LIGO. *Classical and Quantum Gravity*, 19(15):4043, 2002.

[59] D. V. Martynov et al. Sensitivity of the Advanced LIGO detectors at the beginning of gravitational wave astronomy. *Phys. Rev. D*, 93:112004, Jun 2016.

[60] S. Karki, R. Savage, J. Kissel, and E. Goetz. aLIGO DARM Signal Chain. *LIGO Document Control Center*, 2015. https://dcc.ligo.org/LIGO-G1501518.

[61] K. Izumi and D. Sigg. Advanced LIGO: length sensing and control in a dual recycled interferometric gravitational wave antenna. *Classical and Quantum Gravity*, 34(1):015001, 2017.

[62] E. Hall, K. Izumi, and J. Kissel. 0.5 of SRC detuning can explain O1 anomaly in DARM plant. *aLIGO LHO Logbook*, page 27675, 2016.

[63] J. Kissel and D. Tuyenbayev. Process Sensing Functions from Calibration Sweeps To-Date: Optical Gain & Cavity Pole Frequency Consistent; Detuning Spring Frequency *is* Mobile. *aLIGO LHO Logbook*, page 31665, 2016.

[64] B. P. Abbott et al. Calibration of the Advanced LIGO detectors for the discovery of the binary black-hole merger GW150914. *Phys. Rev. D*, 95:062003, Mar 2017.

[65] S. M. Aston et al. Update on quadruple suspension design for Advanced LIGO. *Classical and Quantum Gravity*, 29(23):235004, 2012.

[66] C. Cahillane, J. Betzwieser, D. A. Brown, et al. Calibration uncertainty for Advanced LIGO's first and second observing runs. *Phys. Rev. D*, 96:102001, Nov 2017.

[67] E. Goetz, D. Tuyenbayev, and C. Cahillane. Validating the MCMC parameter estimate, sensing function. *LIGO Document Control Center*, 2016. https://dcc.ligo.org/G1602392.

[68] D. Tuyenbayev, K. Izumi, and J. Kissel. Re: Fourth Round of ER10 Calibration Measurements Complete – Second at 30 W . *aLIGO LHO Logbook*, page 31677, 2016.

[69] D. Tuyenbayev, S. Karki, J. Betzwieser, et al. Improving LIGO calibration accuracy by tracking and compensating for slow temporal variations. *Classical and Quantum Gravity*, 34(1):015002, 2017.

[70] J. Abadie et al. Calibration of the LIGO gravitational wave detectors in the fifth science run. *Nuclear Instruments and Methods in Physics Research Section A: Accelerators, Spectrometers, Detectors and Associated Equipment*, 624(1):223 – 240, 2010.

[71] S. M. Aston et al. Update on quadruple suspension design for advanced ligo. *Classical and Quantum Gravity*, 29(23):235004, 2012.

[72] L. Carbone et al. Sensors and actuators for the Advanced LIGO mirror suspensions. *Classical Quant. Grav.*, 29(11):115005, 2012.

[73] M. Hewitson et al. Charge measurement and mitigation for the main test masses of the geo 600 gravitational wave observatory. *Classical Quant. Grav.*, 24(24):6379, 2007.

[74] B. S. Sheard et al. Observation and characterization of an optical spring. *Phys. Rev. A*, 69:051801, May 2004.

[75] J. Betzwieser and S. Kandhasamy. Calibration: parametrizing sensing function for O1. *aLIGO LLO Logbook*, page 20353, 2015.

[76] J. Kissel. H1 CAL CS Model Restarted to install new TDEP Infrastructure; Frame Builder Restarted . *aLIGO LHO Logbook*, page 20361, 2016.

[77] J. Betzwieser and S. Kandhasamy. Updates to CALCS to be propagated to LHO . *aLIGO LLO Logbook*, page 26126, 2016.

[78] D. Tuyenbayev et al. Tracking temporal variations in the DARM calibration parameters. 2015. https://dcc.ligo.org/LIGO-T1500377/public.

[79] S. Karki. PCAL Signal Chain Topology. *LIGO Document Control Center*, 2015. https://dcc.ligo.org/LIGO-G1501014.

[80] M. Wade. Gravitational-wave Science with the Laser Interferometer Gravitational-wave Observatory (doctoral dissertation). 2015. https://dcc.ligo.org/P1500068.

[81] D. Tuyenbayev. ER7 sensing function trend using Pcal lines . *aLIGO LHO Logbook*, page 19445, 2015.

[82] D. Tuyenbayev. Actuation and sensing functions' correction factors and CC pole frequency trend over the last weekend locks . *aLIGO LHO Logbook*, page 20073, 2015.

[83] J. Kissel, K. Izumi, and D. Tuyenbayev. H1 DARM OLGTFs and PCAL to CAL-CS TFs confirm that H1 ETMY Bias Sign Flip Caused Minimal Change . *aLIGO LHO Logbook*, page 22561, 2015.

[84] K. Izumi and C. Cahillane. Simplifying DARM response with a small SRC detuning. *LIGO Document Control Center*, 2016. https://dcc.ligo.org/LIGO-T1600278.

[85] J. Kissel. Re 2: ETMY UIM and PUM CAL Lines Turn OFF . *aLIGO LHO Logbook*, page 31369, 2016.

[86] D. Tuyenbayev. Re: ETMY UIM and PUM CAL Lines Turn OFF . *aLIGO LHO Logbook*, page 31344, 2016.

[87] T. Accadia and VIRGO Collabration. "Reconstruction of the gravitational wave signal h(t) during the VIRGO sc ience runs and independent validation with a photon calibrator". *Class. Quantum Grav.*, 31:165013, 2014.

[88] L. Rolland et al. "Conceptual design of Advanced VIRGO photon calibration". *VIR*, 0031A-15, 2015.

[89] E. Goetz et al. Precise calibration of LIGO test mass actuators using photon radiation pressure. *Class. Quantum Grav.*, 26:245011, 2009.

[90] H. P. Daveloza et al. Controlling calibration errors in gravitational-wave detectors by precise location of calibration forces. *Journal of Physics: Conference Series*, 363:012007, 2012.

[91] S. Karki, D. Tuyenbayev, S. Kandhasamy, et al. The Advanced LIGO photon calibrators. *Review of Scientific Instruments*, 87(11):114503, 2016.

[92] J. Berliner, P. Daveloza, R. Savage, and J. Gleason. Photon Calibrator Final Design. *LIGO Document Control Center*, 2014. https://dcc.ligo.org/LIGO-T1100068.

[93] S. Hild et al. Photon Pressure Induced Test Mass Deformation in GravitationalWave Detectors. *Class. Quantum Grav.*, 24:56815688, 2007.

[94] E. Goetz, R. Savage, S. Karki, and D. Tuyenbayev. Power Calibration Standard System Descriptions (Photon Calibrator Power Calibration). *LIGO Document Control Center*, 2015. https://dcc.ligo.org/T070210.

[95] D. Tuyenbayev and R. Savage. Photon Calibrator Procedure for Measuring Response Ratios of Power Calibration Standards. *LIGO Document Control Center*, 2015. https://dcc.ligo.org/T1400442.

[96] D. Tuyenbayev, S. Karki, S. Kandhasamy, T. Abbott, and R. Savage. Methodology for Calculating Pcal Calibration Factors. 2015. https://dcc.ligo.org/LIGO-T1500219.

[97] B. N. Taylor and C. E. Kuyatt. Guidelines for Evaluating and Expressing the Uncertainty of NIST Measurement Results. *NIST Technical Document*, 1297, 1994.

[98] B. L. Webster and P. Murdin. Cygnus X-1a Spectroscopic Binary with a Heavy Companion? *Nature*, 235(5332):37–38, 1972.

[99] C. T. Bolton. Identification of Cygnus X-1 with HDE 226868. *Nature*, 235(5336):271–273, 1972.

[100] F. Özel, D. Psaltis, R. Narayan, and J. E. McClintock. The Black Hole Mass Distribution in the Galaxy. *The Astrophysical Journal*, 725(2):1918, 2010.

[101] W. M. Farr, N. Sravan, A. Cantrell, et al. The Mass Distribution of Stellar-mass Black Holes. *The Astrophysical Journal*, 741(2):103, 2011.

[102] L. Kreidberg, C. D. Bailyn, W. M. Farr, and V. Kalogera. Mass Measurements of Black Holes in X-Ray Transients: Is There a Mass Gap? *The Astrophysical Journal*, 757(1):36, 2012.

[103] B. Allen. LIGO calibration accuracy. *LIGO Document Control Center*, 1996. https://dcc.ligo.org/T960189/public.

[104] L. Lindblom. Optimal calibration accuracy for gravitational-wave detectors. *Phys. Rev. D*, 80:042005, Aug 2009.

[105] W. M. Farr, B. Farr, and T. Littenberg. Modelling Calibration Errors In CBC Waveforms. *LIGO Document Control Center*, 2014. https://dcc.ligo.org/LIGO-T1400682/public.

[106] A. Simonnet. Black Holes of Known Mass Illustration. *LIGO Document Control Center*, 2017. https://dcc.ligo.org/LIGO-G1700675.

[107] J. Aasi et al. Advanced LIGO. *Classical and Quant. Grav.*, 32(7):074001, 2015.

[108] K Danzmann. A 600-m laser interferometric gravitational wave antenna. In *Proc. 1st Edoardo Amaldi Conf. on Gravitational Wave Experiments*, pages 100–11. World Scientific, 1995.

[109] E. Goetz et al. Accurate calibration of test mass displacement in the LIGO interferometers. *Classical and Quantum Gravity*, 27(8):084024, 2010.

[110] L. Canete. Optical Follower Servo design for the calibration of a gravitational wave detector. *LIGO Document Control Center*, 2013. https://dcc.ligo.org/LIGO-T1300442.

[111] J. Kissel, D. Tuyenbayev, K. Izumi, E. Goetz, and C. Cahillane. CAL-CS Front-End (and therefore GDS Low-Latency) DARM/DELTAL_EXTERNAL Time-Independent Calibration Updated for O2. *aLIGO LHO Logbook*, page 31693, 2016.

[112] R. Ward. Length Sensing and Control of an Advanced Prototype Interferometric Gravitational Wave Detector (doctoral dissertation). 2010. https://dcc.ligo.org/LIGO-P1000018.

[113] A. Sottile. Charaterization of the photon calibrator data from ligo's 6th science run. https://dcc.ligo.org/LIGO-P1100013, 2011.

[114] D. Tuyenbayev, S. Karki, S. Kandhasamy, T. Abbott, and R. Savage. A Short Overview of Pcal Calibration Steps. 2015. https://dcc.ligo.org/LIGO-T1500283/public.

[115] J. Mizuno, K. A. Strain, P. G. Nelson, et al. Resonant sideband extraction: a new configuration for interferometric gravitational wave detectors. *Physics Letters A*, 175(5):273 – 276, 1993.

VITA

Darkhan Tuyenbayev was born in v. Samarskoe, East-Kaz. oblast, Kazakhstan. In 2006 he received a B.S. degree in Automation and Control Systems from the Kazakh National Technical University in Almaty, Kazakhstan. Between 2005 and 2007 he participated in ACM (Association for Computing Machinery) International Collegiate Programming Contests in Kazakhstan, Uzbekistan, Russia and Japan. He also participated in programming training camps organized by Moscow State University in 2006 and by Petrozavodsk State University in 2007.

He enrolled in graduate school in Physics at the University of Texas at Brownsville in 2011 and received a M.S. degree in 2013. He entered the cooperative Ph.D. in Physics program between the University of Texas at San Antonio and the University of Texas Rio Grande Valley in 2013. In 2014 he joined the LIGO Scientific Collaboration and started research on the calibration of the LIGO detectors, performing most of his research while resident at the LIGO Hanford Observatory in Richland, Washington.

Following the first direct detection of gravitational waves in 2015, together with other members of the collaboration, he was recognized by the 2016 Gruber Prize in Cosmology and by the Special Breakthrough Prize in Fundamental Physics in 2016.

He is planning to continue working within the international gravitational wave detector community.